Impact of PECVD a-Si:H contacting layer deposition on poly-Si/SiO_x/c-Si passivating contacts

Wanyu Si

Delft University of Technology

TU Delft

Impact of PECVD a-Si:H contacting layer deposition on poly-Si/SiO_x/c-Si passivating contacts

by

Wanyu Si

to obtain the degree of Master of Science Sustainable Energy Technology
at the Delft University of Technology,
to be defended publicly on Thursday August 31, 2023.

Student number:	5300789	
Project Duration:	September 1, 2022 - August 31, 2023	
Supervisor:	Prof. dr. Olindo Isabella,	TU Delft | ESE-PVMD | Full Professor
Daily supervisor:	Dr. Zhirong Yao,	TU Delft | ESE-PVMD | PostDoc researcher
Thesis committee:	Prof. dr. Miro Zeman,	TU Delft | ESE-PVMD | Full Professor
	Prof. dr. Ivan Gordon,	TU Delft | ESE-PVMD | Part-time Professor
	Dr. Tom Savenije,	TU Delft | ChemE-OM | Associate Professor
	Dr. Zhirong Yao,	TU Delft | ESE-PVMD | PostDoc researcher

TU Delft

Acknowledgements

As approaching the end of the thesis project, I would like to express my gratitude to all those who supported me and accompanied me during these years. First of all, my greatest thanks will go out to my supervisor Prof. dr. Olindo Isabella, who provided me with a great opportunity to get close to photovoltaics and learn more about solar cell related techniques. With the rich experience and wisdom, he can always rescue me from my confusion in the biweekly group meeting, and constantly inspire me to explore knowledge in unknown areas.

In addition, I would like to thank my daily supervisor Dr. Zhirong Yao. Thank him for the constant guidance, encouragement and patience throughout the project. He always showed the greatest tolerance and kindness, allowing me to develop freely on the points of my own interest.

Also many thanks to the Dr. Paul Procel Moya, Engin Özkol, Yingwen Zhao, Wenxian Wang for actively helping me analyze and solve problems in group meetings. Especially appreciate the help and support from Yingwen, who worked with me together to solve the intensive experimental problems in April.

Next, I would thank all the people who helped me in the lab, including Martijn Tijssen, Stefaan Heirman, Tim Velzeboer, Liqi Cao, Narasimha Raju Pusapati, and Katarina Kovačević at EKL, Roald at Kavli, Prasad Gonugunta and Prasaanth Ravi Anusuyadevi at MSE. They helped me fix the problem from machines or performed a great number of nice measurements.

I also want to thank a lot of friends in Delft, Chengli, Zelin, Yi, Jin, Haoxu, Yan, Qi, Marnix, and Hugo. Some of us worked together, having fun in the lab. And some of us are close friends in the daily life to cook, to drink, or to travel. I will always memorize and cherish the precious time we enjoyed together.

Finally, I would like to thank my parents as well as Junyan, who means a lot to me. Thanks for their supporting and giving me the greatest love.

Wanyu Si
Delft, September 2023

Abstract

Considering the rapidly growing energy demand in worldwide and climate deterioration caused by fossil fuel, the remarkable potential of solar energy has captured the attention of individuals and industries alike. Among different techniques, poly-Si based passivating contacts have shown great performance on solar cell application, which enabling a high efficiency of over 26%. Plasma-enhanced chemical vapor deposition (PECVD) as one of the promising technologies in a-Si contacting layer fabrication has gradually replaced the conventional LPCVD method in industry. However, the accompanied severe ion bombardment is not negligible, especially on its underlying fragile tunnelling oxide. In this work, the impact of PECVD a-Si:H contacting layer deposition on poly-Si/SiO_x passivating contact is investigated.

PECVD radio-frequency (RF) power for the contacting a-Si layer on the underlying SiO_x is the only variable in this project, varying from 5 W to 55 W, and pinhole density acts as a bridge to help analyse the intrinsic principles. Firstly, the results of a-Si:H thin film characterization suggest that with an increasing RF power, the a-Si:H thin film is grown at a higher deposition rate and becomes porous. In addition, the pinholes in tunnel oxide are inspected by applying the concepts of "selective etching" and "pinhole magnification". With a two-step five-point sampling method, it is shown that the effect of RF power on the pinhole density is not monotonically increasing. The highest value is found at 25 W. To explain this, a concept of "protective layer" is proposed, which is defined as a buffer layer (contacting layer) formed at the very beginning during a-Si:H deposition. It appears to be more effective when higher RF power (> 35 W) is applied. Another influence on tunnel oxide property is discussed according to the result from XPS measurement. The percentage of Si^{4+} species is found in the case of 25 W, corresponding to the highest pinhole density. This proves to some extent that the severe particle bombardment brought by strong power would weaken or directly break the Si-O bonds in the PECVD substrate, that is the tunnel oxide in our case.

As a result of thin film characterization, five factors contribute to pinhole formation: (i) Defects in tunnel oxide from imperfect oxidation leave potential for pinhole formation. (ii) Severe ion bombardments in PECVD deposition are allowed to weaken or break Si-O in SiO_x. (iii) Island growth of a-Si:H contacting layer makes the exposed region in tunnel oxide continue to be damaged. (iv) "Buffer layer" formation protects the substrate from ion bombardments. (v) The tensile stress applied by a-Si:H films during annealing intensifies the formation of pinholes.

Subsequently, an unexpected result from passivation quality assessment is that higher passivation level is presented with higher pinhole density. The best passivation quality is found in the case of 25 W, with J_0 of 3.3 fA/cm^2 and iV_{oc} of 714 mV. Further, a large optimal process window for RF power adjustment is found from 25 W to 35 W, which leads to an iV_{oc} over 710 mV, with single side J_0 below 3.5 fA/cm^2. The results from specific contact resistivity indicate that it is positively correlated to the pinhole density. Eventually, the champion passivating contact with a selectivity of 14.37 in this project is expected to yield a maximum efficiency of 28.9% in c-Si solar cell.

Contents

List of Figures

List of Tables

Nomenclature

Abbreviations

Abbreviation	Definition
TFC	Total Final Consumption
IEA	International Energy Agency
PV	Photovoltaic
TOPCon	Tunnel Oxide Passivated Contact
HJT	Heterojunction
IBC	Interdigitated Back Contact
c-Si	Crystalline Silicon
a-Si	Amorphous Silicon
a-Si:H	Hydrogenated Amorphous Silicon
RT	Room Temperature
ARC	Anti-Reflection Coating
SiO_x	Silicon Oxide
SiN_x	Silicon Nitride
TEM	Transmission Electron Microscope
NREL	National Renewable Laboratory
PECVD	Plasma-Enhanced Chemical Vapor Deposition
LPCVD	Low-Pressure Chemical Vapor Deposition
FZ	Float Zone
IPA	Isopropyl Alcohol
t-SiO_x	Thermal Silicon Oxide
RF	Radio-Frequency
FGA	Forming Gas Annealing
RTP	Rapid Temperature Annealing
OM	Optical Microscope
SEM	Scanning Electron Microscope
SE	Spectroscopic Ellipsometry
FTIR	Fourier Transform Infrared Spectrometer
XPS	X-ray Photoelectron Spectroscopy
EVC	Electrochemical Capacitance-Voltage
STC	Standard Test Condition
SRH	Shockley-Read-Hall
LSM	Low-Stretching Mode
HSM	How-Stretching Mode
BHF	Buffer Oxide Etch
NAOS	Nitric Acid Oxidation of Silicon
TMAH	Trimethyl Ammonium Hydroxide

Symbols

Symbol	Definition	Unit
E_G	Bandgap Energy	[eV]
λ	Wavelength	[nm]
h	Planck's Constant	[J·s]
c	Speed of Light	[m/s]
E_{ph}	Photon Energy	[eV]
R	Reflectance	[-]
n	Complec Refractive Index	[-]
T	Transmittance	[-]
α	Absorption Coefficient	[nm^{-1}]
A_{tot}	Total Area of the Solar Cell	[cm^2]
A_f	Uncovered Area	[cm^2]
C_f	Coverage Factor	[-]
η_v	Bandgap Utilization Efficiency	[%]
V_{oc}	Open-Circuit Voltage	[mV]
q	Charge of an Electron	[C]
J_{ph}	Photocurrent Density	[mA/cm^2]
T	Temperature	[K]
J_0	Saturation Current Density	[fA/cm^2]
η_{sj}	Single Junction Solar Cell Efficiency	[%]
FF	Fill Factor	[%]
J_{sc}	Short-Circuit Density	[mA/cm^2]
R_s	Series Resistance	[Ω]
R_{sh}	Parallel Resistance	[Ω]
V_{th}	Thermal Voltage	[mV]
ρ_c	Contact Resistivity	[$m\Omega \cdot cm^2$]
S	Carrier Selectivity	[-]
N	Charge Carrier Density	[cm^{-3}]
V_{mpp}	Maximum Power Point Voltage	[V]
J_{mpp}	Maximum Power Point Current Density	[mA/cm^2]
η	Efficiency	[%]
ER	Etch Rate	[nm/min]
D_{pin}	Pinhole Density	[cm^{-2}]
ω	Wavenumber	[cm^{-1}]
R^*	Microstructure Factor,	[-]
I_{LSM}	Integral Intensities of the Low-Stretching Mode	[-]
I_{HSM}	Integral Intensities of the High-Stretching Mode	[-]
R_T	Total Resistance	[$m\Omega$]
R_c	Contact Resistance	[$m\Omega$]
A_c	Total Area of Top Contact	[mm^2]

1

Introduction

This chapter projects to introduce the background of the thesis and some basic concepts related to solar cells. It provides general insight for better analysis of subsequent experimental results. The background to solar cell development is briefly illustrated in section 1.1, following by its working principle explanation and loss mechanisms analysis in section 1.2 and section 1.3, respectively. The forthcoming section 1.4 introduces fundamental concepts of passivating contact and the related techniques. Subsequently, section 1.5 and section 1.6 aim to elaborate the motivations and objectives of the project, which is finalized by an outline in section 1.7.

1.1. Background

Energy, as fundamental for supporting social production and human activities, has seen rapid growth in demand over the years. As reported, the global energy consumption growth slowed down in 2022 (+ 2.1%) but remained higher than its average 2010-2019 growth rate (+ 1.4%/year) [16]. To meet such a massive demand, conventional fossil fuels play a pivotal role by contributing in excess of fifty percent to the world's total final consumption (TFC). Seen from Figure 1.1 and Figure 1.2, this value reached 66.3% in the year of 2019, with a consumption of 277.2 EJ.

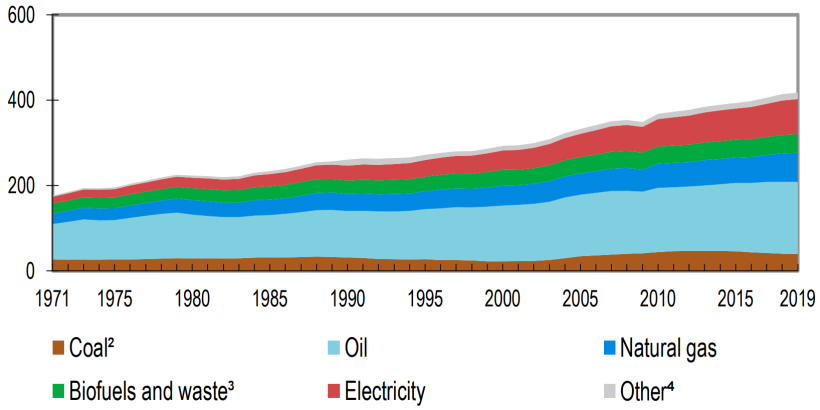

Figure 1.1: World total final consumption of energy (TFC) by source, 1971-2019. [30]

With the extensive consumption of fossil fuels, their mineral reserves continue to decline, resulting in rising fuel prices. In addition, its accompanying negative impact on climate change

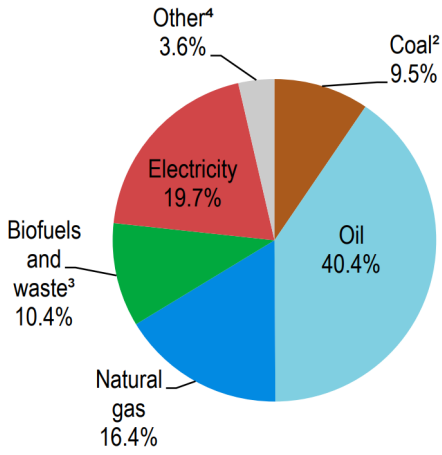

Figure 1.2: Share of world total final consumption of energy (418 EJ) by source, 2019. [30]

is another key issue. Thankfully, there is an increasing awareness of these matters, and various solutions have been proposed, such as reducing energy waste, or developing eco-friendly energy sources to replace traditional fuels.

Different renewable energy sources, such as wind energy, geothermal energy, biomass energy, and solar energy has gradually attracted more human attention. The sun is mainly composed of hydrogen and helium. In its center, huge pressure and high temperature provide good conditions for nuclear fusion to occur [80]. The continuous nuclear fusion reaction inside constantly radiates energy to the outside. Although the solar radiation that reaches the earth's atmosphere is only one in 2.2 billion of the total, the energy it contains is equivalent to that of 5 million tons coal. This indicates that solar energy has great potential for development. There are three methods of solar energy utilization, that are photothermal, photovoltaic, and photochemical conversion. And this project focuses on the second method, photovoltaic technology (abbreviated as PV).

Figure 1.3 demonstrates the anneal PV production by different technologies. As a semiconductor material, silicon has good photoconductivity. And because of its non-toxicity, stability, and huge deposits in the earth, Si-based solar cells have dominated the market since the development of solar cells. Furthermore, different structures and concepts have been applied on c-Si solar cells, including heterojunctions (HJT), tunnel oxide passivated contact (TOPCon), interdigitated back contact (IBC), etc. The record c-Si solar cell efficiency in the lab is 26.81% achieved by LONGI [42]. Although it champion efficiency is realized with a heterojunction structure, TOPCon solar cell is still regarded as the most promising technology, since it has high compatibility with the existing production line of most companies. Additionally, the theoretical efficiency limit of TOPCon solar cell is 28.7%, higher than that of HJT of 27.5% [73].

1.2. Working principle of the solar cell

Since the solar cell discussed in this thesis mainly refer to the c-Si based solar cell, the introduction will revolves around silicon. Before revealing the working principle of it, several concepts need to be clarified.

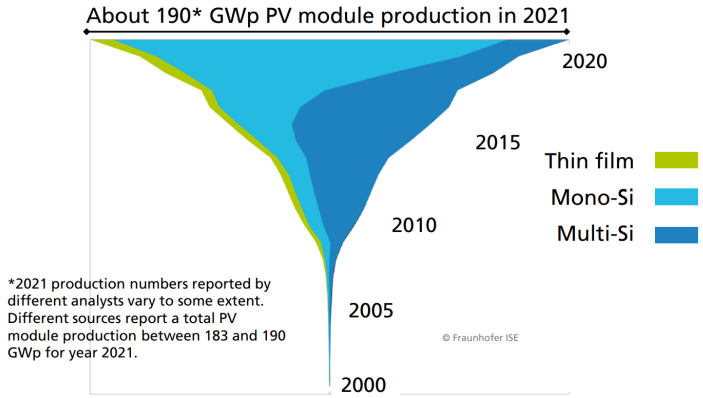

Figure 1.3: Annual PV Production by Technology. [64]

Intrinsic semiconductor

The electrons in the outermost shell of the atom are defined as valence electrons. There are 4 valence electrons in the outer shell of a silicon atom. In a silicon crystal, each atom has 4 adjacent atoms, and it shares 2 valence electrons with each adjacent Si atom, thus forming a stable 8-atom structure, seen as Figure 1.4.

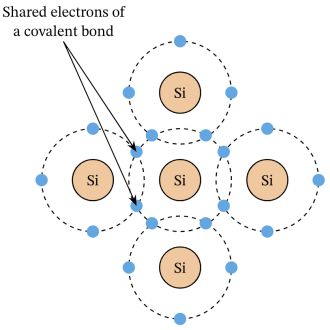

Figure 1.4: Schematic of intrinsic semiconductor. [54]

The electrons in the outer layer of the Si atom are less bound by the nucleus. When they get enough energy, such as illuminated of heated, they will get rid of the constraints of the nucleus and become free electrons, leaving a hole in the original position at the same time. Electrons are negatively charged, and holes are positively charged. In a pure silicon crystal, the number of free electrons and holes is equal.

At room temperature, the number of electrons and holes in pure silicon crystals is quite small, leading to a poor conductivity. Such pure crystal is called an intrinsic semiconductor.

N-type or P-type semiconductor

A doped semiconductor is formed when a small amount of an impurity, such as phosphorus, is doped into a pure silicon crystal. Since a phosphorus atom has 5 valence electrons, when a phosphorus atom forms a covalent bond with 4 adjacent silicon atoms, there is one more valence electron, which can easily break away from the attraction of the phosphorus nucleus and become free electrons. The silicon crystal doped with pentavalent elements becomes an electron-conducting semiconductor, also known as an N-type semiconductor, as shown in Figure 1.5a.

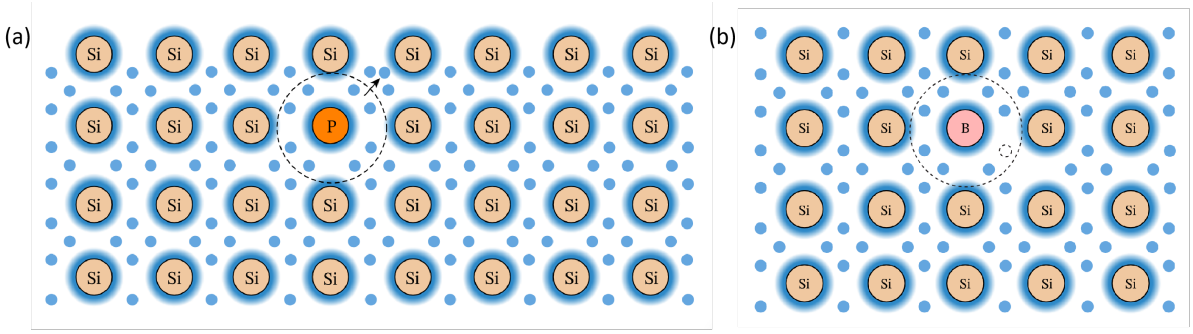

Figure 1.5: Schematic of (a) N-type semiconductor and (b) P-type semiconductor. [54]

In N-type semiconductors, apart from a large number of free electrons due to the impurities doped, there are also a small amount of electron-hole pairs caused by thermal excitation. However, the number of holes is relatively small compared to electrons, thereby they are called minority carriers, while the electrons are named majority carriers in N-type materials. Similarly, if a small amount of impurities, that is, trivalent elements, such as boron, are doped in a pure silicon crystal, a P-type material is formed. Since there are only 3 valence electrons, one valence electron is missing when B forms a covalent bond with the Si atom. At this time, a hole will appear, shown as Figure 1.5b. For P-type semiconductors, holes are the majority carriers and electrons are the minority carriers.

PN junction

If a P-type semiconductor and a N-type semiconductor are closely combined and integrated, the transition region between the two semiconductors with opposite conductivity types is called a PN junction. In the P-type region, there are many holes and few electrons, while in the N-type region, there are many electrons and few holes. Due to the concentration difference of electrons (or holes) formed between two region close to the interface, the electrons (or holes) will diffuse from N-type (or P-type) region to P-type (or N-type) region.

Diffusion movement is established based on the theory of mutual repulsion and collision of electrons. Electrons on the same level of orbit will automatically flow from places where electrons are relatively concentrated to places where electrons are rare. This flow does not require external electric fields. The diffusion rate is proportional to the concentration gradient.

The diffusion process is: in the N-type region near the interface, the electrons cross the interface and recombine with the holes in the P-type region, so that a group of negatively charged boron ions appear in the P-type region. At the same time, in the N-type region, due to the loss of a batch of electrons, positively charged phosphorus ions appear.

As a result, a region occupied with positively charged ion is formed on one side of the interface, and another region occupied with negatively charged ion is formed on the other side of the interface, which is called a space charge region (or depletion region). This is the PN junction, which is a very thin layer.

In the PN junction, due to the accumulation of negative charges and positive charges on both sides, an electric field from the positive charge to the negative charge will be generated, that is, the electric field from the N region to the P region, which is called the built-in electric field, seen as Figure 1.6.

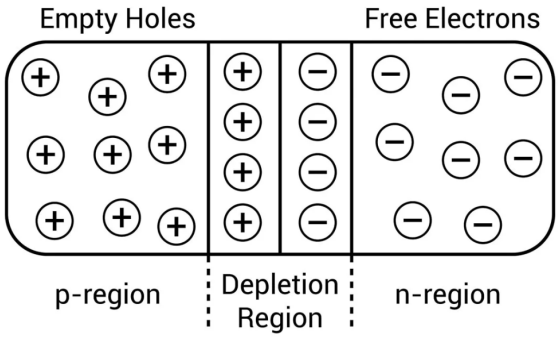

Figure 1.6: Schematic of PN junction. [14]

Photovoltaic effect

An energy of 1.12 eV is required to separate an electron from the valence electron shell of the Si atom at room temperature, and this energy is called the bandgap energy of Si. The separation process is called excitation, and the separated electrons are free electrons, which is free to move and carry electric current. When a semiconductor is illuminated by sunlight, photons with energy greater than the bandgap of the semiconductor will excite the valence electrons of atoms to become free electrons, forming photogenerated electron-hole pairs, namely photogenerated carriers.

The core composition of solar cells is the PN junction. Photogenerated electron-hole pairs will be generated in the P-type region, space charge region and N-type region, and migrate in all directions due to thermal motion.

The photogenerated electron-hole pairs which are generated or migrated in the space charge region would be separated by the built-in electric field. Then the photogenerated electrons are drifted into the N-type region, and the photogenerated holes are drifted into the P-type region. In the depletion region, the total carrier concentration is approximately zero. On the other hand, in the N region (P region), after the electron-hole pairs are generated, they will diffuse to the PN junction boundary. Once reaching the boundary, they will be immediately affected by the built-in electric field and drift. The photogenerated holes (photogenerated electrons) cross the space charge region and enter the P region (N region), while the photogenerated electrons (photogenerated holes) are left behind.

Therefore, the accumulation of positive and negative charges is formed on both sides of the PN junction, forming a photogenerated electric field opposite to the direction of the built-in electric field. In addition to partially offsetting the built-in electric field, this electric field also makes the P-type layer positively charged, and the N-type layer is negatively charged, thus generating a photo-generated electromotive force. This is the ”photovoltaic effect”.

Solar cell working principle

Solar cell consist of PN junction, passivating thin films and metal electrodes. The whole working procedure can be divided into three processes: electron-hole generation, separation and collection. When illuminated, the photogenerated carriers are generated by absorbing energy, then separated by the built-in electric field formed with PN junction, and finally collected by electrodes on front or back side.

1.3. Loss mechanisms in solar cell

This section aims to analyse the factors that affect the conversion efficiency of crystalline silicon solar cells. They mainly come from two aspects, namely optical loss and electrical loss. They will be introduced in detail below.

1.3.1. Optical losses

Optical losses consists of five components. These are spectral mismatch, reflection, incomplete absorption, surface shading, and parasitic absorption.

Spectral mismatch

Losses of spectral mismatch include two parts: thermalization and non-absorption. Since no energy state exists in the bandgap, only the photon with an energy higher than absorber's bandgap energy E_G will be absorbed and generate a pair of electron-hole. In the case of c-Si solar cell, with a bandgap of 1.12 eV, according to the Equation 1.1, only the light with the wavelength shorter than 1107 nm will contribute to the electron-hole pair generation.

$$E_{ph} = \frac{hc}{\lambda} \tag{1.1}$$

where λ is the light wavelength, h is Planck's constant of 6.626×10^{-34} J·s and, c is the speed of light which is 2.998×10^{8} m/s. The light with a wavelength longer than 1107 nm will not be absorbed, namely non-absorption loss, shown in Figure 1.7a. However, although the shorter wavelength light (< 1107 nm) will be absorbed, the extra energy $(E_{ph} - E_G)$ will be released thermally into the lattice, which is called thermalization, shown in Figure 1.7b.

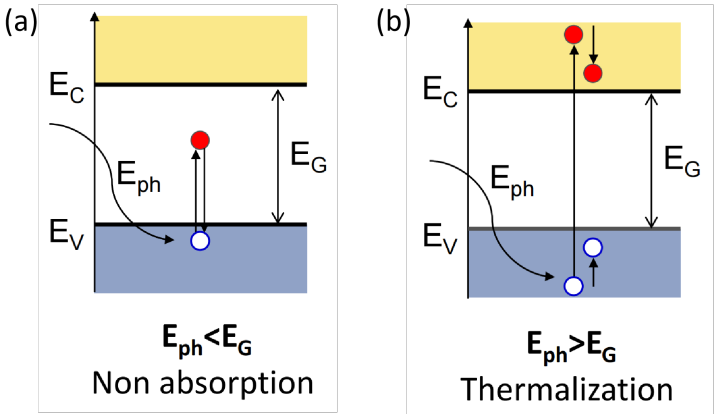

Figure 1.7: (a) Illustrating the non-absorption loss when photon with energy E_{ph} is lower than bandgap energy of semiconductor E_G. (b) If $E_{ph} > E_G$, a part of energy is thermalized. [80]

Reflection

When the light arrives at the interface of two different media, a part of it will be reflected, and the others are transmitted. The energy of light which is reflected is then lost. The refractive index varies from one medium to another. According to Equation 1.2, a bigger gap between two substances will lead to a more prominent reflection.

$$R = |\frac{n_1 - n_2}{n_1 + n_2}|^2 \tag{1.2}$$

where n_1 is the complex refractive index of the surroundings and n_2 is the complex refractive index of Si.One method to reduce the reflection is depositing an anti-reflection coating (ARC) on the surface side where the light enters. In addition, another method is utilizing the concept of total reflectance. When the light is incident from a medium with a small refractive index to a medium with a large refractive index, and with an incident angle greater than a certain value, all the incident light will be refracted into the second medium. Since the refractive index of air is smaller than Si, it is possible to realize total reflectance by changing the Si surface morphology, that is texturing, shown as Figure 1.8.

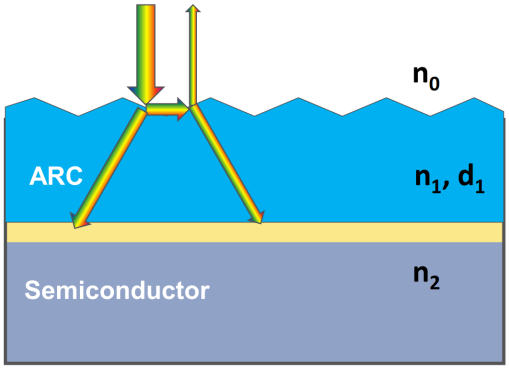

Figure 1.8: Reduced surface reflection by applying ARC thin film and surface texturing. [80]

Incomplete absorption

Not all light that successfully passes through the front surface would remain in and be absorbed by the substrate. Because of the limited thickness of the absorber, part of the light with the longer wavelength will directly pass through the back of the absorber, as shown in Figure 1.9. The transmitted light can be calculated as Equation 1.3.

$$T = e^{(-\alpha d)} \tag{1.3}$$

where T is the transmittance, α is the absorption coefficient, and d is the thickness of the absorber. As a result, the thickness of the absorber can be appropriately increased to reduce the loss caused by incomplete absorption.

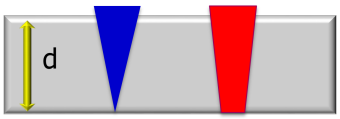

Figure 1.9: Light in blue shows the maximum wavelength that can be absorbed with a substrate thickness d, while light in red will directly pass the back, which is lost. [80]

Surface shading

In the most of structure, metals as the electrode will be applied on the front side of the solar cell, shown as Figure 1.10. In this case, it will reflect almost all light arriving at this area. Thus the area covered by the front electrode has to be deducted from the active area of the solar cell. If determine the all area of the solar cell as A_{tot}, and the uncovered area as A_f, the so-called active area coverage factor C_f is calculated as:

$$C_f = \frac{A_f}{A_{tot}} \tag{1.4}$$

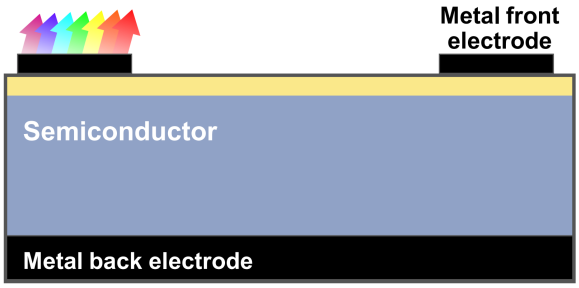

Figure 1.10: Optical loss caused by surface shading at the front electrode area. [80]

Parasitic absorption

To improve the efficiency of the solar cell, various thin films are fashioned on the top or rear. Actually, those films are not ideal and would absorb part of the incident light. However, all the absorption that does not occur in the absorber is regarded as a kind of loss, namely parasitic absorption.

1.3.2. Electrical losses

Electrical losses contain bandgap utilization, radiative recombination, Shockley-Read-Hall recombination, Auger recombination, surface recombination, and resistive losses and shunt losses.

Bandgap utilization

For a PN junction at open-circuit condition at 1 sun (as Figure 1.11), the bandgap utilization efficiency is η_v, as a function of open-circuit voltage V_{oc}, shown as Equation 1.5 and Equation 1.6.

$$\eta_v = \frac{qV_{oc}}{E_G} \tag{1.5}$$

$$V_{oc} = \frac{kT}{q} ln(\frac{J_{ph}}{J_0} + 1) \tag{1.6}$$

Where q is the charge of an electron, k is the Boltzmann constant, T is the temperature in Kelvin, J_{ph} is photocurrent density, and J_0 is the saturation current density, which can be decreased but never be zero. Therefore, the bandgap utilization is:

$$\eta_v(E_G) = \frac{kT}{q} ln(\frac{J_{ph}(E_G)}{J_0(E_G)} + 1) \tag{1.7}$$

And the maximum efficiency for single junction solar cell is given as:

$$\eta_{sj} = \eta_{ult}\eta_v FF \tag{1.8}$$

FF is the fill factor and defined as Equation 1.9. J_{mpp} and V_{mpp} are the current density and voltage at the maximum power point, respectively. J_{sc} is the short-circuit current density.

$$\eta = \frac{J_{mpp}V_{mpp}}{J_{sc}V_{oc}} \tag{1.9}$$

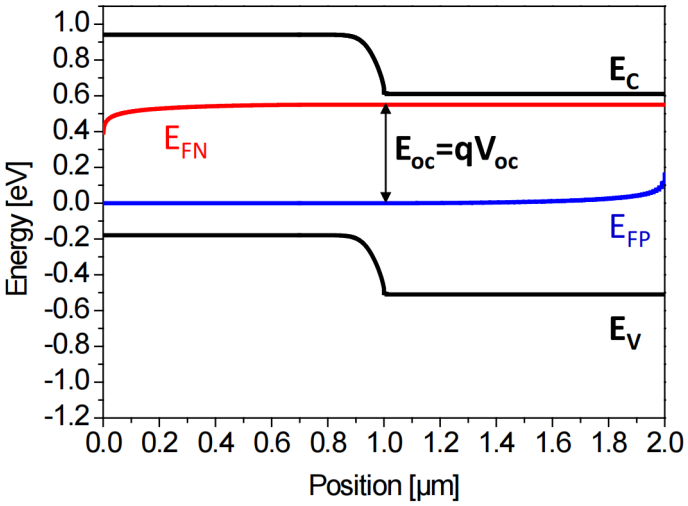

Figure 1.11: Band diagram of PN junction at open-circuit condition at 1 sun. [80]

Radiative recombination

When electrons in the conduction band meet and recombine with holes in the valence band, the excess energy is emitted as photons, which is the reverse process of photogenerated carriers. For direct semiconductors, it is the main way of recombination in the bulk. However, for Si with an indirect bandgap, radiative recombination requires the participation of phonons. Therefore, radiation recombination is relatively small, and it does not play a leading role in the recombination of crystalline silicon solar cells.

Shockley-Read-Hall recombination

Shockley-Read-Hall recombination is facilitated by an impurity atom or lattice defects, which create unexpected energy states during the band gap. These energy states will become centers of recombination. Electrons and holes recombine through trap states in the band gap, and electrons in the conduction band can jump to the valence band through these recombination centers. The recombination rate in this case is thereby proportional to the concentration of the dopants, carrier lifetime and defects.

Auger recombination

When an electron and a hole recombine, the energy generated by the recombination will be transferred to another electron or hole. The third particle has enough kinetic energy to ascend to a higher energy state, and then radiate to the lattice in the form of phonons during the relaxation time. This is the so-called Auger recombination, known as the not-radiative three-particle process. Its recombination rate is related to the concentration of carriers, and it is the main recombination mode in the high doping concentration region. All three kinds of recombination can be demonstrated as Figure 1.12.

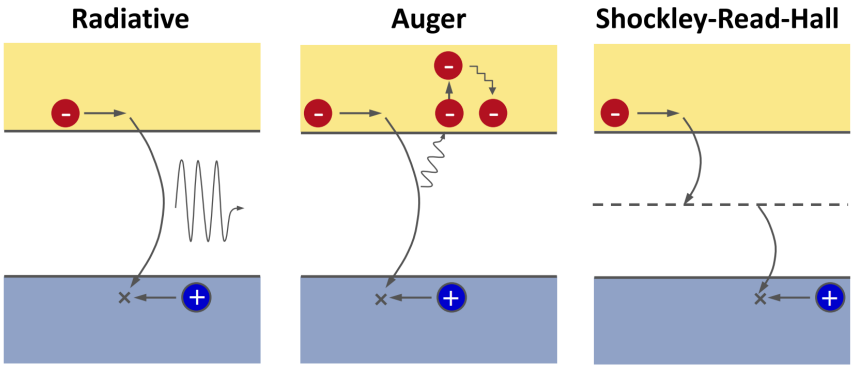

Figure 1.12: Band diagram of PN junction at open-circuit condition at 1 sun. [80]

Surface recombination

There are also a large number of defects such as dislocations, dangling bonds, and lattice defects on the surface of crystalline silicon, which lead to carrier recombination. This recombination can be described by the SRH model.

Resistive losses and shunt losses

Actually, the problem of parasitic resistance such as series resistance R_s and parallel resistance R_{sh} will also be encountered. R_s is derived from the resistance of the current flow direction of the large-area solar cell and the contact resistance of the metal grid lines. The parallel resistance R_{sh} comes from the PN junction structure and the process in the cell fabrication.

The origin of series resistance R_s is a bit more complicated. As shown in Figure 1.13, it mainly consists of the bulk resistance of Si (R_{base}), the contact resistance (R_c), resistance of finger and busbar (R_{finger} and R_{busbar}), and the emitter resistance ($R_{emitter}$). The value of series resistance has a strong correlation with the fill factor of the cell. When the series resistance is too large, the fill factor decreases.

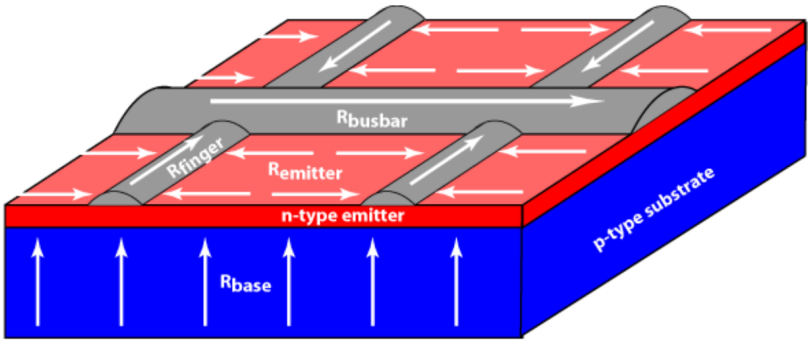

Figure 1.13: Series resistive components and electron flow in a solar cell. [67]

The cause of parallel resistance is relatively simple. it is generally believed that it is generated at the edge of c-Si solar cells. Taking the n-type silicon wafer as an example, since the holes in the emitter can recombine with the electrons in the bulk region or even the back electrode through the surface state, a current channel is generated, resulting in partial leakage of the cell. Inappropriate process can also lead to the formation of parallel resistance, including

edge leakage, edge PN junction residue, PN junction burn-through, surface scratches, metal contamination of the front surface, severe crystal damage, etc..

Both the increase in series resistance and the decrease in parallel resistance have a great impact on the fill factor of the solar cell. Under the same magnitude of change, cell efficiency is more sensitive to series resistance compared to parallel resistance. As illustrated in Figure 1.14, when the series resistance changes greatly, the short-circuit current J_{sc} gradually decreases, and the open-circuit voltage V_{oc} remains same. On the other hand, when the parallel resistance becomes smaller, the J_{sc} remains basically unchanged, while V_{oc} drops significantly. This is because parallel leakage will increase the additional recombination of the cell, and the V_{oc} is quite sensitive to recombination.

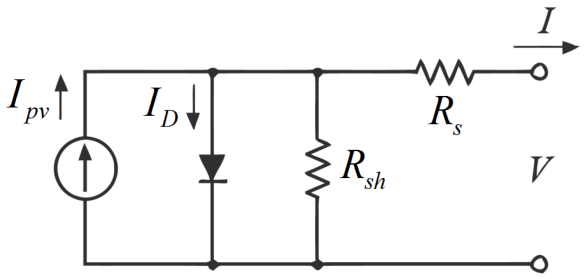

Figure 1.14: Equivalent circuit of a solar cell. [67]

1.4. Carrier-selective passivating contact

Carrier-selective passivating contact in TOPCon structure mainly consists of two essential layers, which are an interfacial tunnel SiO_x layer and the doped poly-Si layer.

1.4.1. Interfacial tunnelling oxide

This subsection aims to analyse the role of interfacial tunnelling oxide in a passivating contact. The required features of tunnelling contact layer will be studied at the beginning. The second part refers to the introduction of tunnelling oxide, including the carrier transport mechanism and its physical characteristics, which is followed by three fabrication methods.

Tunnelling contact layer requirement

A qualified passivating contact is supposed to combine an excellent interface passivation effect with a low contact resistance. Therefore, the selection of materials for the tunnelling contact layer is extremely strict. (i) The material is responsible for passivating the dangling bonds on the surface of bulk Si. It is also preferable if hydrogen can be implanted during the material preparation to passivate the defects in the bulk at the same time. In addition, it will be beneficial if there is a field-effect passivation provided. (ii) The tunnelling effect if contained will assist in the efficient transport of majority carriers between the absorber and the doped layer.

The material of the tunnelling layer in the passivating contact typically includes Al_2O_3, SiO_2, a-Si:H, SiN_x, etc. [13]. Considering the ability for interface defects passivation and field-effect passivation, a-Si:H thin film is the most ideal selection. However, due to parasitic absorption and poor thermal stability, currently, SiO_2 has been widely studied and applied on c-Si solar cells.

Carrier transport mechanism in tunnelling oxide

Two transport mechanisms known as “pinhole” and “tunnelling” are proposed to describe the carrier transport in the oxide layer. The exist of pinhole has been proved to some extent by that a reduced contact resistivity was achieved by applying an increasing annealing temperature over 900°C, while the interfacial oxide seemed to be continuous via Transmission Electron Microscope (TEM) [18]. Nevertheless, the single pinhole mode cannot perfectly explain why contact resistivity remains the same when annealing at 700°C and 800°C separately. For this, Steinkemer et al. created a model of “quantum mechanical tunnelling” and stated that the ultra-thin oxide might only contain the tunnelling mechanism [83]. To conclude, for an interfacial oxide thinner than 2 nm, both the ‘pinhole mode” and “tunnelling mode” would coexist. The domination between them depends on the oxide stoichiometry, thickness as well as annealing temperature applied.

Physical characteristics of tunnel oxide

SiO_2 has been subject to a series of researches. It is found that Si/SiO_2 interface features a very low interface state density (D_{it}), highly asymmetric capture cross sections ($\sigma_n = 100 \times \sigma_p$), and a low positive fixed charge density (D_f), which leads to a small shift of the flat-band voltage (V_{FB}) [25][3][1][15]. As a calculation, the surface recombination velocity, S, is quite low at the interface, since S is negatively correlation to D_{it}, σ_n and σ_p [3]. Further, thanks to the asymmetry of electron and hole capture cross-section, S has a weaker dependence on the excess carrier density, yielding lower surface recombination at the Si/SiO_2 interface.

On the other hand, however, the low density of fixed charge, there is only chemical but no field-effect passivation provided by SiO_2. Even though some reports demonstrated that applying an external voltage [95][2] or depositing corona charges [24][74][35] will induce field-effect passivation in SiO_2, this is currently not available in practical devices.

Apart from the chemical passivation provided in the passivating contact, tunnel SiO_2 alsoseparates the doped poly-Si from c-Si, which can significantly reduce the Auger recombination in c-Si region near the interface. Subsequently, since tunnel oxide presents different barrier for holes (4.5 eV) and electrons (3.1 eV) [41], electrons can selectively pass through at the interface, forming a carrier selective passivating contact.

Fabrication methods of tunnelling oxide

There are many ways to prepare SiO_x. Primarily, the HNO_3 oxidation method (NAOS) is to immerse the wafer in the HNO_3 solution at room temperature or higher to form the NAOS-SiO_x. Utilizing the strong oxidation of HNO_3 solution, the thickness and density of the SiO_x layer can be adjusted by controlling the immersion time and solution temperature as well as the HNO_3 concentration. This process is relatively easy to operate and low in cost, which is a preferable method for 1-2 nm thick SiO_x fabrication. In year of 2015, it is proved that SiO_x can grow in ozonated water or ozone-ambient, which has enhanced thermal stability compared to NAOS in silicon solar cells, especially on textured surfaces [52]. Moreover, another kind of method named thermal oxidation was realized by the National Renewable Laboratory (NREL) in 2014. They formed a 1.5 nm tunnelling oxide layer with an oxidation temperature of 700°C by O_2 [84]. Cooperating with the subsequent doping of polysilicon, the reverse saturation current density at the passivation area is finally less than 10 fA/cm^2, and the iV_{oc} of the solar cell reaches 700 mV. SiO_x grown by thermal oxidation is a reliable solution for industrialization because the process is controllable and the equipment is compatible with the traditional

crystalline silicon cell production line.

1.4.2. Doped poly-Si layer

Thickness is one of the critical parameters in doped poly-Si. By changing the thickness from 60 nm to 200 nm, it was found that the doping concentration experienced a small variation. And the changes in sheet resistance were less than 20 Ω, meaning that the difference of field-effect passivation induced by different poly-Si is limited, as long as with a thickness exceeding 15 nm to guarantee enough lateral conductivity. If the impact of subsequent metallization is considered, the thickness of poly-Si is required to be large enough to resist the damage caused by different methods, such as the penetration of Ag paste during firing. However, thicker poly-Si would result in more parasitic absorption, thus reducing the short-circuit current density.

Another factor is the doping concentration. Higher concentration induces a high energy band barrier with respect to c-Si, contributing to the carrier-selective passivating contact formation. Apart from reducing the contact resistivity with metal, during the dopant diffusion process, a small amount of phosphorus atoms are supposed to enter the bulk Si to prompt field-effect passivation caused by the concentration difference on c-Si surface. In contrast, the severe parasitic absorption and Auger recombination are always along with the larger dopant concentration. Therefore, a balance of interfacial passivation and contact performance needs to be taken into account.

As the primary process in poly-Si fabrication, a-Si is commonly grown via two methods. One is physical vapor deposition, known as PVD process, including thermal evaporation, electron beam evaporation, sputtering, etc.. The other is chemical vapor deposition, abbreviated as CVD, containing metal-organic chemical vapor deposition (MOCVD), plasma enhanced chemical vapor deposition (PECVD), low-pressure chemical vapor deposition (LPCVD), atmospheric pressure chemical vapor deposition (APCVD) and hot wire chemical vapor deposition (HWCVD). Among them, PECVD and LPCVD are investigated in this thesis.

Through the high-temperature annealing process, a-Si begins to transform into poly-Si. The dopant atoms in poly-Si are activated by obtaining enough energy from the thermal budget, and part of them diffuse into bulk Si, enhancing the field-effect passivation. The annealing process can be achieved by a traditional tube furnace. By adjusting the temperature ramping profile, annealing temperature, as well as annealing duration, different doping profiles will be realized. Another method for annealing is the rapid thermal annealing (RTA). Due to the large ramping rate of the temperature, it will take only a quarter of the time to achieve a result close to that of traditional annealing. However, the passivation quality of RTA-treated sample is still inferior to that with annealing.

1.4.3. Surface passivation with dielectrics

Carrier selectivity is one of the basic requirements for solar cells, which assists the electron-hole separation described in section 1.2. The core concept is to allow one kind of charge carrier to transport but block the other carriers [100]. It relies on a combination of qualified passivation quality and low contact resistance between the contacts with c-Si and the contacts with metals. The passivation mechanism contains two parts. Primarily, chemical passivation is achieved by the minimized dangling bonds and reduced state density on the surface or at the interface. Owing to low interface state density and capture cross section for electrons and

holes, SiO_2 shows excellent behaviour on chemical passivation.

On the other hand, some materials, such as SiN_x and Al_2O_3, have plenty of positive or negative fixed charges inside. They will repel another kind of charge carriers to get close to in the underlying silicon, thereby reducing the surface recombination velocity at their interface. This mechanism is known as field-effect passivation, which can be realized by a highly phosphorous-doped poly-Si layer formed on top of n-type c-Si in this project. In addition to reducing the recombination by passivation, a good conductivity of the contact is supposed to be achieved, allowing the majority of carriers to pass through and be collected by electrodes on the surface. Thinner tunnel oxide and higher doping concentration in poly-Si will contribute to lower contact resistance between the bulk Si and electrode metal.

To quantify the carrier selective ability, Schmidt et al. provide an efficient method to visualize it. Based on its principle, that is related to the resistance which the selective layer has for majority carriers and minority carriers, respectively, selectivity can be behaved as:

$$S = \frac{V_{th}}{\rho_c J_0} \tag{1.10}$$

where V_{th} is the thermal voltage which is a constant value at room temperature, ρ_c is the contact resistivity of passivating contact, and J_0 is the recombination current density. For a more intuitive comparison, a logarithmically scaled selectivity is commonly used:

$$S_{10} = log_{10}(S) = log_{10}(\frac{V_{th}}{\rho_c J_0}) \tag{1.11}$$

As seen from Equation 1.11, carrier selectivity is only related to the contact resistivity and recombination current density.

1.5. Motivations

As described in section 1.4, owing to outstanding properties, tunnel oxide can provide great chemical passivation, largely reduce the Auger recombination caused by dopants in-diffusion, and efficiently prevent holes from passing through due to the different barriers for electrons and holes. In addition, the heavily doped poly-Si enhances the field-effect passivation by forming a high/low work function with c-Si, which can repel the minority carriers away from the interface. Furthermore, phosphorous has a lower diffusion coefficient than boron, which can help improve passivation quality. As a result, n^+ poly-Si/SiO_x stack is chosen as a carrier selective passivating contact in this project.

Compared to the conventional a-Si growth method by LPCVD, PECVD allows single-side deposition, higher deposition rate, and lower working temperature, which is greatly beneficial for large-scale mass production in industry. Another important superiority of this method is that the in-situ doping process can be realized more efficiently via PECVD.

However, the plasma-enhanced technology of PECVD will bring extra ion bombardment to the SiO_x and Si substrate. Since the tunnel oxide as the top layer of the substrate is quite fragile and has a thickness of only around 1.4 nm thick, it is hard to prevent any damage from the surroundings. Because of the impact of ion bombardment during PECVD deposition, the

properties of tunnel oxide have the potential to be modified, thus showing complex behaviours on carrier selectivity in passivating contacts.

1.6. Objectives

Based on the motivation described above, the objectives of this project mainly focus on three points. The primary is to study the influence of PECVD a-Si:H contacting layer deposition on thin film characteristics. It contains the impact of a-Si:H thin film and the underlying tunnel oxide, which is studied experimentally and from the literature. Subsequently, the formation of pinholes in tunnel oxide is investigated from the experimental results combined with principle basics from literature. Eventually, the impact of PECVD a-Si:H deposition on carrier selectivity of the formed passivating contact needs to be analyzed. Here, we use the LPCVD as a control sample for the contacting layer since the kinetic energy of poly-Si particles is negligible compared to PECVD counterpart.

1.7. Outline

The thesis report consists of four main components: the introduction, experimental processes, results and analysis, and finally the conclusion and outlook. In chapter 1, a general background of solar cell development and related basic principles are introduced. Then, the content referring to experimental methods and techniques utilized in this project are illuminated in chapter 2. In following chapter 3, the experimental results of Si thin film contacting layer characterization are demonstrated and analyzed. Chapter 4 presents the impact of PECVD a-Si:H contacting layer deposition on the whole passivating contact performance. Finally, the conclusions and outlooks are given in chapter 5.

2

Experimental methods and Process techniques

This project is to investigate the impact of PECVD a-Si:H deposition on the passivating contact. In the target contact, two thin films, tunnel oxide and poly-Si, are expected to cooperate with each other, constituting a thermal-SiO_x/n^+ poly-Si stack and yielding a high carrier selectivity. The only variable in the experiments is the radio-frequency (RF) power, which is one of the essential parameters in of PECVD method during the hydrogenated intrinsic amorphos silicon deposition after the tunnel oxide formation. The deposition, therefore, not only changes the properties of the a-Si:H, but also has potential effects on the underlying SiO_x, finally influencing the passivating contact performance.

In general, the experimental part of the project consists of two parts, the investigation of a-Si:H and SiO_x thin films characteristic, and the characterization of the formed passivating contact. The schematic of the project structure is demonstrated in Figure 2.1. To achieve this, several kinds of samples are fabricated and then analyzed by different characterization methods adopting specific flowcharts.

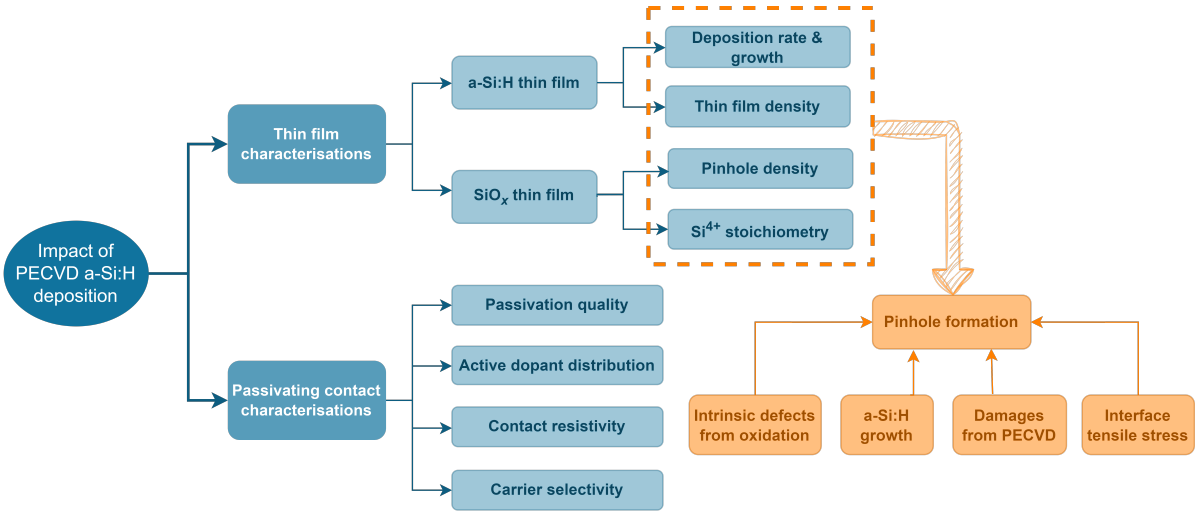

Figure 2.1: Schematic of project structure.

In this chapter, the sample fabrication process is illustrated in section 2.1, containing the process techniques and equipment required. It is then followed by an introduction of characterization for both thin film and passivating contact analysis.

2.1. Sample fabrication process

This section mainly revolves around parts of techniques in passivating contact formation and the specific instruments will be introduced combined with their schematic diagrams. In addition, different flowcharts are designed for four kinds of samples and interpreted as graphs.

2.1.1. Process techniques and equipment

Wafer characteristics

There are two types of wafer used in this project. For the general measurements, such as SiO_x property study and contact passivation quality evaluation, the double-side polished wafers manufactured by TOPSIL company are used. However, for the case of FTIR measurement, a kind of much thicker wafers from SIEGERT WAFER company are selected. The comparison of characteristics between these two types of wafer are summarized in Table 2.1.

Table 2.1: Comparison of two kinds of wafers selected for different purposes

Parameters	**TOPSIL**	**SIEGERT WAFER**
Diameter	99.6-100.2 mm	99.7-100.3 mm
Growth	Float zone (FZ)	Czochralski growth (CZ)
Type/Dopant	N/Phosphorous doped	N/Phosphorous doped
Orientation	<100>$\pm 1°$	<100>$\pm 0.5°$
Resistivity	1-5 Ω·cm	10-20 Ω·cm
Thickness	280 $\pm$ 20 μm	525 $\pm$ 20 μm
Surface finish	Double-side polished	Single-side polished

Two kinds of wafers are both with $\sim$100 mm diameter, phosphorous doped, and <100> orientation. However, since FTIR measurement relies on detecting the absorption of infrared light, thicker silicon wafers with a thickness of around 525 μm are used. Further, in order to reduce the interference of impurities and obtain pure peaks, high resistivity is also required. Thus, the wafers from SIEGERT WAFER with a higher resistivity of 10-20 Ω·cm are suitable.

Cleaning process

Contaminants are always not expected to present on the wafer surface, since the caused recombination will significantly degrade the sample performance. Organic or inorganic contaminants from air exposure or other issues need to be removed in the cleaning process.

The standard cleaning line in the EKL lab contains two steps. The first is to immerse the wafers into 99% HNO_3 for 10 min at room temperature, then followed by a 5 min DI water rinsing. The aim of it is to prevent the surface organic contamination. The next step is using a lower concentration HNO_3 of 69.5% at a high temperature of 110°C to remove the metal ions, with a 5 min rinsing with DI water as well.

After drying them in a spin dryer, there is already a thin silicon oxide formed on the surface, owing to the nitric acid oxidation during the cleaning process (as Equation 2.1 and Equation 2.2) [51] and the native oxidation by the atmosphere (as Equation 2.3).

$$4HNO_3 \rightarrow 4NO_2 + 2H_2O + O_2 \tag{2.1}$$

$$2NO_2 + Si \rightarrow SiO_2 + 2NO \tag{2.2}$$

$$O_2 + Si \rightarrow SiO_2 \tag{2.3}$$

To control the tunnel oxide quality, a wet etch step is required to remove the native oxide as well as protect the wafer surface from further oxidation in the atmosphere. Marangoni is used to realize it. The wafer in the Marangoni instrument is first etched by 0.55% HF for 4 min, based on the chemical reaction as Equation 2.5 [51][66], after which is a 5 min DI water rinsing. Then isopropyl alcohol (IPA) vapor replaces N_2 gun to gently remove the water from the wafer surface and reduces particle counts with the Marangoni effect. The treated wafer will always exhibit a better passivation performance as compared.

$$SiO_2 + 6HF \rightarrow H_2SiF_2 + 2H_2O \tag{2.4}$$

Tunnel oxide formation

The ultra-thin tunnelling silicon oxide in this project is prepared via the thermal oxidation method. It is performed with the assistance of a horizontal TEMPRESS furnace, whose schematic is shown in Figure 2.2. After the cleaned wafers are inserted into the boat slots, the program is conducted for thermal oxidation. Apart from the boat-in and boat-out steps, there are two main steps. In the beginning, the furnace temperature ramps up until it reaches 675°C in the nitrogen atmosphere. Then, the most critical process starts, when the oxygen is fed into the tube with a gas flow ratio of 10 (6 SLM for N_2 and 0.6 SLM for O_2). This process will continue for 3 min and the wafer is oxidated as Equation 2.3. The thickness of SiO_x layer prepared in this way is expected to be around 1.43 nm which is fitted by a spectrum ellipsometer.

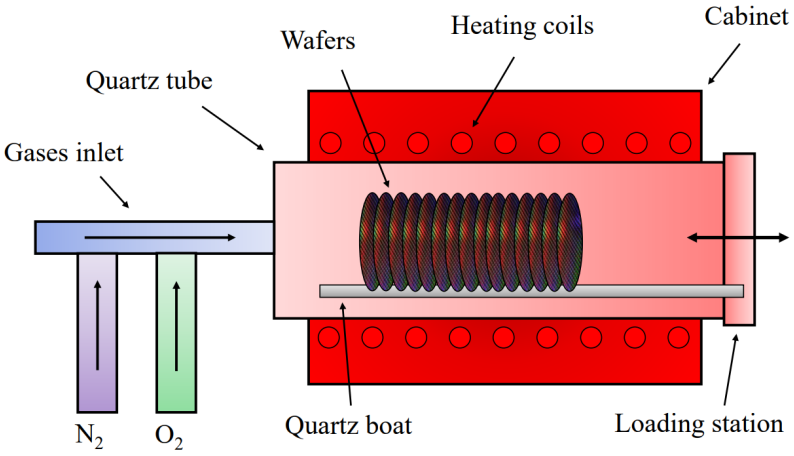

Figure 2.2: Schematic of thermal oxidation furnace. [79]

Low-pressure chemical vapor deposition

To fabricate a reference group, the intrinsic a-Si of one group sample needs to be produced by LPCVD. The horizontal furnace is again manufactured by TEPRESS furnace but with a LPCVD system. As schematically shown in Figure 2.3, the gas flow direction is opposite to that in normal furnaces, due to the pump at the backside. After the wafer loading and boat-in process, the tube will first be pumped down for several minutes until the pressure is reduced to 150 mTorr. The following procedure is heating the chamber to 580°C. Such high temperature is prepared for the subsequent chemical reaction driven by high thermal. SiH_4 as the precursor gas for a-Si deposition will be decomposed into several radicals, and finally form poly-Si on the substrate. The overall chemical reaction is simplified as Equation 2.5 [75].

$$SiH_4(g) \rightarrow Si(s) + 2H_2(g) \tag{2.5}$$

As calculated, the deposition rate of flat wafers with this recipe is about 2.1±0.1 nm/min. The deposition process is maintained for 10 minutes, yielding a 20 nm intrinsic a-Si layer. It is followed by a 60 min annealing at 600°C, in order to release the stress in a-Si. It is worth noticing that LPCVD allows double-side deposition and can process a large number of wafers per time, depending on the number of boat slots on the paddle.

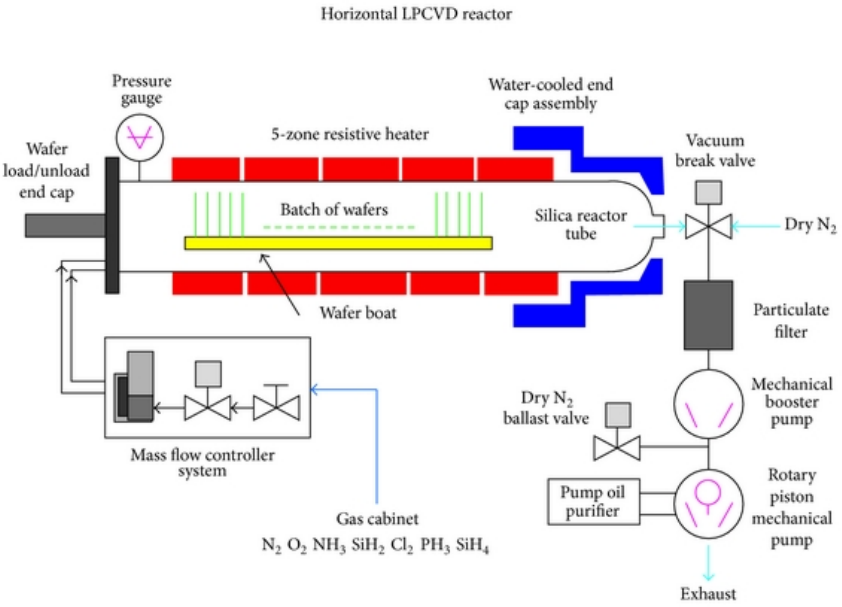

Figure 2.3: Schematic of LPCVD equipment. [75]

Plasma-enhanced chemical vapor deposition

Compared to LPCVD method, the PECVD has become widely used in thin film deposition, due to allowing single-side deposition, higher deposition rate and lower working temperature. As described in Figure 2.4, an electrode connected with a radio frequency generator, another ground-connected electrode and a fast alternating electric field (called plasma zone) between these two parallel electrodes together constitute the basic structure of PECVD equipment.

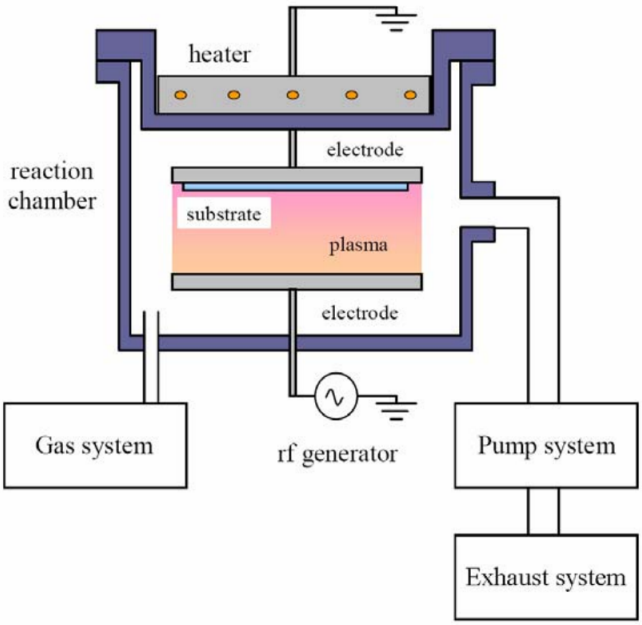

Figure 2.4: Schematic of PECVD equipment. [50]

One critical concept in the PECVD system is referring to the precursor gas decomposition. Under normal atmospheric conditions, a large number of so-called free electrons exist in the air at sea level, whose density is about 10^6 m^{-3} [43]. Similar free electrons also present in the chamber with a low pressure and play an important role in PECVD deposition. After RF power turned on, a strong electric field up to 10^4 V/m is formed between two electrodes. Then the free electrons decompose the electrically neutral gas molecules in the chamber through electron collision reactions under the acceleration of the electric field, producing charged ions and electrons. Normally, on a time scale of about 10^{-8} seconds after ignition, the cascade reaction in Figure 2.5 dominates, and the electron density in the chamber increases exponentially during this time interval. With the accumulation of charges on the two substrates, the electric field intensity felt by the plasma zone will be strongly shielded. Finally, a stable plasma will be formed, whose macroscopic color will gradually become stable.

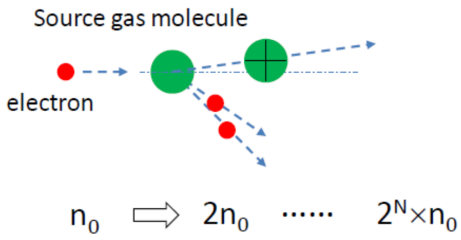

Figure 2.5: Schematic diagram of cascade reaction. [43]

The plasma is composed of neutral atoms or molecules, negative electrons and positive ions, which is a kind of regional electrolytic gas, namely local ionized gas. There are two types of collisions in plasma, elastic collisions and inelastic collisions. Elastic collisions occur more

commonly, but since there is no energy exchange between the colliding molecules during elastic collisions, it is less crucial in this case. On the other hand, many types of inelastic collisions occur simultaneously in the plasma between electrons and ions, ions and ions, ions and neutral molecules, neutral molecules and electrons, etc.. It will then result in several kinds of chemical reactions, such as excitation (Equation 2.6), ionization (Equation 2.7), dissociation (Equation 2.8), electron attachment (Equation 2.9), dissociative attachment (Equation 2.10), photoemission (Equation 2.11), charge transfer (Equation 2.12).

$$A + e^- \rightarrow A^* + e^- \tag{2.6}$$

$$A + e^- \rightarrow A^+ + 2e^- \tag{2.7}$$

$$A_2 + e^- \rightarrow 2A + e^- \tag{2.8}$$

$$A + e^- \rightarrow A^- \tag{2.9}$$

$$A_z + e^- \rightarrow A + A^- \tag{2.10}$$

$$A^* \rightarrow A + hn \tag{2.11}$$

$$A^+ + B- \rightarrow A + B^+ \tag{2.12}$$

Where A, A_2 and B are reactants, e^- represent an negatively charged electron, A^* is reactant A in an excited state, and A^+, A^- and B^+ are ions of A and B [76].

Among the aforementioned reactions, ionization, excitation and dissociation contribute the most to the deposition. Firstly, in ionization, when an electron collides with an atom or molecule, it transfers part of its energy to the orbital electron by the nucleus or molecular nucleus. If the orbital electron gains enough energy to break away from the nucleus, it becomes a free electron. Secondly, sometimes the orbital electrons cannot get enough energy from the colliding electrons to escape from the bondage of the nucleus. However, if the collision can transfer enough energy to make the orbital electrons jump to a higher energy orbit, this process is called excitation. The excited state is unstable and short-lived. If the electrons in the excited state orbit cannot stay for too long, they will return to the lowest energy level or ground state. This process is called relaxation. When excited atoms or molecules quickly relax to the original state, they release the excess energy obtained from the collision of electrons in the form of photons, resulting in the unique glow discharge phenomenon of plasma. Thirdly, when electrons and molecules collide, if the energy transferred to the molecule via collisions is higher than the bonding energy of the molecule, it can break the chemical bond and generate free radicals. Free radicals are molecular fragments with at least one unpaired electron and therefore unstable. They are chemically reactive since they have a strong tendency to snatch electrons from other atoms or molecules to form stable molecules, which can promote chemical reactions in PECVD chambers. The free radicals produced by the decomposition and collision process in the plasma can effectively increase the chemical reaction rate and increase the deposition rate. [62]

For the propose of intrinsic a-Si:H deposition, SiH_4 and H_2 are utilized as precursor gases. The reaction process in the plasma formed by these two gases is extremely complex, involving hundreds of reaction equations [5][78][39]. Table 2.2 summarizes the reaction rate constant data mainly related to the SiH_4 plasma reaction.

Table 2.2: Reaction rate constant data related to the SiH_4 plasma reaction

Process	Rate constant (cm^3/s)
$e^- + SiH_4 \rightarrow SiH_3 + H + e^-$	1.59×10^{-10}
$e^- + SiH_4 \rightarrow SiH_2 + 2H + e^-$	1.87×10^{-11}
$e^- + SiH_4 \rightarrow SiH + H_2 + H + e^-$	9.34×10^{-12}
$e^- + SiH_4 \rightarrow SiH_3^+ + H + 2e^-$	5.64×10^{-12}
$e^- + SiH_4 \rightarrow SiH_2^+ + H_2 + 2e^-$	7.19×10^{-12}
$e^- + SiH_4 \rightarrow SiH^+ + H_2 + H + 2e^-$	1.39×10^{-12}
$SiH_4 + H \rightarrow SiH_3 + H_2$	2.68×10^{-12}
$SiH_3 + H \rightarrow SiH_2 + H_2$	1.00×10^{-10}
$SiH_2 + H \rightarrow SiH + H_2$	7.96×10^{-13}
$SiH + H_2 \rightarrow SiH_3$	1.98×10^{-12}
$SiH_3 + SiH_3 \rightarrow SiH_2 + SiH_4$	7.00×10^{-12}

From the SiH_4 reaction rate constants in Table 2.2, it can be inferred that the group that plays a leading role in the growth of a-Si:H film in the PECVD chamber is SiH_3 radicals, which is consistent with the experimental conclusion in the literature [27][34][63][48][81].

With the above introduction for PECVD instrument structure and the principle of precursor gas decomposition, it is better to understand the deposition procedure as 5 steps:

1. Driven by generated electric field or the concentration difference between the mainstream and the surface of the substrate, the reaction radicals drift or diffuse to the substrate surface.

2. Radicals reach the surface of the substrate, lose part of their kinetic energy, are attached to the surface, and then are deposited on the surface.

3. The reaction radicals obtain the energy provided by the wafer surface, thereby leading to chemical reactions. During this process, the reaction product will move on the wafer surface, and finally the deposition is completed.

4. When the deposition reaction occurs, the unreacted reactants and some products will obtain energy from the wafer surface, and detach from the wafer surface.

5. Finally, part of the products and unreacted radicals return to the main stream and are purged away by the pump.

In this project, the PECVD instrument for a-Si:H deposition is AMOR. For intrinsic layer growth, silane (SiH_4) and hydrogen (H_2) with a gas flow ratio of 4 sccm/35 sccm are utilized as precursor gases, and argon (Ar) is for purge. As for n^+ a-Si:H, the 3.5 sccm phosphine (PH_3) is added. Both two deposition is based on a chamber pressure of 1 mbar, substrate temperature of 180°C, and wafer preheat time of 40 min. The RF power in n-type capping a-Si:H is set at 5

W, while for contact intrinsic layer deposition, it becomes a variable. For each case, RF power has a different constant value, ranging from 5 W to 55 W, with an interval of 10 W. Since the electrode working area is about 12×12 cm^2, the power density ranges from 34.7 mW/cm^2 to 381 mW/cm^2.

High-temperature annealing

Two high-temperature annealing processes are involved in the flow chart, both performed with a TEMPRESS tube furnace. Firstly, a pre-annealing right after contact intrinsic a-Si:H deposition needs to be conducted, which is used to open the pinholes in tunnel oxide. Learning from the literature, the pinhole starts to be observed from a high temperature of 900°C [19], and its density can be counted more accurately at 1050°C [26]. Therefore, the pre-annealing is performed at a temperature of 1050°C for 1 min, with a N_2 atmosphere.

Additionally, a post-annealing is required after n^+ a-Si:H capping deposition by AMOR. The first aim is to crystallize silicon from an amorphous state to a polycrystalline state. Another function of it is to promote phosphorous atoms diffuse over the whole poly-Si region and active them. Considering the crystallinity and other properties required, the post-annealing will start a chamber heating from 600°C to 900 °C with a ramping-up rate of 10°C/min, then stay at 900°C for 30 min, and finalize the process with a cooling-down at the same ramping rate during heating. The schematic of the furnace is the same with dry oxidation as Figure 2.2.

2.1.2. Hydrogenation

The hydrogenation procedure includes two processes, SiN_x:H capping layer deposition and forming gas annealling. The SiN_x:H is deposted in Kavli nanolab by the instrument of Oxford Plasmalab System 100 PECVD. During deposition, ammonia (NH_3), silane (SiH_4) and hydrogen (H_2) act as precursor gases, the substrate temperature is 400°C, and the deposition rate is about 0.223 nm/s and the thickness is 75 nm.

After SiN_x:H fabrication, a forming gas annealing (FGA) process is conducted at Kavli nanolab with the horizontal furnace from TEMPRESS. The annealing is set up with 400°C and a duration of 30 min, with a forming gas of 10% H_2 in N_2.

Metal evaporation

Metallization in this project is finished by thermal evaporation, which is one of the methods in physical vapor deposition (PVD). The metal source Ag is placed in a tungsten boat, which has a higher melt point than metal Ag. By heated by a resistor under high voltage, metal Ag experiences gasification and is evaporated into the chamber in vacuum. At the meantime, the sample rotates with the substrate holder at a constant speed, and finally the silver is evenly attached to the surface of the sample to form a metal film. The schematic of metal evaporation equipment is shown in Figure 2.6.

2.1.3. Sample fabrication flowchart

In this project, there are mainly four types of sample are used, namely Si thin film characterization sample, FTIR sample, surface passivation sample, and contact resistivity sample. The preparation processes of each of them will be introduced as following.

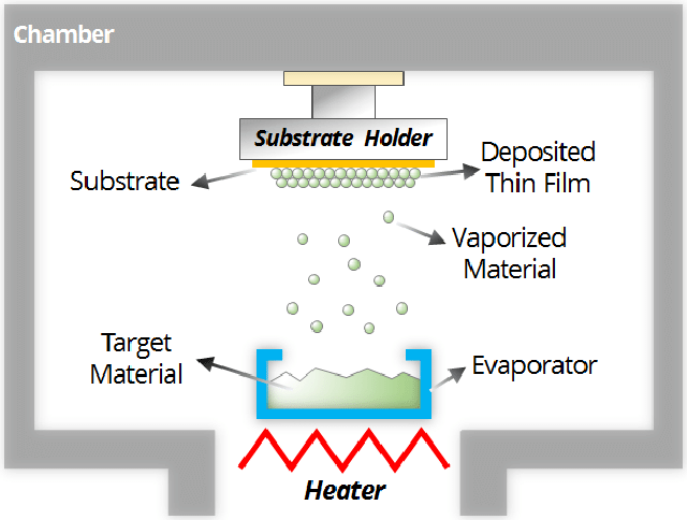

Figure 2.6: Schematic of metal evaporation equipment. [61]

Si thin film characterization sample

The flowchart of normal thin film sample preparation is shown in Figure 2.7a. These samples will be used to investigate the characteristic of different thin films. The details of each step will be introduced as following:

1. Wafers are used here are phosphorous doped, <100> FZ c-Si from TOPSIL, with a thickness of 280 μm.

2. A standard cleaning is performed for all samples. Firstly, 99% HNO_3 solution is used to remove the organic contaminants on the wafer surface for 10 minutes. After 5 minutes rinsing with DI water, wafers are immersed into the 69.5% HNO_3 solution for another 10 minutes to remove the inorganic particles, followed by a 5 minutes DI water rinsing. Then, 0.55% HF solution in Marangoni instrument is utilized to etch the native oxide grown during cleaning process. The etching duration maintains for 5 minutes. Wafers finally are rinsed by DI water for another 5 minutes and dried by IPA.

3. After that, the cleaned wafers are loaded on the boat of furnace's paddle for oxidation. An ultra-thin silicon oxide is grown on the wafer surface at 675°C for 3 min, with a gas mixture consisting N_2 and O_2.

4. Then the samples are divided into two groups with different contact Si thin film layer: PECVD samples and LPCVD reference samples. PECVD sample is one with a 20 nm thickness intrinsic a-Si:H layer deposited via PECVD method. For different cases in PECVD group, RF power is changed. Specifically, 5 W, 15 W, 25 W, 35 W, 45 W and 55 W are applied in different sample, respectively. And for comparison, the intrinsic poly-Si layer of sample in LPCVD group is prepared by LPCVD furnace. Each sample can be easily recognized since there is a mark labeled by diamond pen close to the edge.

5. After thin film deposition, the pre-annealing step is performed for all samples. At 1050°C

for 1 min, amounts of pinholes in t-SiO_x are formed.

It is worth noting that the samples for a-Si:H layer (SE and AFM measurement) only include the first 4 steps, while samples for SiO_x layer property (pinhole observation and XPS measurement) study will finalize all 5 steps.

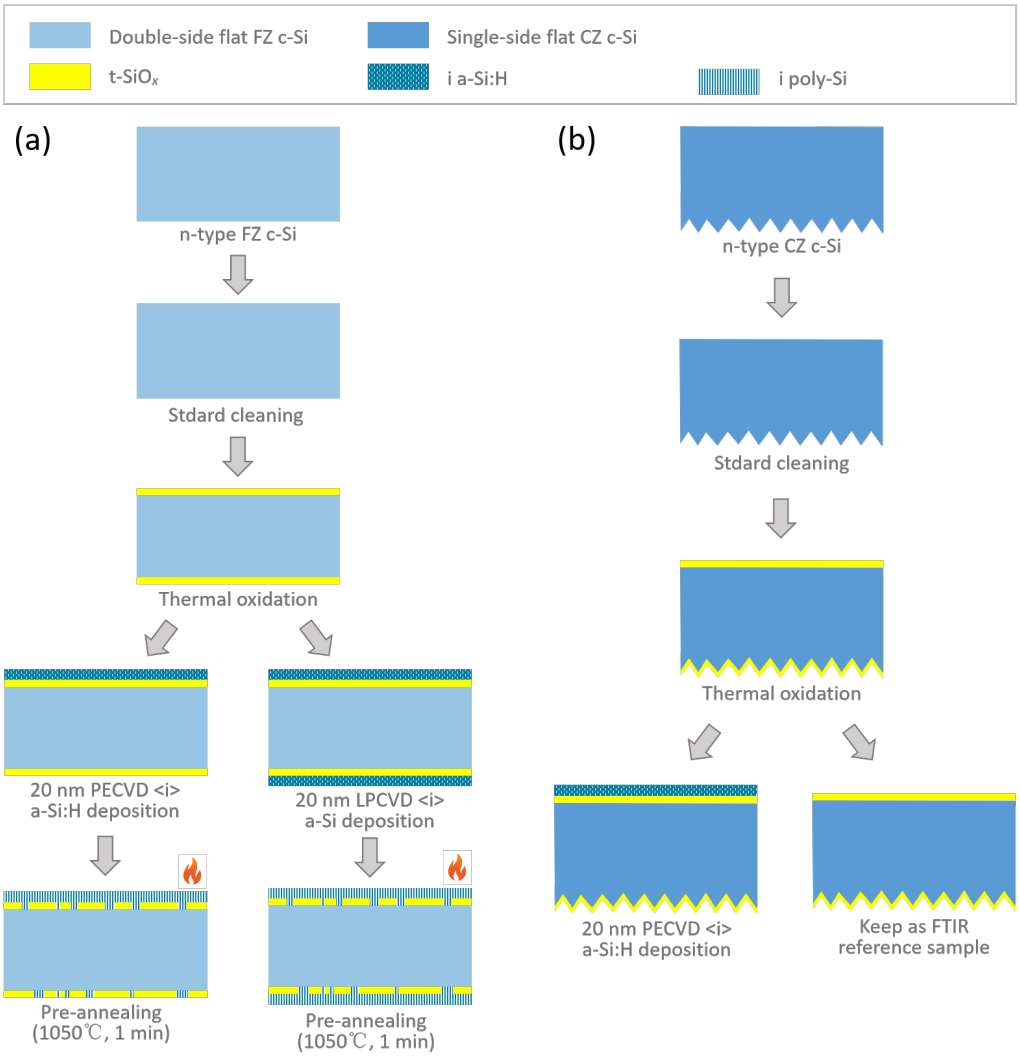

Figure 2.7: Flowchart for (a) TOPCon sample fabrication and (b) FTIR sample.

FTIR sample

As shown in Figure 2.7b, FTIR samples need to be listed separately because this measurement has special requirements for the wafer. For instant, those wafers are supposed to have a thick thickness and higher resistivity (> 5 Ω·cm). The process of FTIR sample fabrication is similar to that of thin film samples, while the differences are:

1. The wafer for FTIR is 525 µm thick, single-side polished, and has the resistivity of 10-20 Ω·cm.

2. After oxidation, each FTIR sample is cleaved into two halves by diamond pen. One half of them will keep its state as the reference sample in the subsequent FTIR measurement,

providing the ground spectra. And another half will proceed the intrinsic a-Si:H by PECVD.

3. Furthermore, there is no LPCVD sample needed for FTIR.

Passivation sample

Passivation samples are used to determine the crystallinity of poly-Si and evaluate the passivation quality of the passivating contact. The flowchart is shown in Figure 2.8, and experimental details are as following:

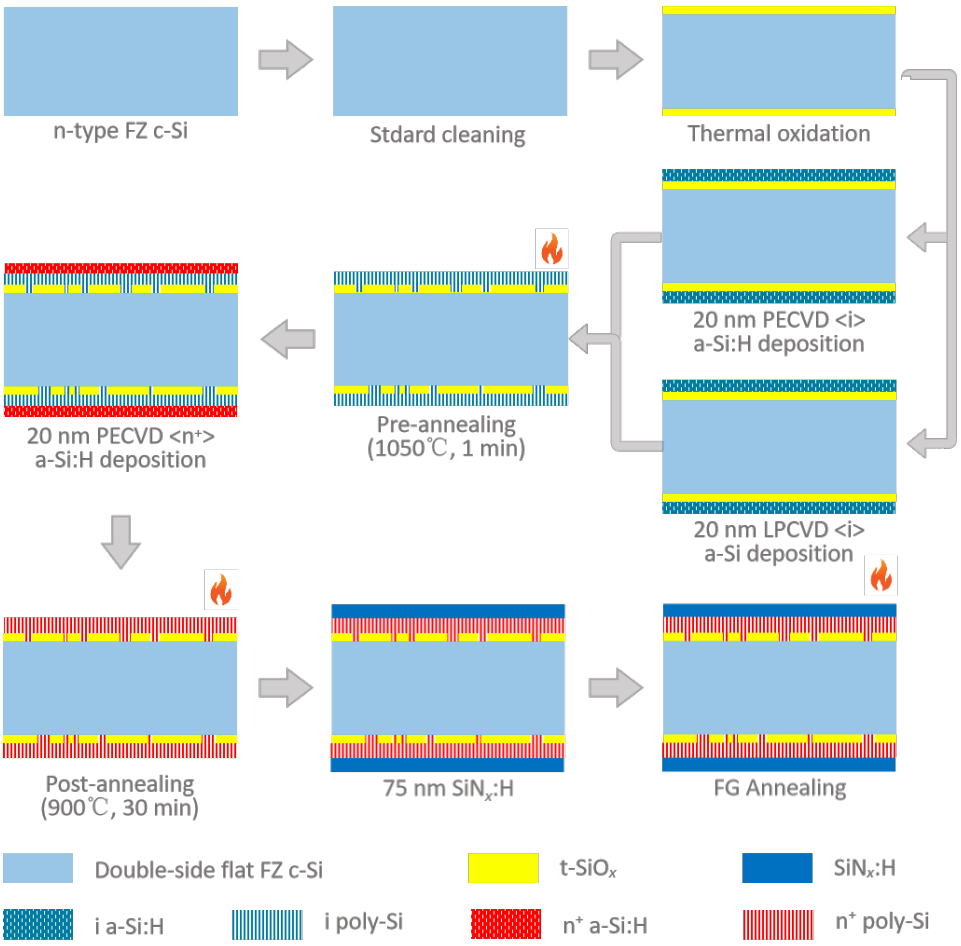

Figure 2.8: Flowchart for passivation sample fabrication.

Contact resistivity sample

The last kind of sample is prepared to measure the specific contact resistivity of passivating contact. The flowchart is shown in Figure 2.9. The contact sample formation is based on the passivation samples. Before electrodes formed on both sides, it is necessary to remove the SiN_x:H on the surface, since SiN_x:H is an insulator, which will block the conduction of the circuit during subsequent measurement. For this purpose, 0.55% HF or BHF (buffered hydrofluoric acid 1:7 is used for 5 minutes. BHF 1:7 is the mixture of 49% HF and 40% NH_4F, with a ratio of 1:7. Since the contact resistivity will be measured by Cox-Strack method, the

tested sample is cut into 2×2 cm^2 square pieces. Then, 500 nm metal Ag will be evaporated thermally and deposited on the surface of each sample.

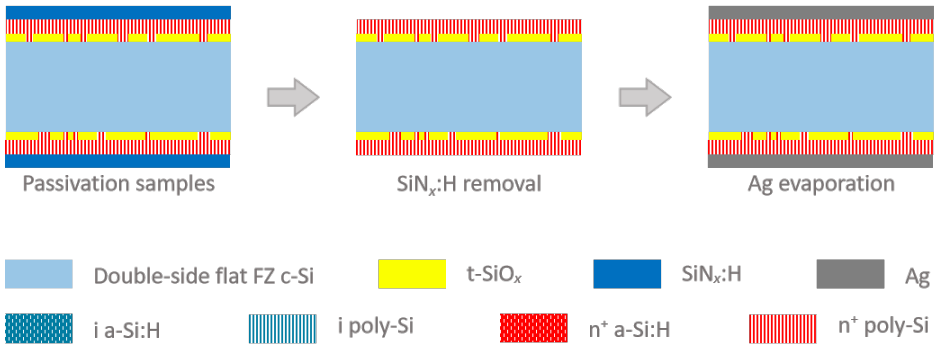

Figure 2.9: Flowchart for contact sample fabrication.

2.2. Characterization techniques

This section is to introduce several characterization techniques involved in this project. The thin film property is detected by SE, optical microscope, SEM, XPS, FTIR, Raman as well as stress meter. The second part is referring the techniques for passivation quality evaluation, dopants concentration distribution as well as the contact resistivity measurement.

2.2.1. Thin films

Optical microscope

An optical microscope (abbreviated as OM) is a kind of microscope, which uses optical principles to magnify and image tiny objects that cannot be distinguished by the naked eye, so that people can extract microstructure information.

The reason why the OM can magnify the object to be inspected is realized through the lens. Single-lens imaging has aberrations, which seriously affect the imaging quality. Therefore, the main optical components of the microscope are composed of more than one lens. It can be seen from the different lens performances that only a convex lens can magnify, while a concave lens cannot. Although the objective lens and eyepiece of the microscope are composed of lenses, they are equivalent to a convex lens. In order to facilitate the understanding of the magnification principle of the microscope, briefly explain the five imaging laws of the convex lens:

1. When the object is located beyond the double focal length of the object side of the lens, a reduced inverted real image will be formed within the double focal length of the image side and outside the focal point.

2. When the object is located on the double focal length of the object side of the lens, an inverted real image of the same size is formed on the double focal length of the image side.

3. When the object is within twice the focal length of the lens object side and outside the

focal point, a magnified inverted real image will be formed outside the double focal length of the image side.

4. When the object is located at the focal point of the lens object, the image cannot be imaged.

5. When the object is within the focal point of the lens object side, no image is formed on the image side, and a magnified upright virtual image is formed on the same side of the lens object side farther than the object.

The imaging principle of the microscope is to use the laws of (3) and (5) to magnify the object. When the object is between f-$2f$ in front of the objective lens (f is the focal length of the object side), a magnified inverted real image will be formed outside the double focal length of the objective mirror side. In the design of the microscope, this image falls within one focal length f of the eyepiece, so that the first image (intermediate image) magnified by the objective lens is magnified again by the eyepiece, and finally on the object side of the eyepiece (intermediate image) On the same side of the human eye), a magnified upright (compared to the intermediate image) virtual image is formed at the distance of human eyes (250 mm). Therefore, when we are in the OM inspection, the image of the original object seen through the eyepiece (without an additional conversion prism) is in the opposite direction.

Most optical microscopes have a similar structure component. As shown in Figure 2.10, the optical system of the microscope mainly includes four parts: objective lens, eyepiece, mirror and condenser. In a broad sense, it also includes illumination sources, filters, coverslips, and slides. The objective lens is the most important part that determines the performance of the microscope. It is installed on the objective lens converter and is close to the object to be observed.

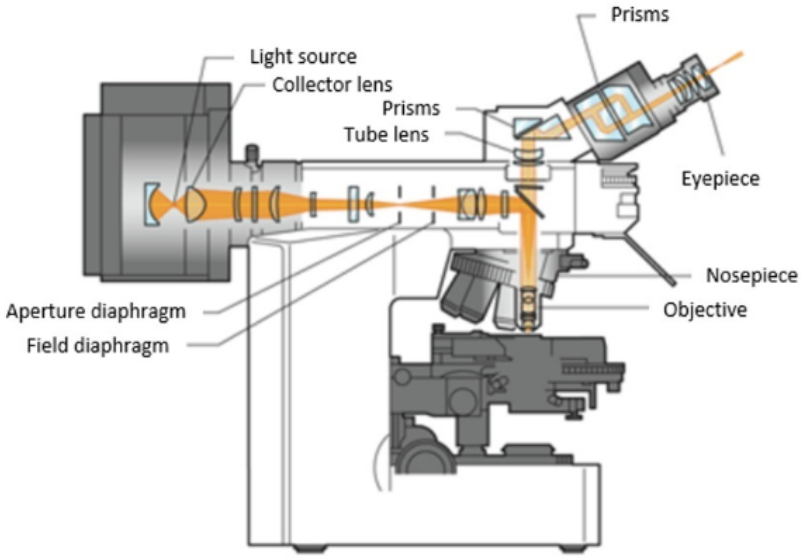

Figure 2.10: Schematic of classic optical microscope. [57]

And the eyepiece, because it is close to the observer's eye, is also called the eyepiece. It is installed on the upper end of the lens barrel. The shorter the length of the eyepiece, the greater the magnification, since the magnification of the eyepiece is inversely proportional to the focal length of the eyepiece. The function of the eyepiece is to further magnify the resolved real image that has been magnified by the objective lens, to the extent that the human eye can easily distinguish it.

The relationship between the eyepiece and the objective lens is: (i) If the fine structure resolved by the objective lens is not re-magnified by the eyepiece and does not reach the size that the human eye can distinguish, it will not be observed. (ii) For the fine structures that cannot be resolved by the objective lens, even after re-magnification by the high-power eyepiece, still cannot be recognized. In other words, the eyepiece can only be used for magnification, and will not improve the resolution of the microscope. Sometimes although the objective lens can distinguish two very close object points, it is still impossible to observe clearly because the distance between the images of these two object points is smaller than the resolution distance of the eyes. Therefore, the eyepiece and the objective lens are not only related to each other but also restrict each other.

The microscope used in this project is the reflected light microscope ZEISS Axiotron, where the images are obtained digitally. A magnification of 100 is selected for pinhole observation, which provides a sufficient range to inspect micron-scale features.

Scanning electron microscope

The scanning electron microscope (SEM) is a large-scale instrument for testing the surface morphology of samples. It is based on the interaction of electrons and substances.

In principle, the scanning electron microscope uses a pretty finely focused high-energy electron beam to scan the sample to stimulate various physical information. Observation of the surface topography of the test sample is obtained by accepting, amplifying, and displaying this information. The schematic of SEM is shown in Figure 2.11.

Under the acceleration voltage of 2-30 kV, through the electron optical system composed of 2 to 3 electromagnetic lenses, the electron beam is converged into an electron beam with a small aperture angle and a beam spot of 5-10 nm, then focuses on the surface of the sample. A scanning coil is installed on the final lens. With the help of it, the electron beam scans the surface of the sample. The high-energy electron beam interacts with the material on the surface of the sample to generate signals such as secondary electrons, back-reflected electrons, and X-rays.

These signals are respectively received by different receivers and amplified to modulate the brightness of the fluorescent screen. Since the current passing through the scanning coil is synchronized with the current on the corresponding deflection coil of the picture tube, the signal emitted by any point on the surface of the sample corresponds to the corresponding bright spot on the fluorescent screen of the picture tube.

That is to say when the electron beam hits a point on the sample, there will be a bright spot corresponding to it on the fluorescent screen, and its brightness is proportional to the energy of the excited electron. In other words, SEM is performed by point-by-point image decomposition. In addition, the order of light point imaging is from the upper left to the lower right,

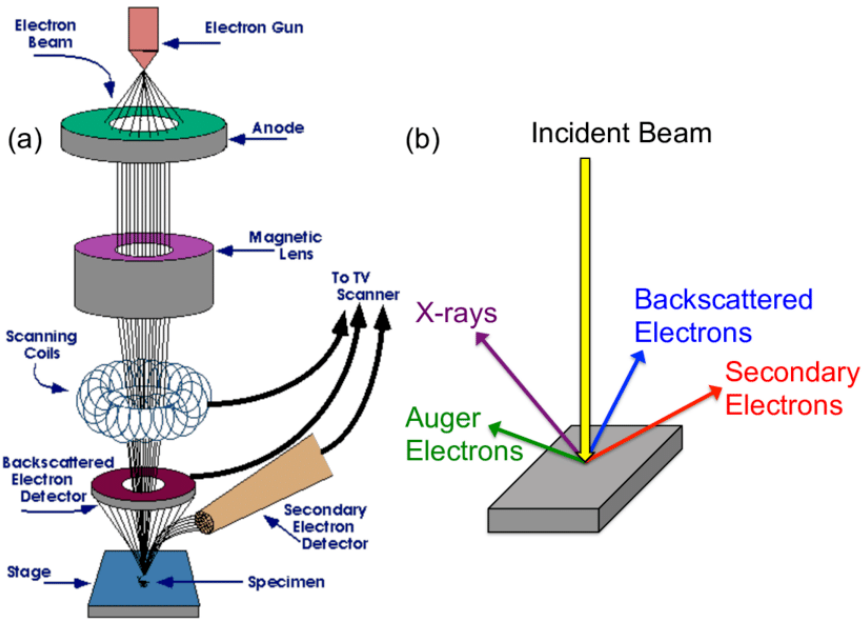

Figure 2.11: Schematic drawing of (a) the typical Scanning Electron Microscope (SEM) column, and (b) sample-beam interactions within a SEM. [90]

until the last row of pixels at the lower right is scanned to complete a frame of image. This scanning method is called raster scanning.

Additionally, SEM consists of an electron optical system, signal collection and display system, vacuum system and power supply system. Firstly, the vacuum system mainly includes two parts: a vacuum pump and a vacuum column. A vacuum column is a sealed cylindrical container, and the vacuum pump is used to create a vacuum in the vacuum column. Generally, both the imaging system and the electron beam system are built into the vacuum column. The bottom of the vacuum column is the sealed chamber, which is used to place the sample. The reason for using a vacuum is mainly based on the following two reasons: (i) The filament in the electron beam system will quickly oxidize and fail in the ordinary atmosphere, so in addition to using a vacuum when using the SEM, it is usually necessary to fill the entire vacuum column with pure nitrogen or inert gas. (ii) The second reason is to increase the mean free path of electrons, allowing more electrons collected for imaging.

Secondly, the electron optical system consists of an electron gun, electromagnetic lens, scanning coil and sample chamber and other components. It is used to obtain a scanning electron beam as an excitation source for generating physical signals. In order to obtain higher signal intensity and image resolution, the scanning electron beam should have higher brightness and as small a beam spot diameter as possible. Among different components, the electron gun plays the most important role. It utilizes the high voltage between the cathode and the anode filament to generate a high-energy electron beam. Besides, electromagnetic lens are used to gradually shrink the beam spot of the electron gun. For instance, the original beam spot with a diameter of about 50 mm can be reduced to a small beam spot with only a few nanometers. Moreover, the function of scan coil is to provide an incident electron beam on the sample surface. By changing the scanning amplitude of the incident electron beam, the scanned image will be magnified. Finally, the main component in the sample chamber is the sample stage. It

can move in three-dimensional space, tilt, and turn.

Thirdly, SEM signal detection amplification system detects the physical signal generated by the sample under the action of incident electrons, and then amplifies by video as the modulation signal of the imaging system. Different physical signals require different types of detection systems, which can be roughly divided into three categories: electron detectors, cathodoluminescent detectors, and X-ray detectors. Electron detectors and X-ray detectors are involved in NOVA NANOSEM system.

Finally, since the electron beam in the lens barrel and the electron beam in the picture tube are scanned synchronously, the brightness on the fluorescent screen is modulated according to the intensity of the signal excited from the sample. However, the received signal intensity always changes with the surface conditions of the sample. The signal detection and amplification system then needs to adjust these signals and output an enlarged scanning image consistent with the surface characteristics of the sample.

The utilized instruction in this thesis is the NOVA NANOSEM. Thin film thickness and surface morphology can be inspected clearly and accurately. The picture of the utilized SEM is shown in Figure 2.12.

Figure 2.12: Image of NOVA NANOSEM 650 SEM system. [17]

Spectroscopic ellipsometry

Spectroscopic ellipsometry (SE) is an optical measurement device for probing film thickness, optical constants and microstructure of materials. The lack of contact with the sample, the absence of damage to the sample and the absence of a vacuum make the ellipsometer an attractive measurement device. Ellipsometry involves the reflection of elliptically polarized light from the surface of a material. In order to characterize the properties of reflected light, two components are defined: P and S polarization states. The P component refers to the linearly

polarized light parallel to the incident plane, and the S component refers to the linearly polarized light perpendicular to the incident plane, as shown in Figure 2.13.

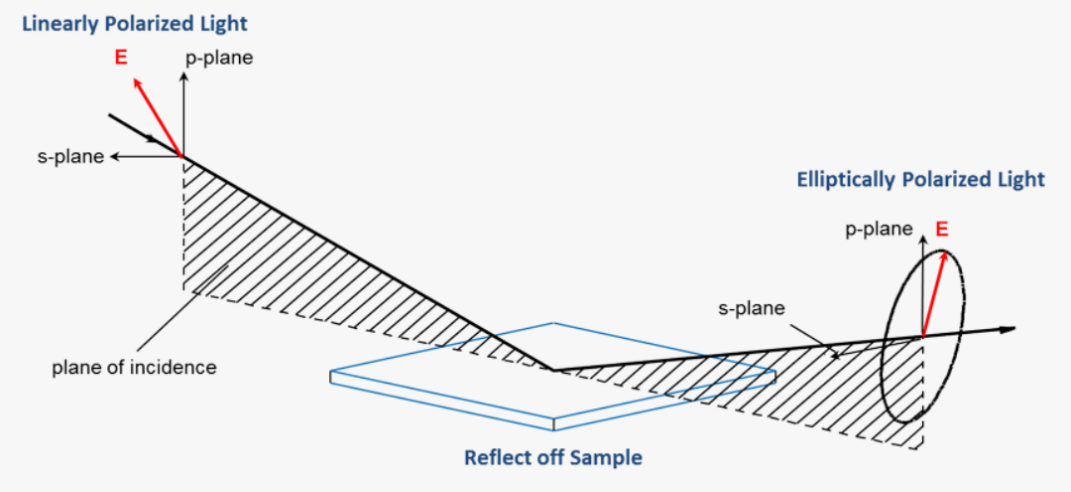

Figure 2.13: The incident light beam contains electric fields both parallel (p-) and perpendicular (s-) to the plane of incidence. [94]

The Fresnel reflection coefficient r describes the reflection of incident light at an interface. The respective Fresnel reflection coefficients r of the P and S polarization state components are the ratios of the respective reflected wave amplitudes to the incident wave amplitudes.

Since the sample generally has multiple interfaces, and the light returning to the original incident medium undergoes multiple reflections and transmissions. The total reflection coefficients, R_p and R_s, are determined by the Fresnel reflection coefficients of each interface. R_p and R_s are defined as the ratio of the final reflected wave amplitude to the incident wave amplitude.

Figure 2.13 shows the basic optical and physical structure of the ellipsometer. The polarization state of the incident light is known, the polarized light is reflected on the surface of the sample, and then the polarization state (amplitude and phase) of the reflected light is measured to calculate or fit the properties of the material.

SE shows excellent performance on thin film characterization, such as high precision of very thin films (1 nm), non-destruction during the measurement, and high sensitivity to some surface structures. In this thesis, measuring the thickness of SiO_x is the main purpose of this instrument. The product image is shown in Figure 2.14.

Fourier transform infrared spectroscopy

Fourier transform infrared spectrometer (abbreviated as FTIR Spectrometer) is an infrared spectrometer developed based on the principle of Fourier transform of the interfered infrared light. Spectral analysis is a method to identify a substance and determine its chemical composition, structure or relative content based on its spectrum. According to the principle of analysis, spectroscopic techniques can be divided into three types: absorption spectroscopy, emission spectroscopy and scattering spectroscopy. If according to the shape of the measured position, it mainly includes atomic spectroscopy and molecular spectroscopy. And infrared spectroscopy

Figure 2.14: Image of M-2000F spectroscopic ellipsometer. [94]

belongs to the latter, molecular spectroscopy. In this case, infrared absorption spectroscopy is adopted.

The basic principle of infrared absorption spectroscopy is related to molecular motion. There are four kinds of molecular motions: translation, rotation, vibration and electronic motion, among which the last three are quantum motions. As shown in Figure 2.15, the molecule absorbs a photon with energy $h\nu$ from the lower energy level E_1, and can jump to the higher energy level E_2. The whole movement process satisfies the law of energy conservation E_2-E_1 = $h\nu$. The smaller the difference between the energy levels, the lower the frequency and the longer the wavelength of the light absorbed by the molecule.

The infrared absorption spectrum is caused by molecular vibration and rotational transition. The atoms that make up chemical bonds or functional groups are in a state of constant vibration (or rotation), and their vibration frequency is equivalent to that of infrared light. Therefore, when a molecule is irradiated with infrared light, the chemical bond or functional group in the molecule can undergo vibrational absorption. Different chemical bonds or functional groups have different absorption frequencies, and will be in different positions on the infrared spectrum, so that information about which chemical bonds or functional groups are indicated in the molecule can be obtained.

Actually, infrared spectroscopy is essentially an analytical method for determining the molecular structure of a substance and identifying compounds based on information such as the relative vibration between atoms in the molecule and molecular rotation. Since the molecular rotational energy level difference is relatively small and the absorbed light frequency is relatively low, corresponding to a long wavelength, the pure rotational energy spectrum of the

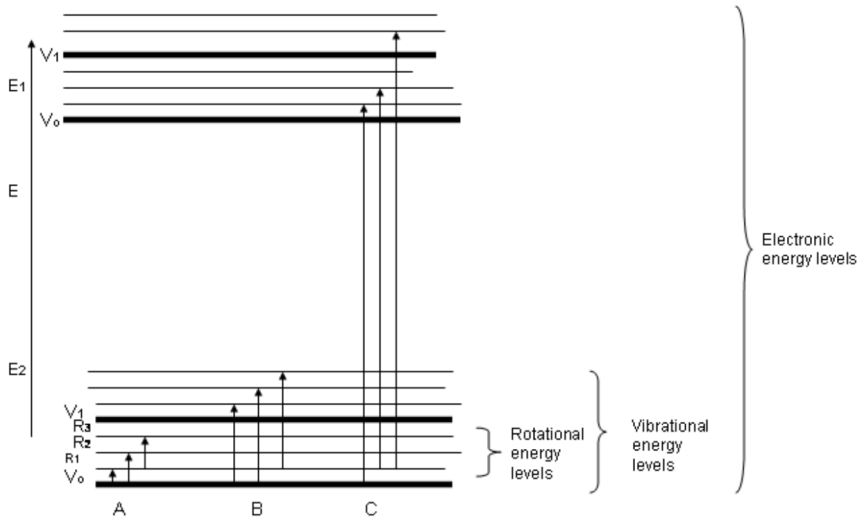

Figure 2.15: Energy levels for a molecule. Possible transitions that occur: (A): Pure rotational transitions, (B) rotational-vibrational transitions, (C) rotational-vibrational-electronic transitions. [59]

molecule then appears in the far-infrared region (25-300 μm). On the other hand, due to the large energy level difference of vibration, and the light frequency absorbed by the molecular vibrational energy level transition is thus higher. Therefore, the pure vibrational energy spectrum of molecules generally would appear in the mid-infrared region (2.5-25 μm). [98]

In addition, the molecular absorption would be influenced by instantaneous dipole moment, bond force and atomic weight. It is reported that the stronger the bond force, the higher the absorption frequency, as well as the smaller the atomic weight, the higher the absorption frequency.

However, the position of the absorption peak has the potential to be changed by plenty of factors: the factors from external such as the method of sample preparation, crystallization conditions, the thickness of the sample, and the intrinsic factor mainly related the molecular structure

The FTIR instrument consists of the infrared light source, interferometer and detector, as illustrated in Figure 2.16. And the measurement setup is shown in Table 2.3.

Table 2.3: FTIR measurement set-up

Number of scans	200	Source	IR
Final format	Transmittance%	Range	4000-400
Resolution	4	Velocity	0.639
Beamsplit	kBr	Aperture	92

X-ray photoelectron spectroscopy

X-ray Photoelectron Spectroscopy (XPS) is a method of measuring the energy distribution of photoelectrons and Auger electrons emitted from the surface of a sample when X-ray photons

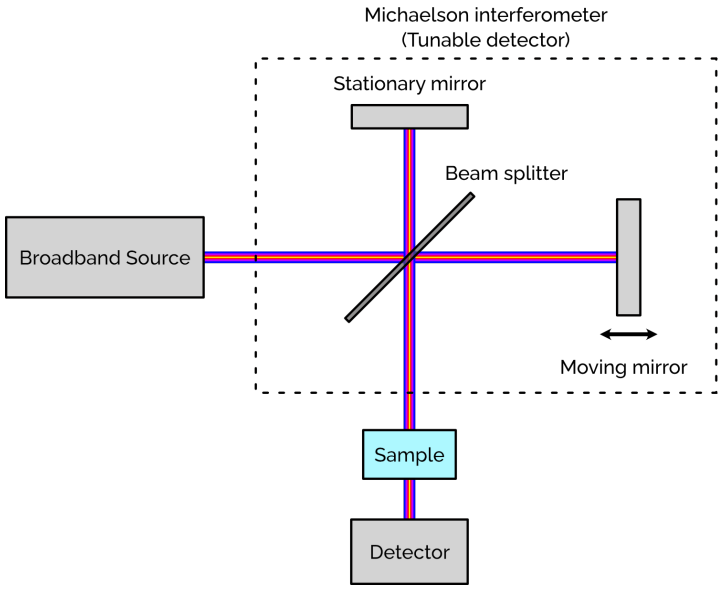

Figure 2.16: Schematic of FTIR measurement. [89]

are irradiated by an electron spectrometer. It can be used for qualitative analysis and semi-quantitative analysis. Generally, the information on the element composition, chemical state and molecular structure of the sample surface can be obtained from the peak position and peak shape of the XPS spectrum, and the content or concentration of the element on the surface of the sample can be obtained from the peak intensity.

The principle of XPS is on the basis of photoionization. When a beam of photons irradiates the surface of the sample, the photons can be absorbed by the electrons on the atomic orbitals of a certain element in the sample. The obtained energy releases electrons from the constraints of the atomic nucleus, which are emitted from the interior of the atom with a certain kinetic energy. Then atom itself becomes an ion in an excited state.

According to Einstein's law of photoemission:

$$E_k = h\nu - E_B \tag{2.13}$$

where E_k is the kinetic energy of the emitted photoelectron, $h\nu$ is the energy of the X-ray source photon, E_B is the binding energy on a specific atomic orbital (different atomic orbitals have different binding energies).

It can be seen from the Equation 2.13 that for a specific monochromatic excitation source and a specific atomic orbital, the energy of the photoelectron is characteristic. It means that when the energy of the excitation source is fixed, the energy of its photoelectrons is only related to the type of element and the excited atomic orbital. Therefore, we can qualitatively analyze the elemental types of substances according to the binding energy of photoelectrons.

Al $K\alpha$ and Mg $K\alpha$ X-rays are commonly used as the excitation source, which can detect all elements in the periodic table except hydrogen and helium. The general detection limit is 0.1% (atomic percentage). In this project, the XPS instrument from MSE lab is used to detect measure and semi-quantitively analyze the stoichiometric Si^{4+} in the tunnel silicon oxide, with

an excitation source of Mg $K\alpha$ and binding energy resolution of 0.2 eV. The schematic is shown in Figure 2.17.

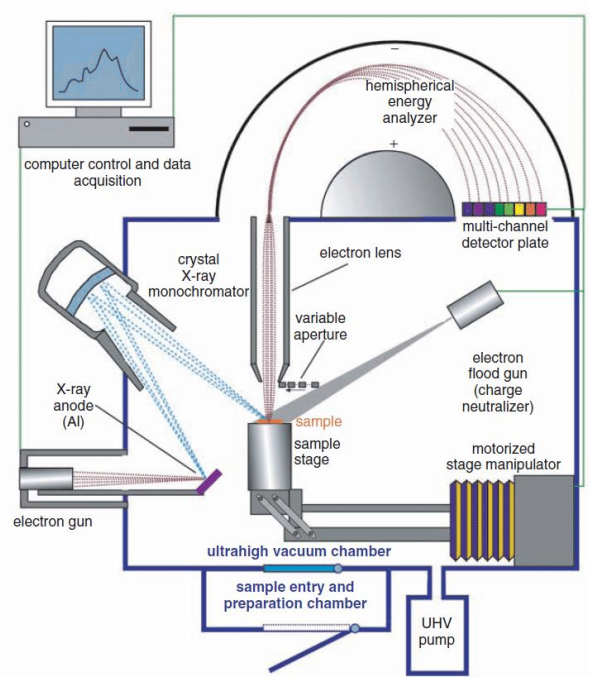

Figure 2.17: Schematic of XPS measurement. [82]

Raman measurement

Based on the Raman scattering effect discovered by Indian scientist C.V. Raman, Raman spectroscopy analyses the scattering spectrum different from the frequency of the incident light to obtain information on molecular vibration and rotation, and is applied to molecular structure research.

When a beam of monochromatic light of frequency ν_0 is irradiated on the sample, the molecules can scatter the incident light. Most of the light just changes the direction of light propagation. The frequency of the transmitted light passing through the molecule is still the same as that of the incident light. Such a kind of scattering is called Rayleigh scattering. On the other hand, if the transmitted light changes not only its direction of propagation but also the frequency, the Raman scattering occurs, as shown in Figure 2.18.

In Raman scattering, the frequency of scattered light is reduced relative to the frequency of incident light, which is called Stokes scattering. In contrast, if the frequency increases, it is called anti-Stokes scattering. Normally, Stokes scattering is much stronger than anti-Stokes scattering. Thus what Raman spectrometers usually measures is Stokes scattering, also collectively referred to as Raman scattering. [99]

A Raman spectrometer generally consists of five parts: a light source, an external light path, a dispersion system, and an information processing and display system. The Raman system from Renishaw at Kavli nanolab is used to determine the crystallinity of poly-Si. The schematic of the Raman structure is shown in Figure 2.19.

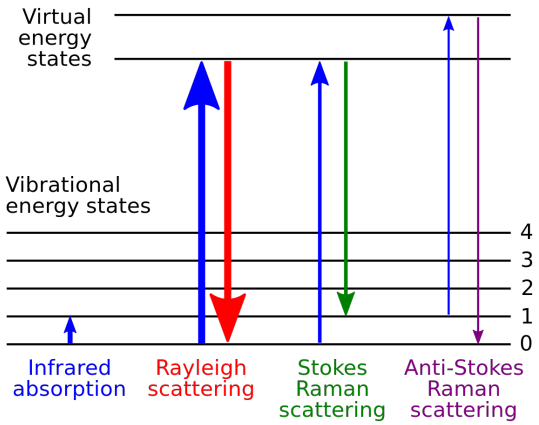

Figure 2.18: Different scattering with energy states. [99]

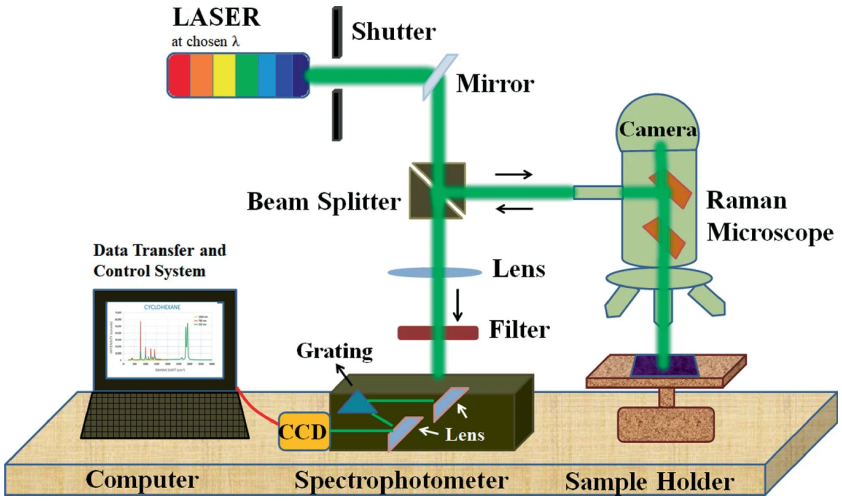

Figure 2.19: Schematic of Raman spectrometer. [60]

2.2.2. Passivating contacts

Electrochemical capacitance-voltage profiling

Electrochemical corrosion of semiconductors is realized based on the principle of anodic oxidation and point solution in electrochemistry. There are two methods to dissolve solid substances in liquids: (i) one is wet corrosion, that is, the chemical reaction between solids and liquids is used to gradually corrode solids without an external electric field. (ii) the other is electrochemical corrosion, that is, the solid is placed in the electrolyte, and a DC voltage is applied. The positive electrode of the voltage is connected to the solid substance that needs to be corroded, and the negative electrode of the voltage is connected to an electrode that is not dissolved and has good conductivity. After electrification, the anode material is gradually oxidized and corroded under the action of electric field and electrolyte.

Electrochemical differential capacitance-voltage, referred to as ECV, uses the electrolyte to form a potential barrier, and applies a forward bias (p-type) or reverse bias (n-type and illumination) to the semiconductor to corrode the surface to remove the electrolyzed Material. The measurement curve is obtained by repeating the ”corrosion-measurement” cycle through the

automatic device, and then the corrosion depth can be continuously obtained by integrating the corrosion current by applying Faraday's law. Although this method is destructive, it can theoretically measure infinite depth.

The ECV measurement contains two steps. The first is to measure the differential capacitance of the Schottky barrier formed at the electrolyte/semiconductor interface to obtain the carrier concentration, and then use the anode electrochemical dissolution reaction to remove the measured sample at a set rate. Equation 2.14 provides a simple method for determining the carrier density. By using an adjustable high-frequency voltage to change the parameters C and dC/dV, and repeating the "corrosion-measurement" cycle continuously, the carrier concentration and In-depth relationship, so as to achieve the purpose of testing.

The charge density of the carriers is:

$$N = \frac{1}{e\epsilon_0\epsilon_r A^2} \times \frac{C^3}{dC/dV} \tag{2.14}$$

Where ϵ_0 is vacuum permittivity, ϵ_r is the relative permittivity of semiconductor material, e is the electron charge, A is the area where the electrolyte contacts the semiconductor, dC/dV is the slope of the C-V curve at the edge of the depletion region.

The total depth corresponding to this carrier concentration is:

$$x = W_d \times W_r \tag{2.15}$$

where W_d is the depth of depletion region and W_r is the depth of corrosion.

In this project, ECV measurement is used to determine the dopant concentration distribution in n^+ poly-Si, which is performed by TNO. The schematic of ECV measurement is shown in Figure 2.21.

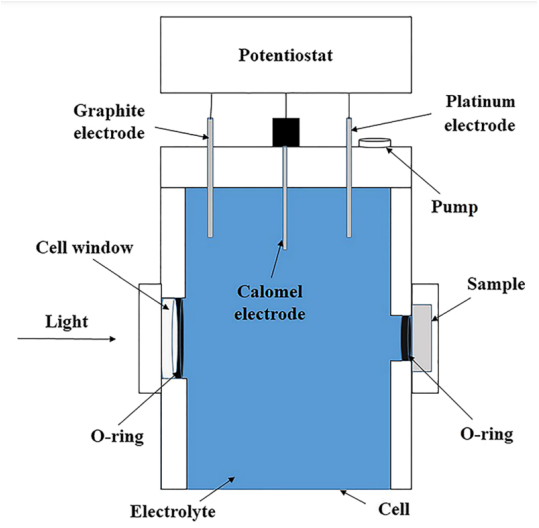

Figure 2.20: Schematic of ECV measurement. [71]

Current-voltage measurement

Wacom WXS-90S-L2 solar simulator in ESP lab can evaluate the electrical performance of the solar cell, by measuring the solar cell J-V curve. Within the measurement, external parameters, such as open-circuit voltage (V_{oc}), short-circuit current density (J_{sc}), fill factor (FF), the maximum power point voltage (V_{mpp}), the maximum power point current density (J_{mpp}), the series resistance (R_s), the parallel resistance (R_{sh}), as well as the efficiency (η) can be obtained. However, in this thesis, the only result is required, that is total resistance of the sample measured by 2-point probe at the standard test condition (STC). The resistance will be used to calculate the contact resistivity of the passivating contact. Figure 2.22 demonstrates the schematic of Wacom current-voltage measurement.

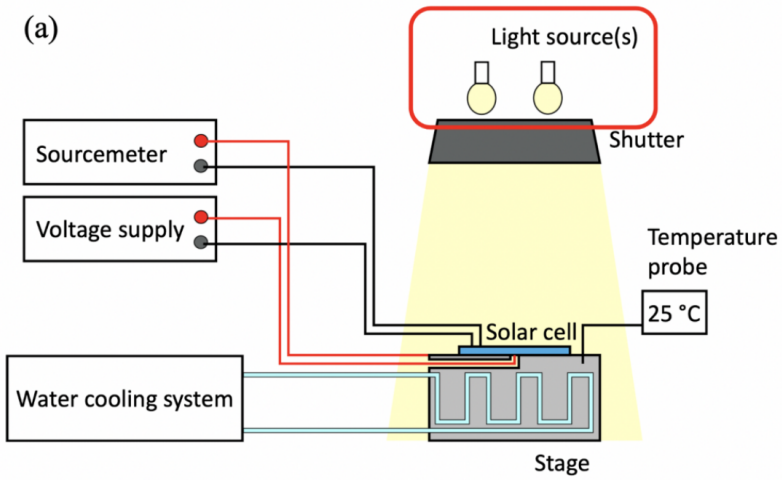

Figure 2.21: Schematic of Wacom current-voltage measurement.

3

Impact of PECVD a-Si:H contacting layer deposition on intrinsic a-Si:H and SiO_x thin films

This chapter aims to investigate the impact of PECVD a-Si:H deposition on the properties of a-Si:H contacting layer itself as well as the underlying ultra-thin SiO_x. After an introduction of experimental methods in section 3.1, a-Si:H and SiO_x properties will be analysed in section 3.2 and 3.3, respectively, with a changing PECVD RF power. And in the following section 3.4, the principle of pinhole formation in ultra-thin SiO_x will be discussed.

3.1. Experimental objective and method

Several measurements are performed to analyze the changed properties of thermal SiO_x and a-Si:H thin films. Different sample are fabricated to investigate a-Si:H deposition rate and surface density, pinhole density in SiO_x and its Si^{4+} stoichiometry. The flowchart of samples fabrication will be introduced in this section.

PECVD a-Si:H deposition rate measurement

In order to calculate the PECVD a-Si:H thin film deposition rate, each sample needed to be prepared with a stack of c-Si/t-SiO_x/i a-Si:H. During intrinsic a-Si:H deposition, a set of optimal tune and load positions in the generator was optimized under different RF power to minimize the reflected power. Then more than 8 samples were prepared for each RF power case by changing the deposition time. Finally, the thickness of a-Si:H on the labeled side was fitted by ellipsometry. The flowchart is shown as Figure 3.1.

a-Si:H surface density measurement and evaluation

Since infrared light is mainly applied on FTIR measurement, thicker silicon wafers with a thickness of around 525 µm are used. Secondly, in order to reduce the interference of impurities and obtain pure peaks, high resistivity is also required. The flowchart of FTIR measurement is

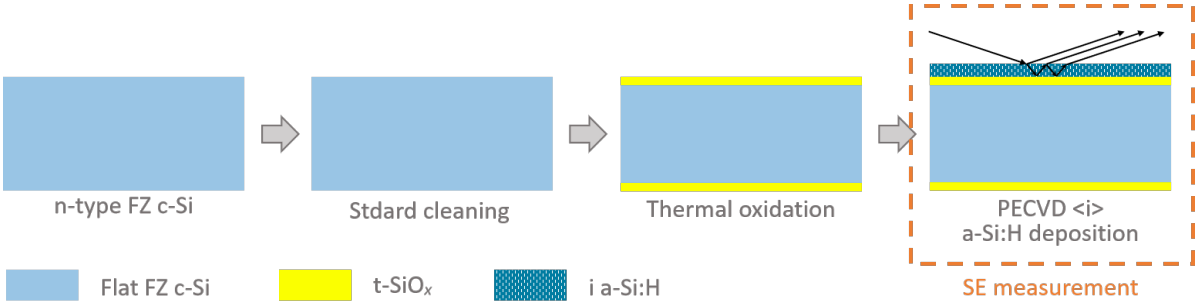

Figure 3.1: Flowchart of PECVD a-Si:H deposition rate measurement.

shown as Figure 3.2. Once the sample is oxidized thermally, it will be cleaved into two halves. One proceeds the a-Si:H deposition, and the other one stops the fabrication and is kept as a reference sample during measurement providing spectrum background information.

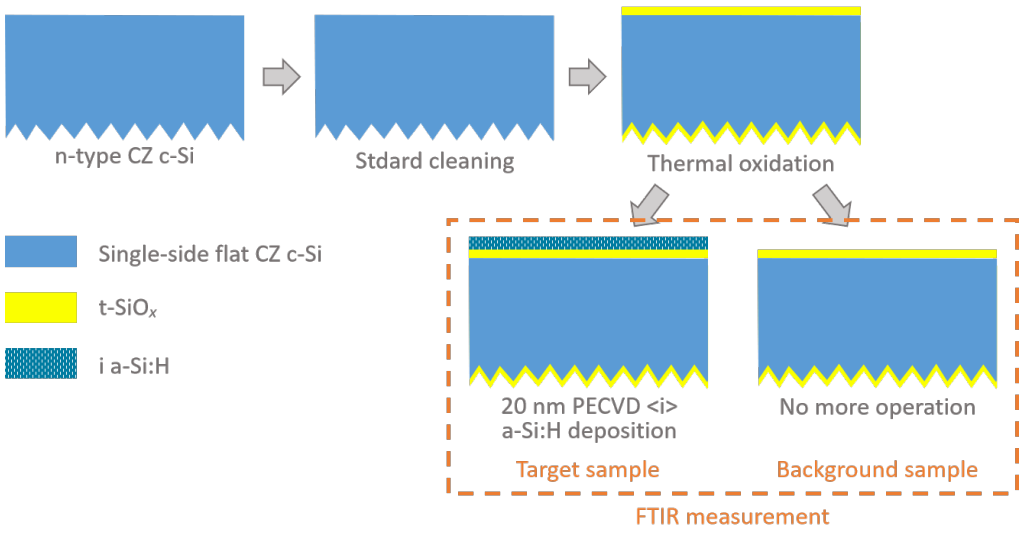

Figure 3.2: Flowchart of a-Si:H surface density measurement and evaluation.

Pinhole density in SiO_x observation and calculation

Pinholes are supposed to exist in SiO_x thin films by a large amount of studies. However, due to its limited density and small size, it is hardly to be observed in SEM or TEM directly. In this project, a semi-quantification method with the concepts of "selective etching" and "pinhole magnification" is applied to help calculate and compare the pinhole density changes in different cases.

In order to look for pinholes in tunnel oxide, poly-Si on the oxide need to be etched away. TMAH and KOH solution are two candidates for it, since both of them have a higher etch rate to <100>Si than that to SiO_2, namely higher etch selectivity of <100>Si:SiO_2. Comparing the etch selectivity of two solutions in Figure 3.3, the highest etch selectivity is found with 5% TMAH at the temperature of 70°C, with a value of 9600.

Ideally, when immersing the c-Si sample prepared with a poly-Si/SiO_x stack on the top into the 5% TMAH solution (70°C), the poly-Si will be quickly etched, and the chemical reaction

will "stop" at SiO_x layer. If there are pinholes appearing in SiO_x, the TMAH solution will pass through the pinholes and continue reacting with the underlying c-Si. With an appropriate etch duration, pinholes are rapidly magnified in the shape of an inverted pyramid (shown in Figure 3.4), and can be observed via SEM or even an optical microscope. Figure 3.5 shows the SEM images of pinholes in different sizes observed at different magnifications.

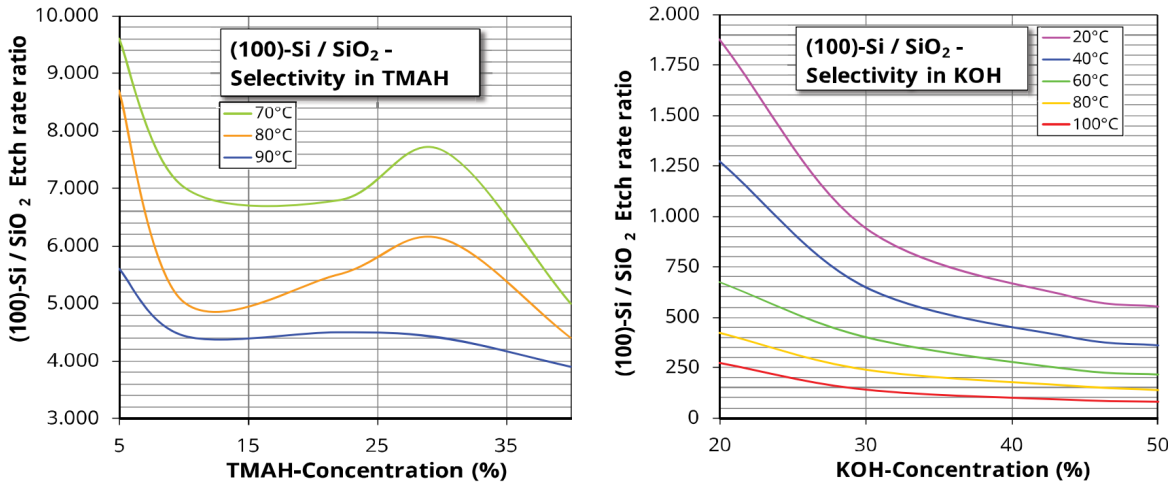

Figure 3.3: The concentration and temperature-dependent selectivity of the etching rate of <100>Si and SiO_2 in TMAH (left graph) and KOH (right graph). In TMAH, the etch rates of Si and SiO_2 have their maximum at different TMAH concentrations, which is why their ratio shows a local minimum.[51]

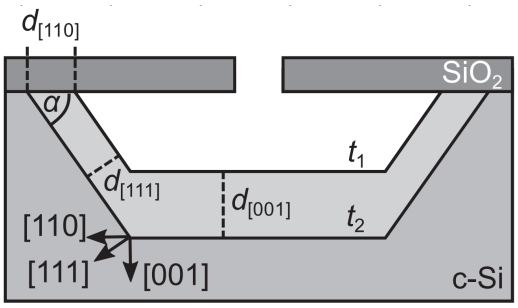

Figure 3.4: Schematic of enlarged pinholes.[86]

The experiment for pinhole density in SiO_x observation is divided into three processes: verification for etch selectivity of a-Si:H/SiO_x and poly-Si/SiO_x in TMAH solution, optimal etch time determination, pinhole density observation changed with RF power.

First of all, to calculate the etch selectivity of a-Si:H/SiO_x and poly-Si/SiO_x in 5% TMAH solution at 70°C, the etch rate of involved three thin films a-Si:H, poly-Si and SiO_x needed to be measured. Figure 3.6 shows the sample preparation process which is used to calculate the etch rate of SiO_x. Two steps of SE detection and simulation occur after thermal oxidation and TMAH etch for 60 seconds, respectively. The thickness of SiO_x is deduced from $d_{SiO_x,1}$ to $d_{SiO_x,2}$. Then the etch rate of SiO_x, ER_{SiO_x}, is calculated as

The charge density of the carriers is:

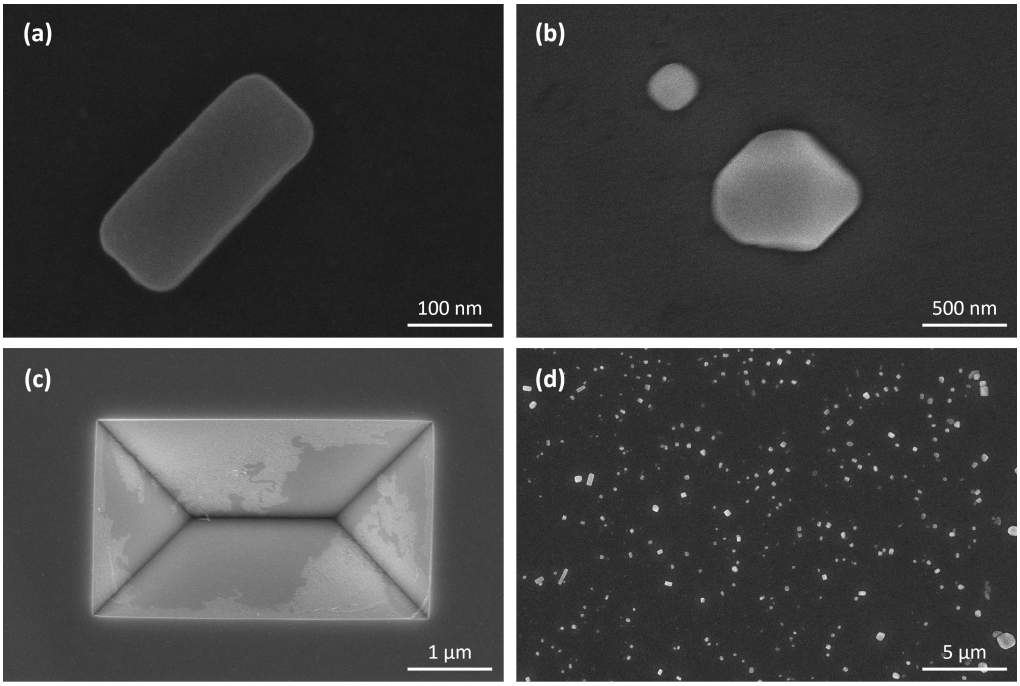

Figure 3.5: SEM images of pinholes in different sizes observed at different magnifications.

$$ER_{SiO_x} = \frac{d_{SiO_x,1} - d_{SiO_x,2}}{60\ s} \tag{3.1}$$

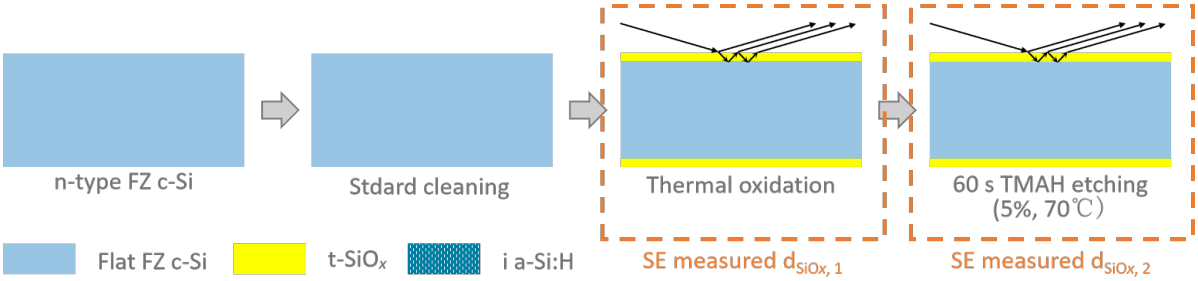

Figure 3.6: Flowchart of the experiment on the etch rate of SiO_x.

Figure 3.7 shows the process of the etch rate of a-Si:H calculation. The thickness of a-Si:H after PECVD deposition is observed by SEM, determined as $d_{a-Si:H,1}$. And after dipping in 0.55% HF for 3 minutes to remove native oxide and 20 seconds of TMAH etching, the second thickness of a-Si:H, $d_{a-Si:H,2}$, is measured by SE. Then the etch rate of a-Si:H, $ER_{a-Si:H}$, is calculated as

$$ER_{a-Si:H} = \frac{d_{a-Si:H,1} - d_{a-Si:H,2}}{20\ s} \tag{3.2}$$

Figure 3.8 shows the process of etch rate of poly-Si calculation. The thickness of poly-Si after 1050°C annealing for 1 minute [26] is observed by SEM, determined as $d_{poly-Si,1}$. After dipping in 0.55% HF for 3 minutes to remove native oxide and 20 seconds TMAH etching,

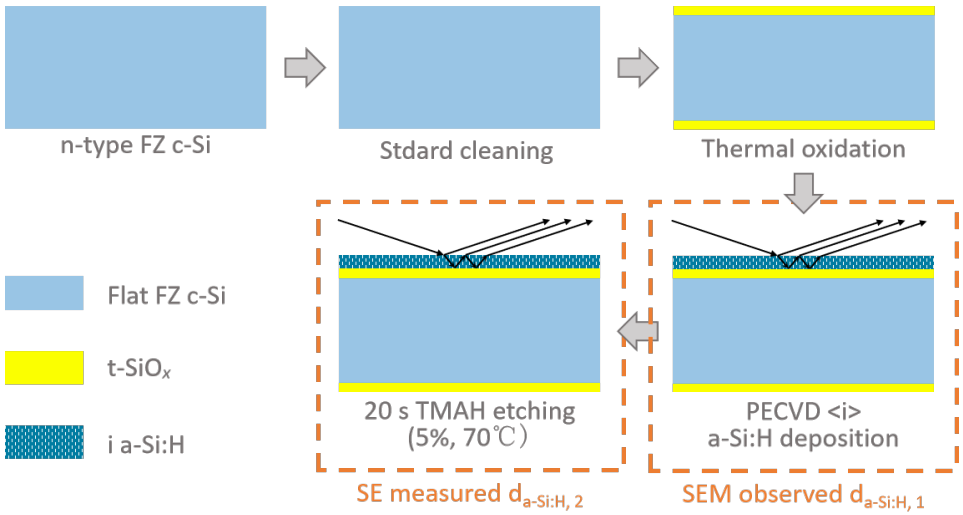

Figure 3.7: Flowchart of the experiment on the etch rate of a-Si:H.

the second thickness $d_{poly-Si,2}$ is measured by SE. Then the etch rate of poly-Si, $ER_{poly-Si}$, is calculated as

$$ER_{poly-Si} = \frac{d_{poly-Si,1} - d_{poly-Si,2}}{20\ s} \tag{3.3}$$

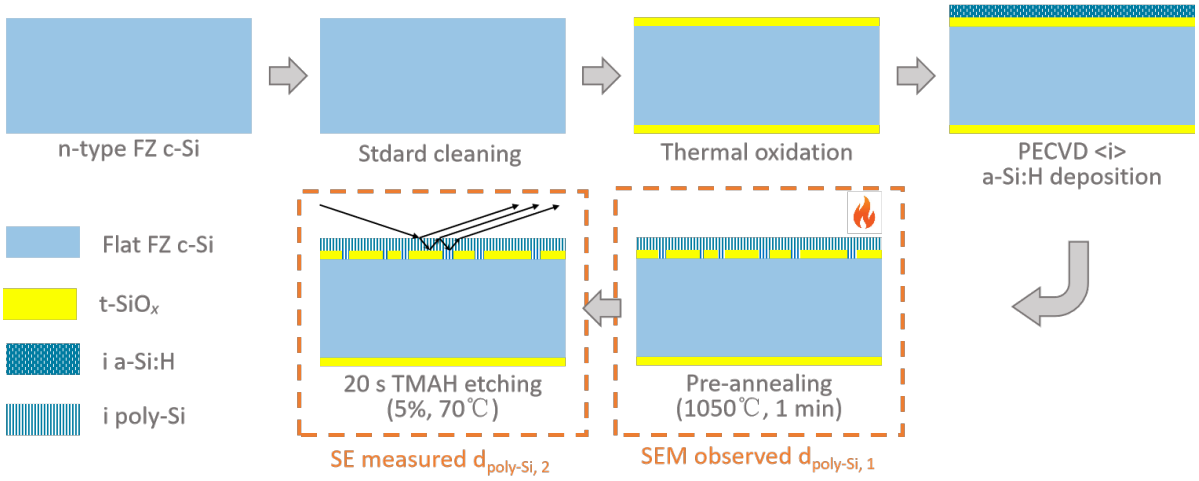

Figure 3.8: Flowchart of the experiment on the etch rate of poly-Si.

Secondly, to look for an optimal etch time for the subsequent investigation of impact brought by RF power, 6 groups of samples with the same poly-Si/SiO_x stack are etched by TMAH for different durations. By comparing the pinhole density, D_{pin}, in each case, an optimal etch time will be obtained. The sample preparation includes the standard cleaning, thermal oxidation, 20 nm PECVD intrinsic a-Si:H deposition under 5 W RF power, and a pre-annealing at 1050°C for 1 minute, as shown in Figure 3.9, TMAH in this case is 5% concentration and at the temperature of 70°C. The test of TMAH etch time varies from 150 s to 300 s, with an interval of 30 s. After etching, each sample is observed by an optical microscope with a magnification of 100.

To calculate the pinhole density, five 1.5 mm by 1.5 mm areas (namely A, B, C, D, E) are taken from each wafer at specific locations, as shown in Figure 3.10a. In each selected area, five 200 µm by 200 µm subareas are taken as shown in Figure 3.10b. By counting the number of pinholes in each subarea, there is pinhole density, such as $D_{pin,B1}$. Averaging $D_{pin,B1}$ to $D_{pin,B5}$, the general pinhole density $D_{pin,B}$ is gained. And the pinhole density, D_{pin}, for the sample is the average value from $D_{pin,A}$ to $D_{pin,E}$. Repeating the previous calculation for each wafer, the result of the final pinhole density is then obtained.

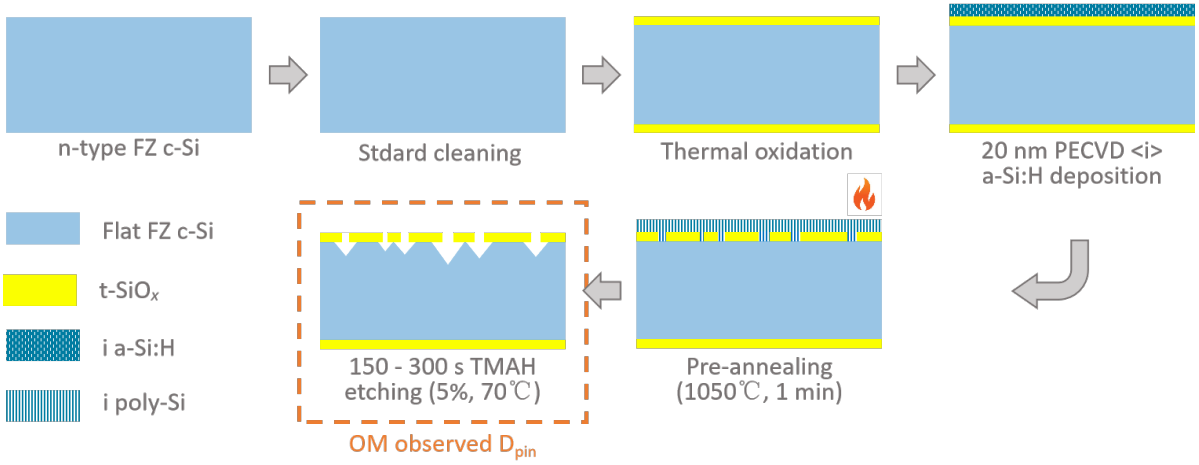

Figure 3.9: Flowchart of the experiment on the optimal etch time determination.

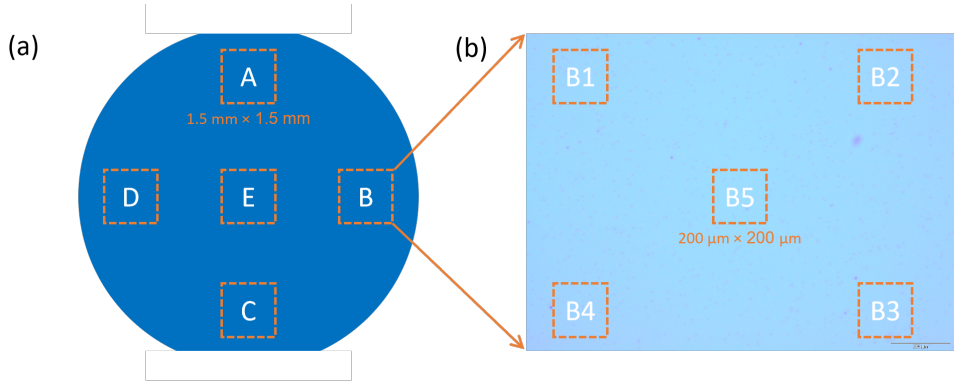

Figure 3.10: Schematic of pinhole density calculation. (a) is the five areas (A-E) selected on each wafer, and (b) is the five subareas selected on area B (B1-B5).

The final part is referring to investigating the pinhole density changing with an increasing RF power in 20 nm PECVD intrinsic a-Si:H deposition. The process is similar to the previous optimal etch time experiment, while in this case, the TMAH etch time is fixed, but the RF power at the PECVD a-Si:H deposition step. The flowchart is shown in Figure 3.11.

Si^{4+} stoichiometry in SiO_x measurement

Since the stoichiometric Si^{4+} in tunnel oxide has a huge impact on passivation quality, and in order to correspond to the subsequent passivation experiment results, the passivated samples are used here, which is double-side symmetrical with a stack of SiN_x:H/n+ poly-Si/SiO_x. To

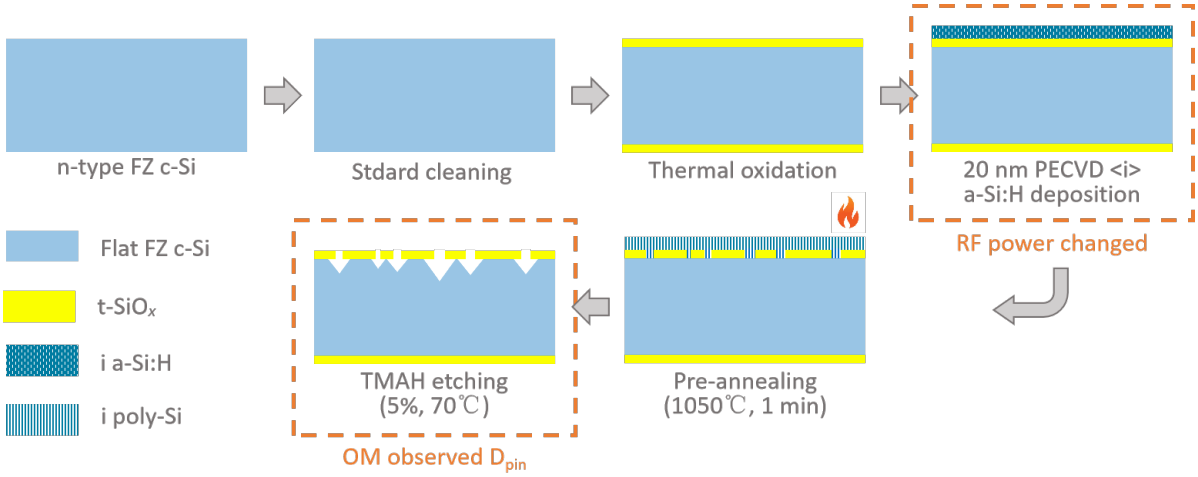

Figure 3.11: Flowchart for investigating that the pinhole density in tunnel oxide changes with an increasing RF power during PECVD intrinsic a-Si:H deposition.

analyze the SiO_x stoichiometry, several steps are adopted to remove the top SiN_x:H and poly-Si layer and expose the SiO_x to the instrument. As demonstrated in Figure 3.12, first step is to immerse the sample into BHF 1:7 solution for 5 min to etch SiN_x:H, followed by a 5-minute DI water rinsing. Then the sample is dipped in 5% TMAH solution at 70°C for 15 seconds and rinsed immediately with DI water for another 5 minutes. The prepared XPS sample is required to be measured as soon as possible. Since ultra-thin SiO_x exposed to the air is fragile, it is easily re-oxidized by oxygen in the air, thus affecting the detection results.

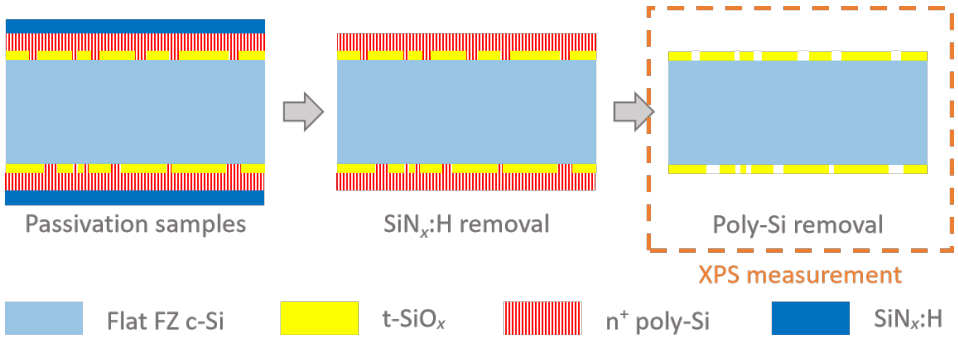

Figure 3.12: Flowchart of XPS measurement for Si^{4+} stoichiometry in SiO_x.

3.2. Impact of RF power on a-Si:H contacting layer

This section focuses on the changes of a-Si:H thin film property when RF power increases. There are four aspects elaborated, including a-Si:H deposition rate and its surface morphology, thin film density, and surface stress.

3.2.1. PECVD a-Si:H deposition rate and growth

As described in Figure 2.4, a RF-generator-connected electrode, a ground-connected electrode and a fast-alternating electric field (called plasma zone) between these two parallel electrodes together consist the basic structure of PECVD equipment. The principle of the deposition pro-

cedure can be divided into two mechanisms. The first one is that a small fraction of atoms or molecules is ionized through random processes, such as thermal collisions. With the electric potential, the positive ions are driven towards the cathode and negative ions or electrons towards the anode. The initial moving ions and electrons would collide and dissociate more precursor gases, resulting in a cascade reaction, shown in Figure 2.5. The electron density in the chamber increases exponentially during this time interval. With the accumulation of charges on the two electrodes, the electric field intensity applied on the plasma zone will be strongly shielded, finally forming a stable plasma. Its macroscopic color will gradually become stable.

The second mechanism is substrate surface reaction. When ions reach the substrate, SiH_3 dominated radicals will diffuse through the surface, find the relatively low energy binding position, and form bond [34][43][49]. The simplified SiH_3 dominated surface reaction model is shown in Figure 3.13.

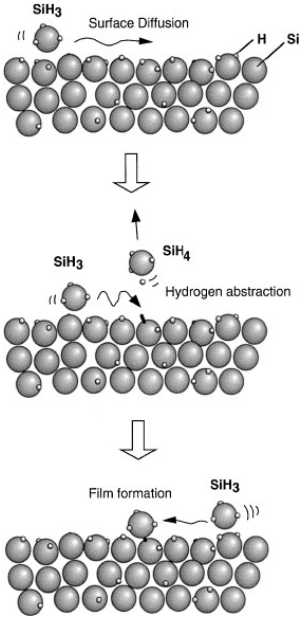

Figure 3.13: Schematic of SiH_3 dominated surface reaction. [49]

When using SE to measure and build a model to simulate the a-Si:H thickness, it is widely agreed that a one-layer model is insufficient to describe the thin film. Collins et al. defined surface roughness layer thickness, d_s, and bulk layer thickness, d_b, as two components of the total a-Si:H thickness [12]. From Figure 3.14Figure 3.14 d_s keeps increasing until saturating to 17 Å. At the meantime, d_b reaches a monolayer thickness of around 2.5 Å. From this time onwards, d_b keeps increasing nearly proportional to the time, whereas d_s declines slightly with a reduction of 4 Å. This film thickness growth trend is consistent with results Fujiwara et al. and Koh et al. reported when d_b < 200 Å and i-layer H_2-dilution ratio R = $[H_2]/[SiH_4]$ < 20 [21][38].

For the above phenomena, many papers put effort on exploring the real process of a-Si:H thin film growth and propose growth models. Canillas et al. proposed three nucleation models, of which cylindrical nucleation assumption is finally in great agreement with the experimental measurement[8], while Collins et al. and Sakai et al. believed the hemispherical structure is more reasonable[12][70]. Although there is no conclusive conclusion on the morphology of the

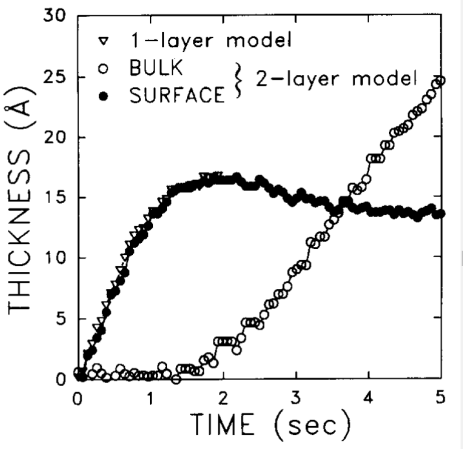

Figure 3.14: Surface and bulk layer thicknesses (solid and open circles respectively) obtained in a linear regression analysis of SE data collected during a-Si:H PECVD onto SiO_2/c-Si at 250 °C. The plasma power flux at the substrate was set at 520 mW cm^{-2}, leading to a deposition rate of 400 Å min^{-1} The acquisition and repetition times for the SE spectra were both 64 ms. The layer thickness in a one-layer model is also shown for the nucleation regime (triangles). [38]

nuclei, it is agreed that there is a nucleation-coalescence mechanism during a-Si:H formation.

Then why is a-Si in the form of nucleation at the early stage of deposition, rather than homogeneous growth? There are four possible reasons. Firstly, at the beginning of the plasma glow, the state of the plasma zone is unstable, and the proportion and density of various growth radicals in the plasma that have not yet reached a steady state are still changing. Secondly, although a flat substrate can be used in this case, it is not realistic that the surface is perfect enough without any lattice defects, such as step and kink sites. Since SiH_3 are more likely to combine with dangling bonds due to the lower binding energy required, it is easy to nucleate at the lattice defect during the early deposition period. Thirdly, in this project, because a-Si:H is deposited on t-SiO_x/c-Si substrate, it also strongly depends on the uniformity of ultra-thin SiO_x. The difference in reactivity with the SiH_3 between c-Si and SiO_x would bring localized growth. Eventually, it is also affected by the difference in reactivity with growth radicals between different substances, the growth radical is more likely to combine with the nuclei instead of the bare substrate. Therefore, the nuclei increase in size.

Corresponding to the previous experimental results in papers, when $d_s < 17$ Å, $d_b = 0$ Å and the deposition is in nucleation mode. When $d_s \sim 17$ Å, d_b starts to increase and d_s approaches the peak value. Continued deposition, d_s slightly decreases and d_b increases, which is in coalescence mode.

Figure 3.15a shows that the thickness of intrinsic a-Si:H grown on t-SiO_x/c-Si substrate increases with time. The experimental results measured by SE are represented by dots, and the lines are fitted thickness growth curves. Different color indicates different RF power. By refitting the slope of the fitted curve in Figure 3.15a, the trend of intrinsic a-Si:H deposition rate as a function of RF power density is plotted in Figure 3.15b.

It can be seen from the figure that when the applied RF power density increases, the growth rate rises continuously, which can be approximately seen as a proportional increase. One of the

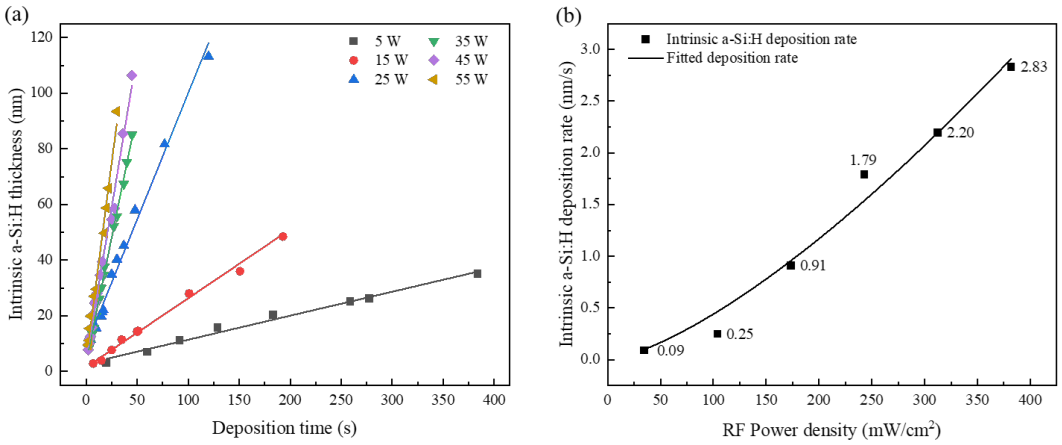

Figure 3.15: (a) Intrinsic a-Si:H thickness for different deposition times when 6 different RF powers are applied. (b) Intrinsic a-Si:H deposition rate increases with PECVD RF-power density.

reasons for this trend can be explained as that higher RF power density promotes higher electrical potential difference U between two electrodes, as Figure 3.16. If an ion with a positive charge of q close to the anode in the plasma zone, it would gain the potential energy $W = qU$. Let's assume the mass of the particle is negligible and it is not subject to any external force. When the ion reaches the cathode, its potential energy will be converted into kinetic energy. When electrons with higher potential energy or kinetic energy collide with precursor gases in the chamber, the probability of elastic collision reduces, and excitation or ionization reaction increases. Consequently, the free radical concentration in the plasma zone is improved. Taking H_2 as an example, H_2 collided by electrons will be decomposed into H^+ and H, etc. [47]. H^+ obtains higher kinetic energy through electric field acceleration, rushes to the substrate at high speed, and breaks some chemical bonds on the surface, thereby more dangling bonds are formed. It provides more opportunities for free radicals to react, thus a-Si:H deposition rate rises. On the other hand, however, higher RF power density also leads to a more severe etching process on the substrate surface, owing to the ion bombardment effect [23]. In other words, the growth rate of a-Si:H by PECVD is the result of the above two competitive processes: thin film deposition and negligible etching effect. Kobayashi et al. reported that even though the etching rate reduces the ideal deposition rate to some extent, overall the increase in growth rate is still large enough to be observed when improving the RF power density [37]. This is also consistent with the trend we observe in the Figure 3.15.

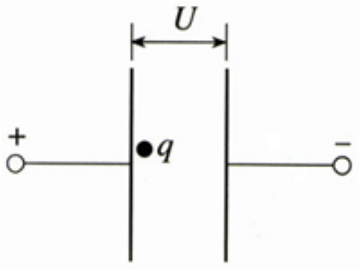

Figure 3.16: Schematic diagram of charged particles in an electrostatic field.

3.2.2. Thin film density of a-Si:H

Hydronated a-Si deposited by PECVD contains a large amount of hydrogen, involving hydrogen molecules and incorporated hydrogen [10]. Norberg et al. reported that from 2% to 40% of the hydrogen could be trapped as molecule H_2 into the a-Si:H network [23]. Furthermore, Si-bonded hydrogen always shows different manners. The simplest corporation is the monohydride (Si-H), where spatially isolated Si-H is accounted up to 4% [56]. More complex bonds, e.g., dihydride (Si-H_2) and trihydride (Si-H_3) species, are grouped preferentially on the internal surfaces of nano-scaled voids with typical dimensions of 5 to 100 Å [10][56].

Another notable structural feature of a-Si:H grown by PECVD is that it contains a significant number of defects, namely vacancy and void. The two are essentially the same, except that in the field of a-Si. For the convenience of communication, the defect missing up to 3 Si atoms is defined as vacancy [81], e.g., monovacancy as Figure 3.17a and divacancy as Figure 3.17b. Correspondingly, the defect missing multiple Si atoms is called void or "microscopic" voids, as Figure 3.17c.

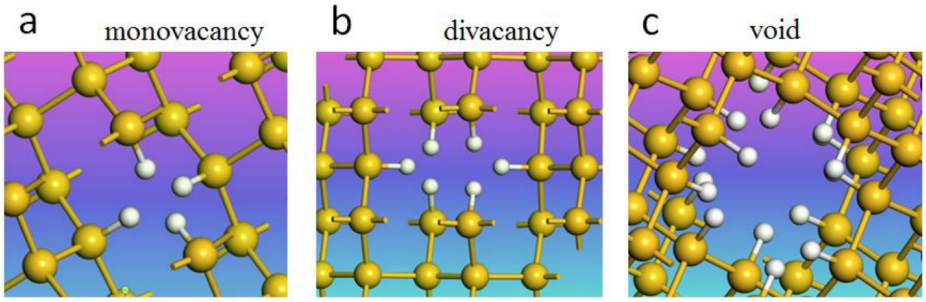

Figure 3.17: Schematic diagram of the structure of (a) monovacancy, (b) divacancy, and (c) void in a-Si:H film. [43]

Information on a-Si:H thin film density is investigated by analyzing the intensity of hybrid absorption modes in infrared spectroscopy. Figure 3.18a shows the spectra of α/ω of 20 nm a-Si:H thin film grown under different RF power (varying from 5 W to 55 W), where α represents the absorption coefficient (a.u.) and ω is the wavenumber (cm^{-1}). Five absorption peaks are observed at 640 cm^{-1}, 845 cm^{-1}, 890 cm^{-1}, 2000 cm^{-1} and 2090 cm^{-1}. The peak of 640 cm^{-1} comes from the wagging vibrational mode [46][53], a doublet at 845 cm^{-1} and 890 cm^{-1} is due to dihydride bending or scissors modes [32][40], and two stretching modes, low-stretching mode (LSM) and high-stretching mode (HSM), occur at the peak of 2000 cm^{-1} and around 2090 cm^{-1}, respectively [40][46][53][69][81].

In Figure 3.18a, peaks between 840-890 cm^{-1} are ignorable at RF power of 5 W, while two peaks appear and their absorption coefficients continue rising when RF power exceeds 15 W. From the literature, peak at 845 cm^{-1} only appears in a-Si:H film at specific deposition conditions, e.g., using Ar and SiH_4 as precursor gases and deposited at high deposition rate over 0.17 nm/s [32]. In our case, each intrinsic a-Si:H thin film is grown at a high rate (> 0.25 nm/s) with Ar, SiH_4 and H_2 as precursor gases, except for the case with RF power of 5 W (0.09 nm/s). This leads us to understand the absence of 840 cm^{-1} peak. On the other hand, peak at 890 cm^{-1} is sometimes related to the appearance of the peak at 2080 cm^{-1} [32], which still needs more verification. However, it is widely agreed that this peak is attributed to Si-H_2 bonding existence [7][9][45][65], which is associated with microvoids.

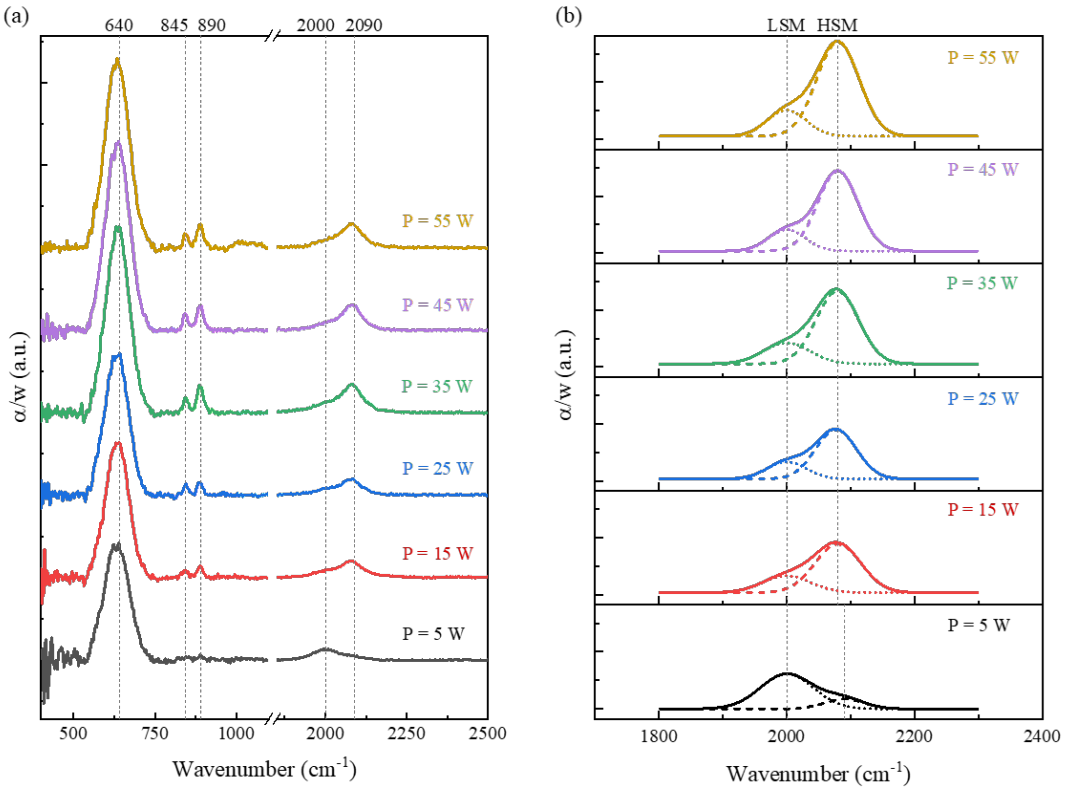

Figure 3.18: The spectra of α/ω, of thin a-Si:H film (∼20 nm) grown at different RF power. (a) shows all peaks in a-Si:H with spectra ranging from 400 cm^{-1} to 2500 cm^{-1}. (b) is the fitted curves of low- and high-stretching modes over the wavenumber from 1800 cm^{-1} to 2300 cm^{-1}. Two fitted peaks are shown in dotted curves and cumulative fitting curves are shown in solid.

Similarly, different performance of peak at 2000 cm^{-1} and 2090 cm^{-1} occurs again between the case of 5 W and the others. With low RF power of 5 W, the absorption coefficient of 2000 cm^{-1} peak is much higher than in other cases. And when increasing RF power, the peak at 2090 cm^{-1} becomes obvious and its intensity absorption increases as well. Peak observed at 2000 cm^{-1} is due to Si-H stretching mode vibration [32]. However, the origin of the peak at 2090 cm^{-1} is still under discussion: (i) overlap of Si-H_2 and Si-H, (ii) overlap of Si-H_2 and Si-H_3, (iii) Si-H_2 with polysilane $(Si\text{-}H_2)_n$, or (iv) clustered Si-H [32]. So far, it agrees with most of the studies that Si-H_2 bonding state contributes significantly to the peak at 2090 cm^{-1}. The presence of Si-H_2 bonds is common for a-Si:H with microvoids. Comparing the peaks between 840-890 cm^{-1} and 2000-2090 cm^{-1} in different cases, it is preliminarily suggested that a-Si:H deposited at higher RF power is likely to contain a large amount of voids.

Absorption peaks positioned from 1800 cm^{-1} to 2300 cm^{-1} are further analyzed and plotted in Figure 3.18b. The original spectra were firstly baseline corrected and then fitted with two peaks that LSM and HSM are initially centered at 2000 cm^{-1} and ∼2090 cm^{-1}, respectively, using Gaussian functions. It is clearly seen that the absorption peak of HSM significantly improved with an increment of RF power. It means that a-Si:H contains more hydrogen and becomes void-rich since the HSM absorption is dominated by Si-H_x at void surfaces [81]. In addition,

interestingly, there is a downward peak shift observed from 2090 cm^{-1} (at 5 W) to 2080 cm^{-1} (exceed 15 W) when increasing RF power. As Arno et al. reported, this shift suggests that both mono- and dihydrides contribute to the HSM [81].

Additionally, the thin film density can be compared quantitively with the assistance of the microstructure factor, R^*

$$R^* = \frac{I_{HSM}}{I_{LSM} + I_{HSM}} \tag{3.4}$$

where I_{LSM} and I_{HSM} are the integral intensities of the LSM and HSM absorption bands, respectively. Since monohydrides (Si-H) in vacancies (monovacancies, divacancies or polyvacancies) contribute to the LSM and clustered hydrogen (Si-H, $Si-H_2$, $Si-H_3$ as well as $(Si-H_2)_n$) on void surfaces to the HSM, the R^* is positively related with the density of microvoids in a-Si:H films [53][69]. Figure 3.19 shows R^* in 6 different RF power cases. As seen from the

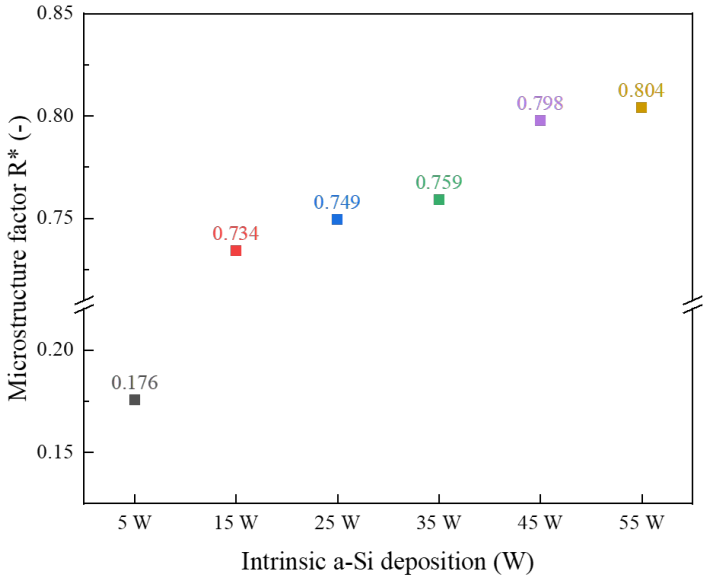

Figure 3.19: Microstructure factor R* of thin (∼20 nm) a-Si:H films as functions of the RF power in PECVD process.

figure, R^* is improved from 0.176 to 0.804 with the increasing RF power. It can be better understood if four competitive processes are introduced: (i) an amount of of H^+ can improve the diffusion rate of SiH_3 radicals in a two-dimensional direction by colliding them with high kinetic energy, which is helpful for SiH_3 radicals to bind at the lowest energy position. The microstructure of a-Si:H film deposited under such growth conditions tends to be more ordered [43]. (ii) Since the atomic mass of hydrogen (m_H = 1.0) is substantially lower than of silicon (m_{Si} = 28.1) or other radicals [46], H^+ can help form dangling bonds on the surface by breaking some weak Si-H bonds, which has a positive effect on ordered growth of thin films. (iii) However, greater electric field strength would easily drive H^+ into the already formed film, and H^+ has a large potential to break the normal Si-Si bonds, inducing lattice disorder

in the growing film [23]. (iv) a-Si:H deposition is always accompanied by a large number of microvoids. At high deposition rates, these microvoids are quickly covered by newly formed nano-sized layers [43].

Thus, when RF power is relatively low (5 W), the deposition rate is quite slow ($\sim$0.09 nm/s), and processes (i) and (ii) play a more significant role. In contrast, when RF power is higher than 15 W in this project, the deposition rate exceeds 0.25 nm/s, processes (iii) and (iv) dominate the deposition, and the formed a-Si:H becomes more porous.

3.3. Impact of RF power on underlying SiO_x

The influence of PECVD RF power is not only on the formed a-Si:H film but also on the underlying tunnel SiO_x due its ultra-thin thickness. Two properties of SiO_x are involved. The first is using an optical microscope to observe pinholes on the surface and count its pinhole density. Then use XPS to measure and calculate Si^{4+} stoichiometry in SiO_x.

3.3.1. Impact of RF power on pinhole density in SiO_x

Verification of Si/SiO_x selectivity in TMAH

Figure 3.20 shows the SEM-measured thickness of (a) a-Si:H and (b) poly-Si films before TMAH etching. The average thicknesses of samples are 247 nm for a-Si:H and 215 nm for poly-Si. After 20 s etching in 5 wt.% TMAH at 70°C and 5 min water rinsing, each sample was measured and fitted by SE, showing the thickness reduction of $\sim$137.7 nm (a-Si:H) and $\sim$176.3 nm (poly-Si). A similar procedure was done for t-SiOx samples, except that the etch time was extended to 60 s, leading to a thickness reduced to 1.142 nm. As calculated, the etch rates of each film are 413.1 nm/min (a-Si:H), 528.9 nm/min (poly-Si), 0.268 nm/min (t-SiO_x), summarized in Table 3.1.

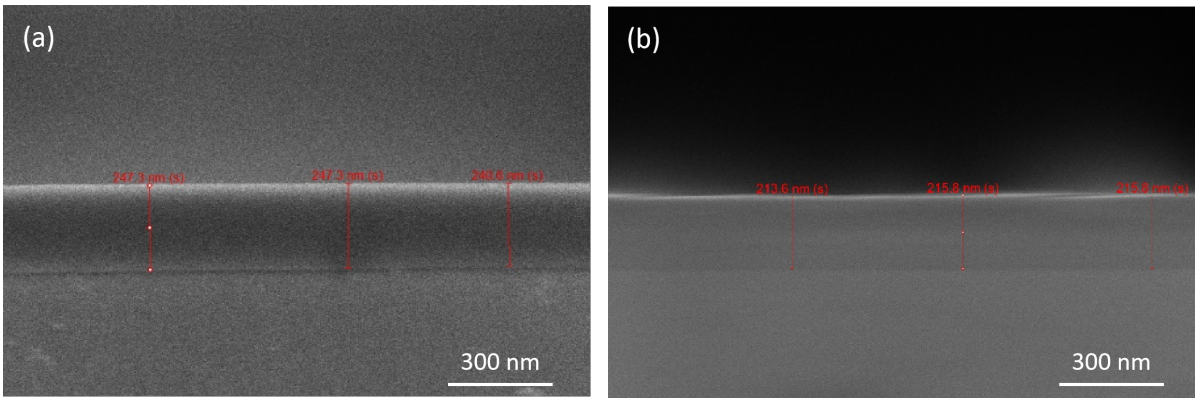

Figure 3.20: SEM images of thickness measurement for (a) a-Si:H and (b) poly-Si films before TMAH etching.

Table 3.1: Etch rate of a-Si:H, poly-Si and t-SiO_x

	Average thickness (nm)		Etch time (s)	Etch rate (nm/min)
	Before etching	After etching		
a-Si:H	247 ± 3	109.3 ± 2.5	20	413.1
Poly-Si	215 ± 3	38.7 ± 1.9	20	528.9
t-SiO_x	1.41 ± 0.04	1.142 ± 0.06	60	0.268

It is suggested that the etch rate for <100>Si is larger than poly-Si and much larger than a-Si [88]. Obtained from Figure 3.21, the theoretical etch rate of <100>Si in 5 wt.% TMAH (70°C) should be around 500 nm/min, lower than the measured poly-Si etch rate. This difference might originate from the increment of TMAH solution concentration due to water evaporation when heating the solution. Further, the etch rate of t-SiO_x is 0.268 nm/min, much higher than 0.052 nm/min for SiO_2 from MicroChemicals [51]. It is because the silicon oxide prepared in our lab is not pure SiO_2, which is relatively easily etched away in TMAH. Additionally, this value is larger than 0.125 nm/min in the literature as well [72]. It can be attributed to that different oxidation conditions would form an oxide layer with different density, which has different etch rate in TMAH solution.

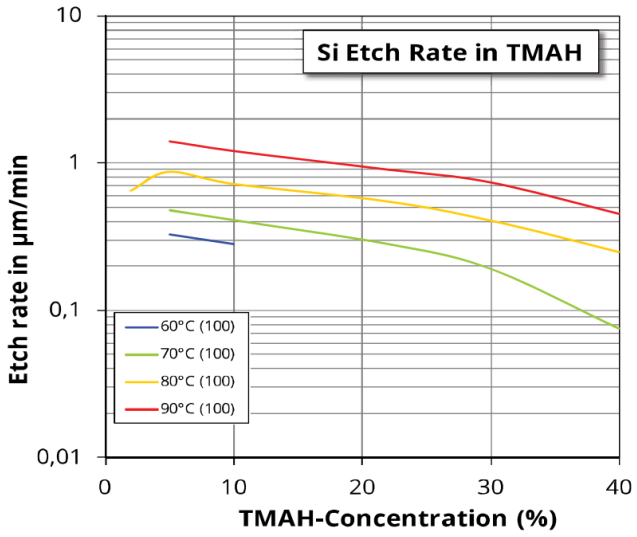

Figure 3.21: The concentration and temperature-dependent etching rate of (100) in TMAH. [51]

Shown as Table 3.2, the etch rate ratio of a-Si:H/t-SiO_x and poly-Si/t-SiO_x are around 1541 and 1974, respectively. Although there is a huge difference between them with what we expected in the literature (not much less than 9600), it is still large enough to protect t-SiO_x when samples are etched by TMAH for no more than 5 min.

Table 3.2: Etch rate ratio between different materials.

Etch rate ratio	**a-Si:H/t-SiO_x**	**poly-Si/t-SiO_x**	**<100>Si/t-SiO_2**
From measurement	1541	1974	-
From literatures	-	-	9600

3.3.2. Optimal etch time determination

This part is to look for a suitable etch time for the following experiments. From Figure 3.22a, it is hard to observe pinholes with 150 s etch time. It is due to the etching through the pinholes is quite slow, that the surface area of the pinhole is too small to be visible. Extending the etch time from 180 s, pinholes start to appear and intuitively, become larger and denser.

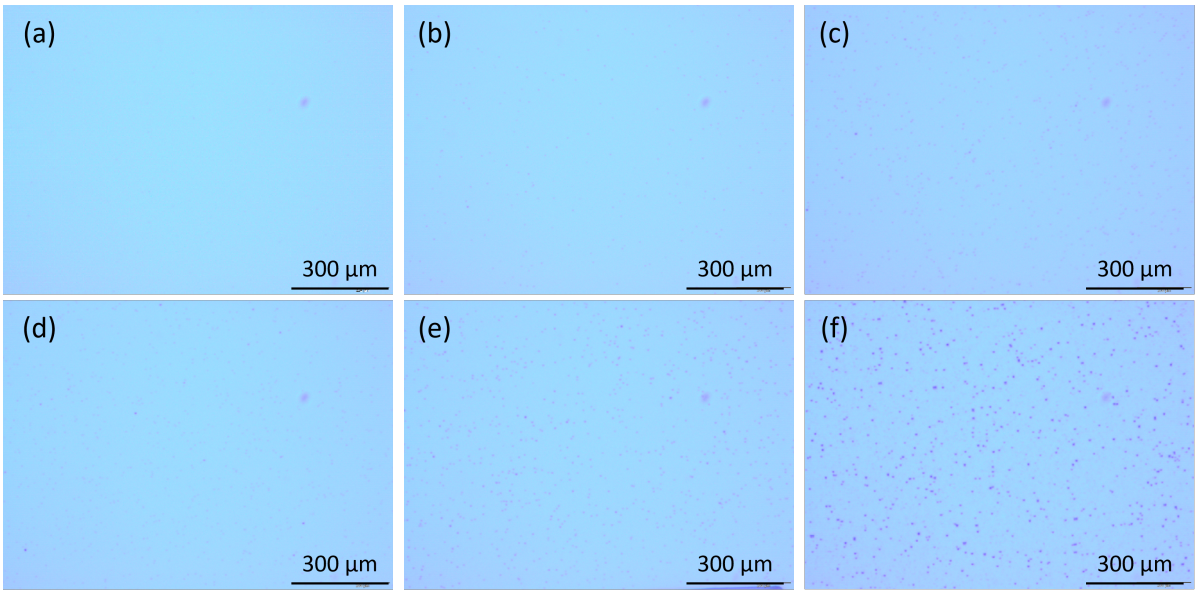

Figure 3.22: Optical microscopic images of pinholes in t-SiO_x with different etch time in 5 wt.% TMAH at 70°C. From (a) to (f), etch time increases from 150 s to 300 s, with intervals of 30 s.

The calculated pinhole density over different etch times is summarized in Figure 3.23, except for 150 s. From 180 s to 240 s, pinholes are easy to distinguish and its density ranges from 3.22×10^6 cm^{-2} to $4.73 \times 10^6 cm^{-2}$. After that, pinhole density increases rapidly, accompanied by large error bars. Combined with the last two images in Figure 3.22, it can be explained that part of the pinholes is too large to be isolated from their neighbours, which is not suitable for observation. In order to improve the accuracy of the pinhole density and leave a more workable range of subsequent experiments, 180 s was selected as the optimal etch time.

Pinhole density changed with RF power

Using 5 wt.% TMAH solution at 70°C to etch the samples prepared at different RF powers as well as a reference sample grown by LPCVD, the pinhole density of each case is calculated and plotted as Figure 3.24. The results show that the pinhole density keeps rising from 2.16×10^7 cm^{-2} to 4.75×10^7 cm^{-2}, until RF power reaches 25 W. The possible reason causes this trend is similar to one of the competitive processes that we introduced for R^* analysis in Section 3.2.2.

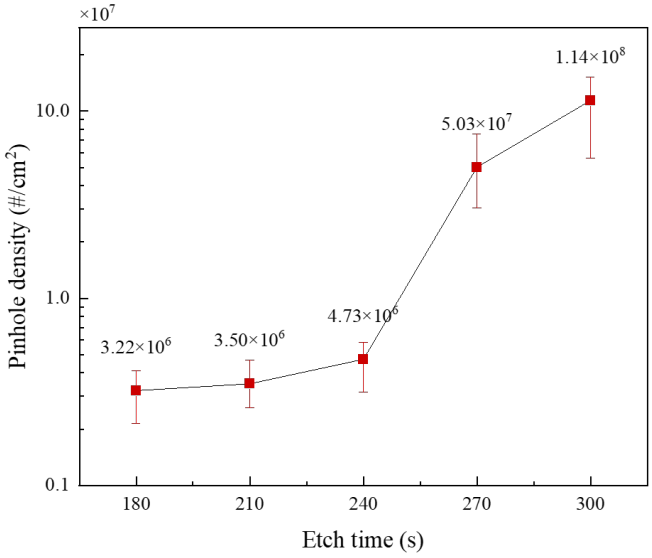

Figure 3.23: Pinholes density in t-SiO_x with different etch time from 180 s to 300 s.

When applying large RF power density, the high electric field strength would make light atoms or ions, such as H^+ obtain large kinetic energy and drive them to break the bonds (Si-O in this case) on the substrate surface. Such behaviour can also be named ion bombardment.

Then a slight decrease of pinhole density presents with a ten-Watts increment of RF power to 35 W. Interestingly, however, much fewer pinholes are formed when further improving the RF power to 45 W or 55 W. The pinhole density at 55 W is 1.48×10^7 cm^{-2}, even lower than that at 5 W. It is easier to understand if a guess about the "protective layer" is proposed. The protective layer, namely the buffer layer in this project, belongs to a-Si:H film and is formed at the very beginning during the deposition. It only appears when extremely high RF power is applied (> 35 W). Thanks to the high RF power, the film deposition rate is significantly improved. Although ion bombardment tends to damage the substrate, the quickly formed buffer layer would protect the underlying t-SiO_x from ion bombardment. This is why pinhole density drops between 35 W and 55 W.

3.3.3. Impact of RF power on Si^{4+} stoichiometry in SiO_x

Under the particle bombardments induced by PECVD a-Si:H deposition, the quality of the chemical bonding configuration (Si-O) has the probability of being modified. The silicon oxide layer consisted mainly of SiO_2 (Si^{4+}), whereas the sub-oxide region at the interface was comprised of intermediate oxidation states, i.e., Si_2O (Si^{1+}), SiO (Si^{2+}), and Si_2O_3 (Si^{3+}). It has been widely agreed that the high compactness of SiO_2 stoichiometric configuration will contribute to a good passivation quality [28], compared to other sub-oxides. For figuring out the chemical structure, X-ray photoelectron spectroscopy measurements are normally used to obtain the Si-O bonding configurations, corresponding to the number of Si-O bonds on an Si atom.

We did the XPS measurements on 7 samples. XPS spectra in Figure 3.25a focusing on Si 2p

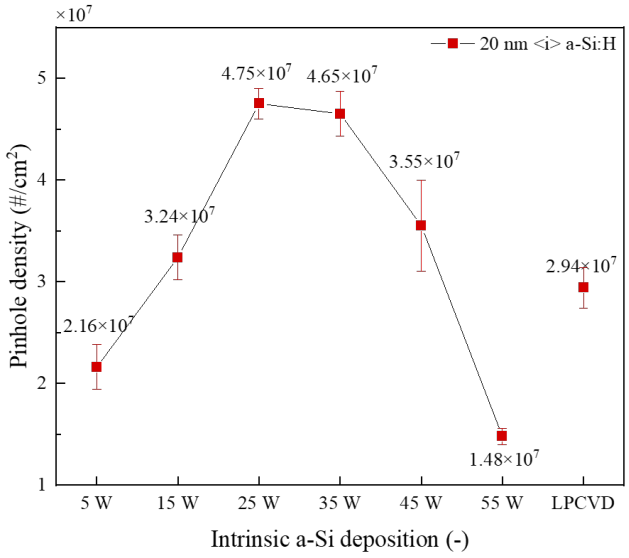

Figure 3.24: Pinhole density calculated in different RF power cases with a constant a-Si:H thickness of 20 nm.

bond and fraction fitting is plotted in Figure 3.25b, involving the peaks of Si 2p 3/2 and Si 2p ½, Si^{1+}, Si^{2+}, Si^{3+} and Si^{4+}. In order to exclude the result deviation caused by the difference status of instrument status in each measurement, all the peaks in Figure 3.27b are calibrated with a C 1s peak of 284.75 eV. The raw intensity spectra is deducted by a Shirley background, and then a semi-quantitative analysis of the constituents of SiO_x is performed to evaluate the quality changes of SiO_x film.

After calibration, the lower binding energy peak near 99.5 eV is related to the bulk Si, where two peaks for Si 2p 3/2 and Si 2p ½ are centred at 96.98 eV and 98.53 eV. Further, the higher binding energy peak near 103.4 eV is attributed to SiO_2 [36], while the deviation is because of the existence of sub-oxide region. In Figure 3.27b, the oxide region was fitted with four peaks of their position at around 99.54 eV (Si^{1+}), 100.65 eV (Si^{2+}), 101.43 eV (Si^{3+}), and 102.86 eV (Si^{4+}). It is observed that a 0.2 eV downward shift of Si^{4+} peak position occurs in the case of 25 W and 35 W, while the same value upward shift occurs in 55 W. Since these shift values are close to the instrument limitation of binding energy identification, which is 0.2 eV as well, the peak position of Si^{4+} in all cases is regarded to be same.

Among different species, the percentage of Si^{4+} species is a good indicator to quantify the SiO_x film, as shown in Figure 3.26. The Si^{4+} stoichiometry is found to be 26%, the lowest at 25 W, whilst experiencing a 8% - 9% improvement when increasing RF power to 55 W or reducing to 5 W. It means that the SiO_x in 25 W sample has the worst quality than the others, which is consistent with the results found in Section 3.3.1. Combining Figure 3.24 and Figure 3.26, it is found that the large pinhole density corresponds to the cases of low stoichiometry of Si^{4+}. This proves to some extent that the severe particle bombardment brought by strong power would weaken or directly break the Si-O bonds in the PECVD substrate, that is the t-SiO_x in our case.

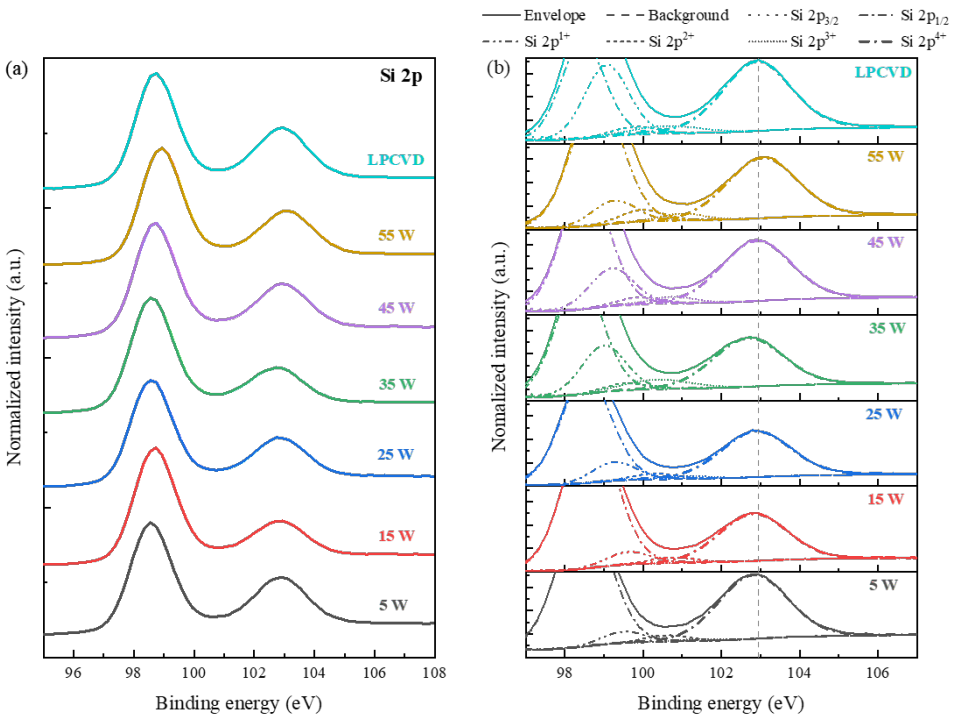

Figure 3.25: (a) Comparison of XPS spectra of SiOx impacted by a-Si:H deposition at different RF power after normalization and calibration. (b) Fraction fitting (Si 2p 3/2 and Si 2p ½, Si^{1+}, Si^{2+}, Si^{3+} and Si^{4+}) of XPS spectra of SiO_x in different RF power cases.

3.4. Pinhole formation principle in SiO_x

After analyzing the impact of RF power on SiO_x thin film, it is found that there is a correlation between pinhole density and Si^{4+} stoichiometry in t-SiO_x. This section is to explore the origin of pinholes in tunnel SiO_x. Firstly, the whole period before pinhole observation is divided into three processes. During each process, the potential factors contributing to pinhole formation will be analysed according to the experimental results in this project and principles from the literature. Finally, a trade-off analysis between possible factors is applied to verify the behaviour of pinhole density variation in the cases.

Process of t-SiO_x fabrication

As the chemical reaction described with Equation 3.5, the species, O_2, is used to grow thermal oxide. The ideal model assuming an abrupt transition from bulk c-Si to SiO_2 is shown as Figure 3.27. In this model, the tetrahedral bonding of c-Si is achieved by bonding to the O atoms of the oxide [87].

$$Si + O_2 \rightarrow SiO_2 \tag{3.5}$$

However, a number of results obtained via XPS, TEM, and SREM suggest that there is a transition region between the c-Si and the top SiO_2 [31][68][91]. As Ikarashi et al. demonstrated, c-SiO_2 at the oxidation front is a necessary process for oxidation to occur, which agrees with

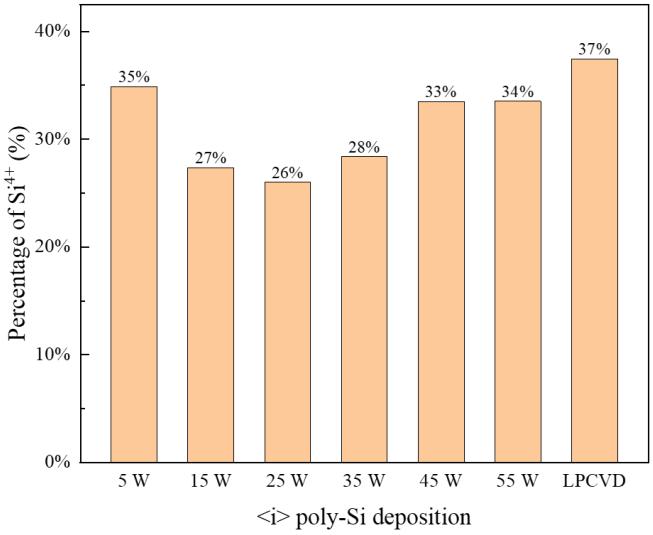

Figure 3.26: Comparison of the percentage of four valence configurations of the Si-O bonds in the SiO_x films obtained by fitting the Si 2p XPS spectra in seven cases.

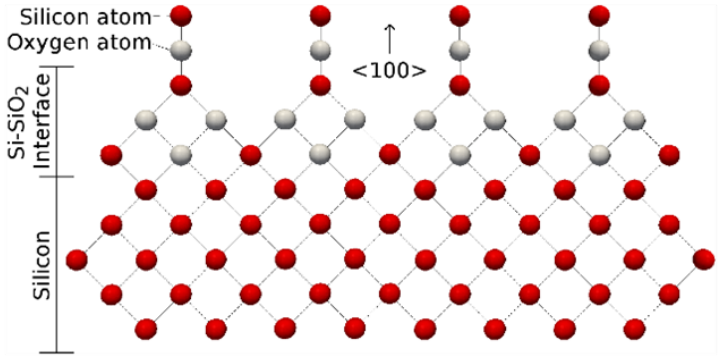

Figure 3.27: Ideal atomic configuration model for the c-Si/SiO_2 interface. [31]

the initial model in Figure 3.27. And vertical growth is preferred by Si-oxide. After the first atom-layer oxidation, it is observed that vertical oxidation is suppressed at the top of the oxidation protrusion, while the c-Si surface provides a probability for O atoms to form Si-O bonds on the Si backside. Alternatively, the back-bond oxidation can proceed vertically below the SiO_2 layer for at least two more atomic layers. As the area of c-SiO_2 increases, a crystalline-amorphous transition will occur due to the large elastic strain at the interface, shown as Figure 3.28. The newly formed a-SiO_x region tends to allow more vertical back-bond oxidation. It is worth to be noticed that due to the disordered structure in a-SiO_x region, intermediate oxidation states will present, namely sub-oxide. Similar results are reported in [55][77][85] as well. As reported, the size of the transition region can reach 20 Å at certain oxidation conditions. And since this region is amorphous, there are an amount of weak and dangling bonds, which raises the possibility of pinhole formation in the subsequent processes. The improved model is shown in Figure 3.29. [20][33]

On the other hand, there are excess Si remaining in the c-Si from the oxidation process due to

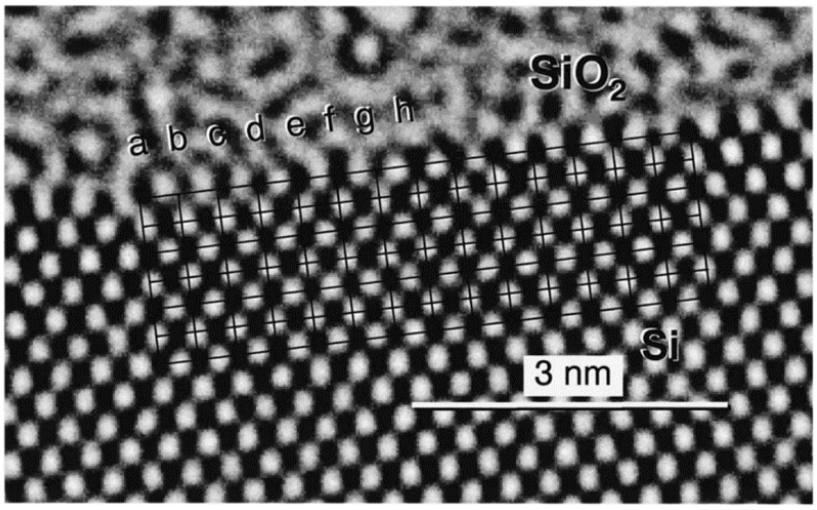

Figure 3.28: <110> cross-sectional HREM image of a SiO_2/Si(100) interface. Each black dot corresponds to a Si atomic dumbbell. The rectangular lattice shows the periodicity of the atomic dumbbell in bulk Si. [31]

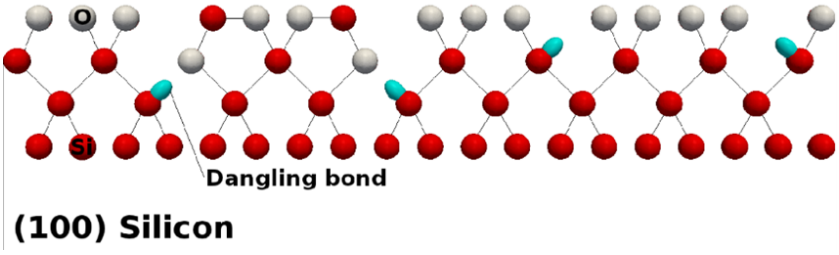

Figure 3.29: Improved atomic configuration model for the c-Si/a-SiO_x interface. [31]

incomplete conversion of Si to SiO_2. Some excess Si atoms occupy interstitial positions and are implanted as "self-interstitial atoms" from the oxidized interface into the bulk c-Si. Self-interstitials nucleate at strained centers of Si, generating extrinsic stacking faults, which is also observed by other reports, shown in Figure 3.30. It leads to the horizontal nonuniformity of the SiO_x film. [29][33]

Process of PECVD a-Si:H deposition

As analysing in section 3.2.1 and 3.3.1, when applied large RF power (> 5 W), ions with light atomic mass such as H^+ tend to obtain large kinetic energy, causing server particle bombardments on the substrate surface. Such bombardments have the potential to weaken or break Si-O in t-SiO_x, which has been prooven by Si^{4+} stoichiometry detection in section 3.3.2. Furthermore, due to the thin film's island growth, even if the a-Si on the surface can be detected with a thickness of a few nanometers, the SiO_x region still exposed to the plasma continues to be bombarded. Nevertheless, with the much higher RF power (> 25 W), the buffer layer is formed quickly and covers the entire substrate surface, protecting underlying SiO_x from high kinetic energy particles.

Process of annealing

Figure 3.31 is the Raman spectra of 40 nm thick n-type poly-Si layers in 7 cases, which initially consist of 20 nm intrinsic a-Si:H and 20 nm n-type a-Si:H, and then experience two-step

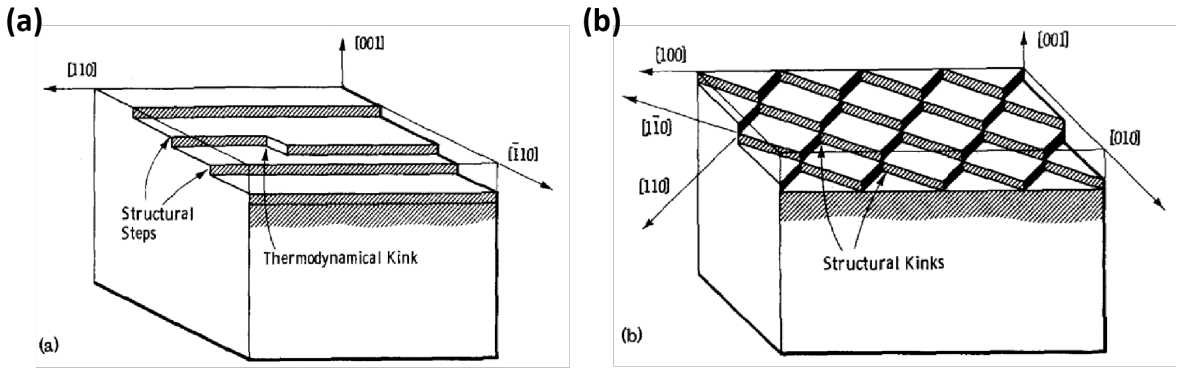

Figure 3.30: Schematic representation of the <111> surfaces (a) and the <101> surfaces (b), with thermodynamic and structural kinks. [29]

annealing. Each sample is detected to have a peak at 520 cm^{-1}, and all curves are highly overlapping, implying the same crystallinity. However, the results from Figure 3.19 show that the intrinsic a-Si:H contains more SiH_2 content and becomes porous from 5 W to 55 W, indicating they have different crystallization processes.

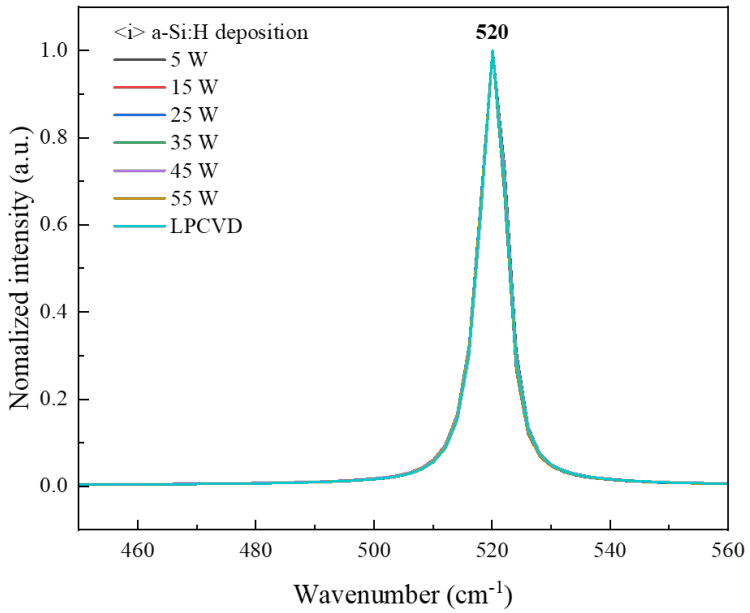

Figure 3.31: Raman spectra of 40 nm thick poly-Si layers deposited on 1.41 nm t-SiO_x/c-Si after annealing at 900°C for 30 min.

Total stress in a-Si:H film itself consists of the contribution from both intrinsic stress and thermal stress. The thermal stress results from the mismatch of the thermal expansion coefficients of the film and the substrate as the sample cools from deposition temperature to room temperature. Assuming the thermal stress value in all the samples will remain identical and only intrinsic stress will change depending on the deposition parameters. Thus, the change in the

total stress will be largely due to varying intrinsic stress in the film in this case [11]. The intrinsic stress of a-Si:H is different for samples prepared at different RF power. From Ong's results, the intrinsic stress (compressive) increases with the RF power [58]. And high compressive stress in a-Si:H layers originates most likely from H introduced into a-Si:H network [22]. corresponding to the trend in Figure 3.19.

Compressive stress in a-Si:H will become larger when annealing, until several large grains formed due to Si-H bonds broken and lattice reformation. This large internal compressive stress will produce a large tensile stress externally, applying to the underlying SiO_x. Tensile stress applied on SiO_x contributes to the breakage of Si-O bonds and morphological changes, shown as in Figure 3.32.

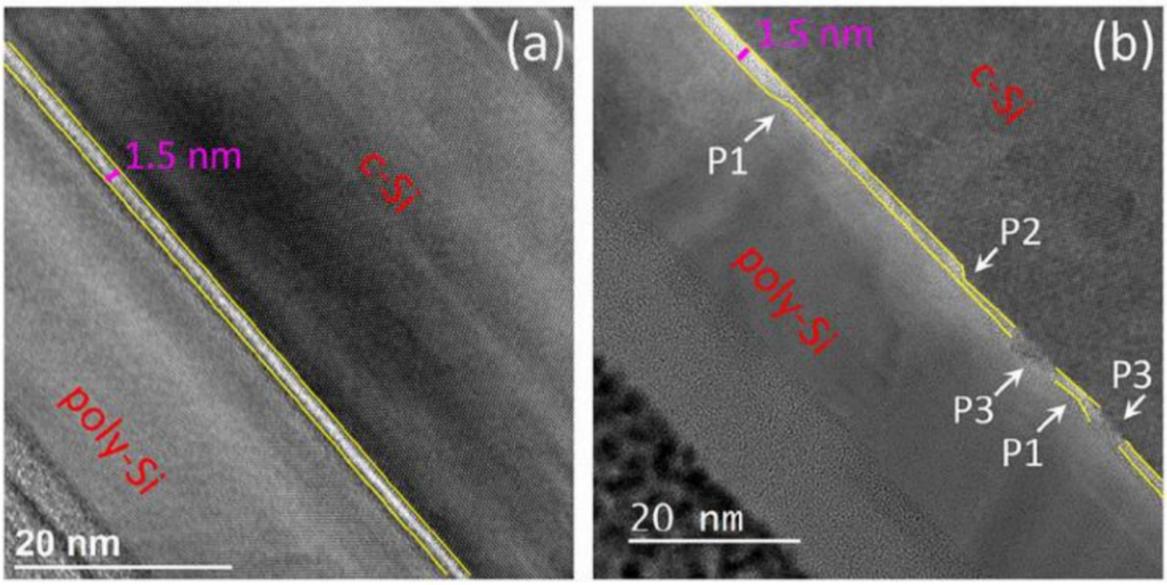

Figure 3.32: Cross-sectional HR-TEM images of poly-Si/SiO_x/c-Si annealed at (a) 800°C and (b) 900°C. [44]

To conclude, there are five factors that contribute to pinhole formation: (i) Defects in SiO_x thin film from imperfect oxidation leave potential to pinhole formation. (ii) Huge ion bombardments in PECVD deposition are allowed to weaken or break Si-O in t-SiO_x. (iii) Island growth of a-Si:H makes the exposed region of SiO_x continue to be bombarded. (iv) Quick buffer layer formation protects the substrate from ion bombardments. (v) The tensile stress applied by a-Si:H films during annealing intensify the formation of pinholes.

In this project, there is a balance of the influence between these factors on the pinhole formation in t-SiO_x. As demonstrated in Figure 3.33, from 5 W to 25 W, the negative impact of ion bombardment and interface tensile stress, together with the imperfect oxidation and a-Si:H island growth, dominates the increment of pinhole density. In contrast, from 35 W to 55 W, the positive effect of the buffer layer compensates for the previous drawbacks, leading to pinhole density reduction.

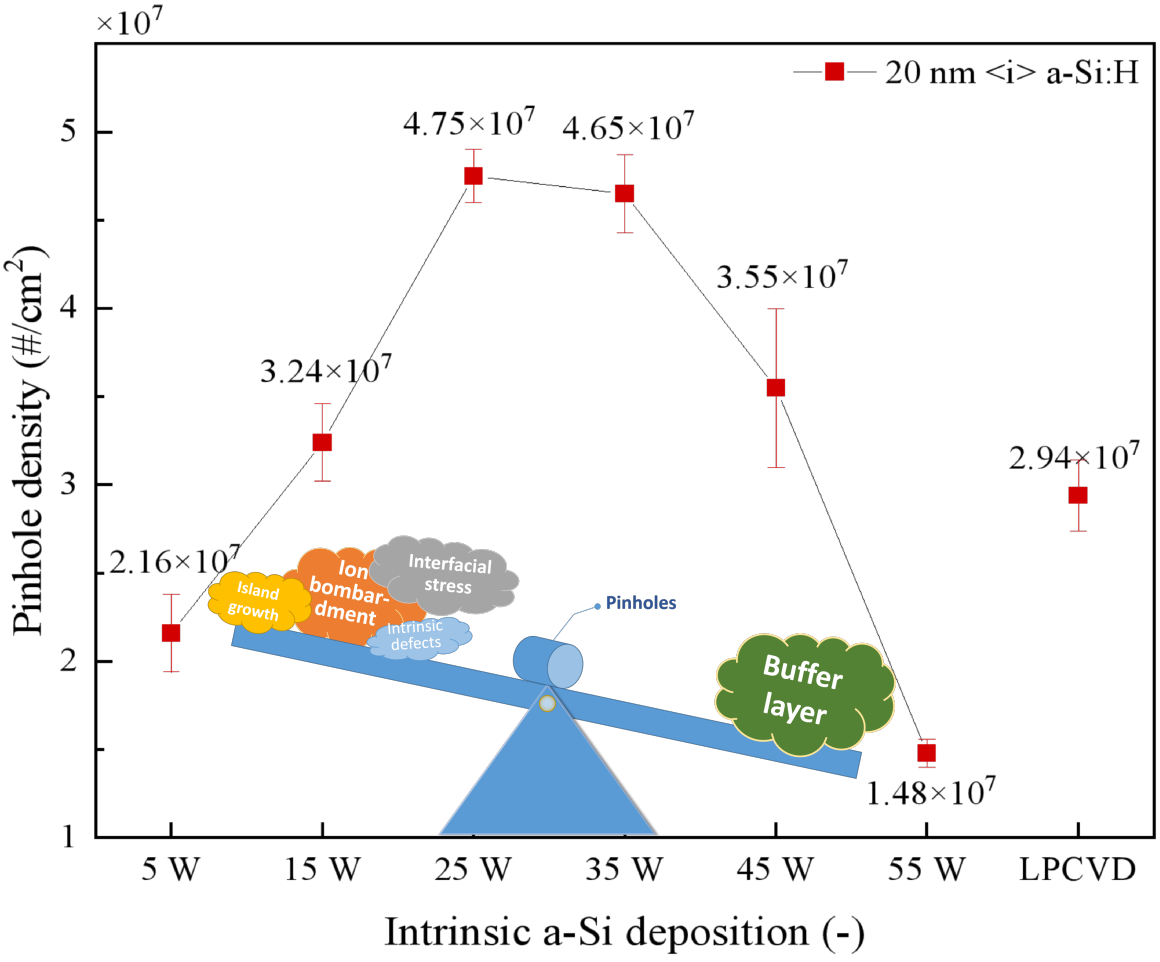

Figure 3.33: Schematic diagram of the impact of different factors on pinhole density.

4

Impact of PECVD a-Si:H deposition on poly-Si/SiO_x passivating contact

After investigating the a-Si contacting thin film properties caused by increasing RF power, the performance of formed passivating contact will be measured and compared in this chapter. Section 4.1 will briefly describe the sample preparation processes. Combining section 4.2 and section 4.3, the influence of RF power on the passivation level and the change of its intrinsic mechanism will be studied and discussed. Finally, the carrier selectivity of passivation contact will be quantified and compared in section 4.4.

4.1. Experimental objective and method

As the results in chapter 3, changes in RF power are found to affect characteristics of both a-Si:H and its underlying SiO_x thin film. Apart from the a-Si:H growth rate and density, the impact on pinhole formation in the tunnel oxide layer seems to be more noticeable. Tunnel oxide plays an important role in poly-Si/SiO_x/c-Si passivating contact, since it not only acts as a barrier to limit the in-diffusion of dopants from doped poly-Si to bulk c-Si, but also provides excellent chemical passivation to reduce the dangling bonds on c-Si surface. In addition, the carrier transport mechanism in tunnel oxide has been widely discussed. It is agreed that both tunneling transport and pinhole-assisted transport coexist in SiO_x. The presence of pinhole has a complex impact on passivation quality and contact resistivity, thereby influencing the carrier selectivity of passivation contact. Therefore, this chapter focuses on the impact of RF power on carrier selectivity of passivation contact, where varied pinhole density is a crucial factor to help analyze.

The study in this chapter includes three parts. Firstly, the passivation quality is evaluated for the passivation samples. Then, the doping concentration distribution is detected by ECV measurement. Subsequently, a measurement regarding the contact resistivity is performed. And lastly, the carrier selectivity of passivation contact prepared with different RF power is compared and discussed.

Passivation quality evaluation

As shown in Figure 4.1, Passivation quality evaluation is achieved by measuring J_0 and iV_{oc} by photoconductance lifetime tester. Two-step measurement is performed after post-annealing and FGA annealing process, respectively. Then four parameters measured as post-annealing and FGA will be obtained, represented as $J_{0,post-ann}$, $J_{0,FGA}$, $iV_{oc,post-ann}$ and $iV_{oc,FGA}$.

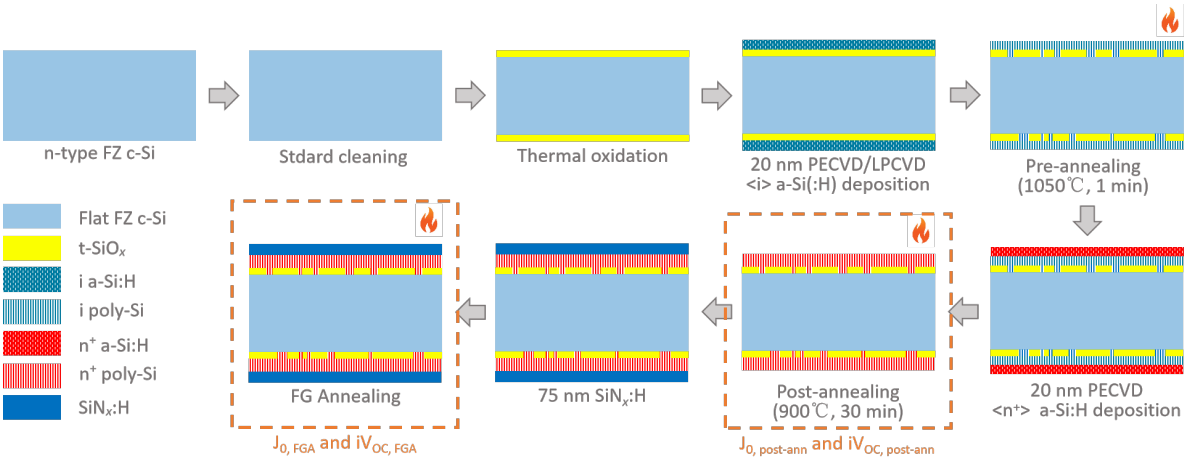

Figure 4.1: Flowchart for the passivation evaluation of double-sided symmetric samples.

Active P dopant distribution detection

After passivation quality evaluation, same samples are cleaved into 4 quarters. One of them will be etched by BHF 1:7 solution for 5 min to remove SiN_x:H layer on the surface. Then they will be sent to TNO for ECV measurement. Its flowchart is shown in Figure 4.2.

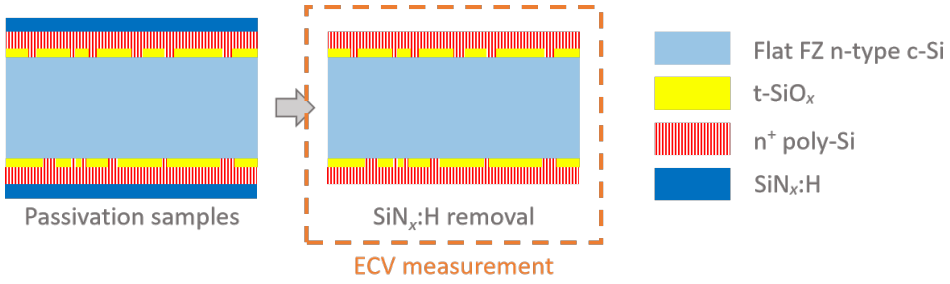

Figure 4.2: Flowchart of ECV measurement.

Contact resistivity measurement

Another one quarter of the passivation samples are used to prepare the contact resistivity samples. After 5 min BHF 1:7 etching and 5 min DI water rinsing, the samples are then evaporated with 500 nm Ag by PROVAC instrument. The final contact resistivity calculation is based on Cox-Strack method and performed with WACOM, which is a kind of Current-Voltage measurement instrument. The flowchart for sample fabrication is shown in Figure 4.3.

4.2. Passivation quality of passivating contacts

This section is to present the passivation quality of passivation samples in all different preparation conditions. Figure 4.4 plots the passivation parameters of samples at 2 statuses, after

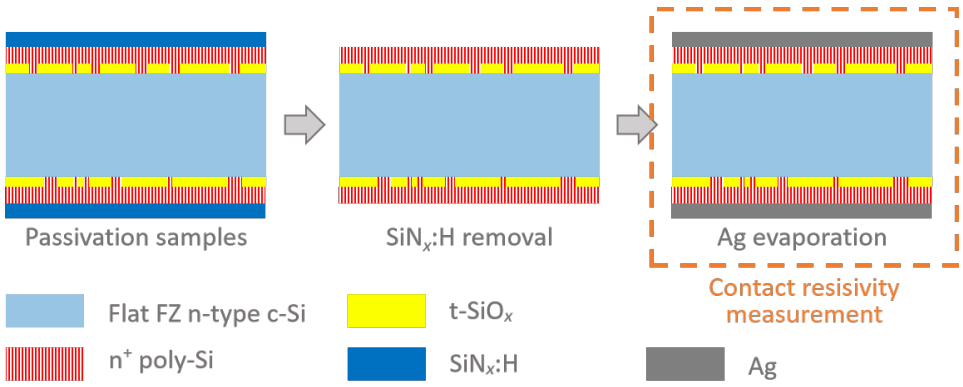

Figure 4.3: Flowchart of specific contact resistivity measurement.

post-annealing and after "SiN_x + FGA" hydrogenation, as a function of RF power, in which the left graph is the variation of J_0 and results of iV_{oc} is shown on the right. The LPCVD sample as a reference group, is also involved.

Firstly, it is clear from Figure 4.4 that the passivation level of almost each sample is improved after hydrogenation regardless of RF power or different fabrication methods, except for 5 W. The opposite trend occurring at 5 W is attributed to the blistering issue observed during the experiment, resulting in 22.5 fA/cm^2 and 29 mV reduction in J_0 and iV_{oc}, respectively. The unexpected issue in the 5 W sample makes it probably better not to focus on the absolute value of the 5 W case, instead, to observe the overall trend in combination with other cases. For the PECVD samples (except for 5 W), the curves of J_0 and iV_{oc} are relatively flat before hydrogenation, while a clear hump appears after hydrogenation. This enhanced behaviour will be explained in the next section.

Then, interestingly, the trends of passivation parameters variation are consistent with that of pinhole density. To be specific, the increment of iV_{oc} or J_0 is always accompanied by the rise of pinhole density in PECVD samples. Among six PECVD cases, the best passivation level is found in the case of 25 W, with J_0 of 3.3 fA/cm^2 and iV_{oc} of 714 mV, corresponding to the highest pinhole density in Figure 3.24. Although the passivation of the champion PECVD sample is lower than the LPCVD sample, it is still comparable, since the difference can be attributed to the degraded chemical passivation from lower Si^{4+} stoichiometry [92].

Additionally, it is good to notice that when performing the intrinsic a-Si:H deposition at 25 W and 35 W, a wide range of RF power leads to an iV_{oc} higher than 710 mV, with single side J_0 not over 3.5 fA/cm^2. As a result, a large optimal process window for RF power adjustment is left for n-type passivating contact optimization.

4.3. Active P dopant distribution

To further investigate the relationship between the poly-Si fabrication conditions and passivation quality, electrochemical capacitance–voltage measurements for all PECVD and LPCVD samples are performed. Two comparison groups are categorized in Figure 4.5. The cases whose pinhole density is positively correlated to the RF power are compared in Figure 4.5a, and those that have a negative correlation are in Figure 4.5b. Since the LPCVD sample is the reference group, it is involved in both two graphs.

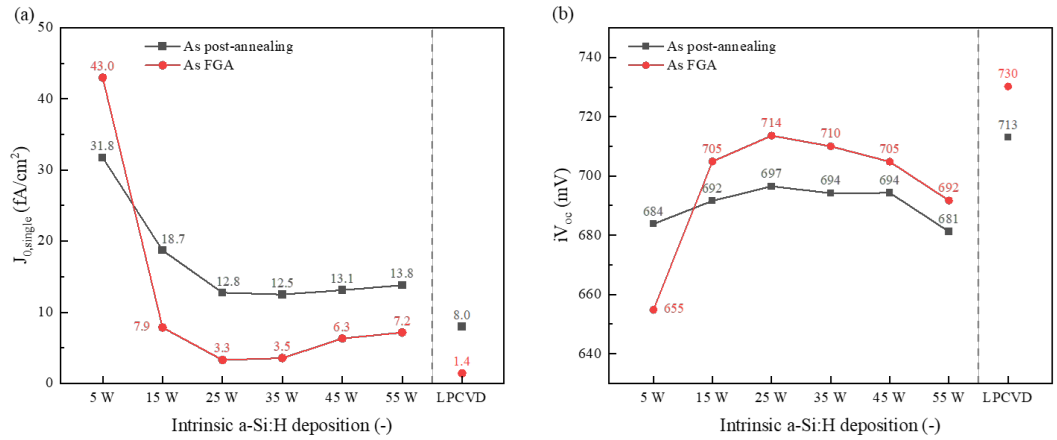

Figure 4.4: Passivation quality in terms of (a) J_0 and (b) iV_{oc} of the phosphorous-doped poly-Si based passivating contacts after post-annealing and FGA hydrogenation. The samples contain intrinsic a-Si:H films under different deposition conditions or methods before post-annealing.

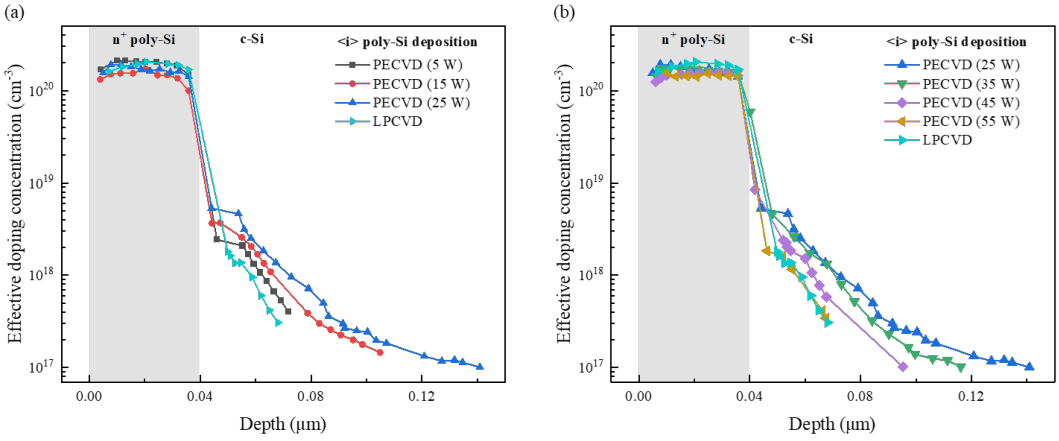

Figure 4.5: Measured effective doping profiles by ECV for passivating samples. The cases of intrinsic a-Si:H deposited at 5 W, 15 W, 25 W or by LPCVD are compared in (a), and deposited at 25 W, 35 W, 45 W, 55 W or by LPCVD method are compared in (b).

In general, the effective phosphorous doping concentration is around 2×10^{20} cm^{-3} in all cases. Seen from Figure 4.5a, a deeper P diffusion tail is along with the increasing RF power from 5 W to 25 W. On the contrary, it becomes shallower from 25 W to 55 W on the right. But if from the view of pinhole density, it is found that the deep in-diffusion is always accompanied by a large pinhole density in PECVD samples. Since the ion bombardments create a pinhole in SiO_x, as we discussed in Chapter 3, the poly-Si and the bulk c-Si are in direct contact at the pinhole region. During annealing, the dopants can be driven into bulk Si more efficiently, thus resulting in a long diffusion tail.

In addition, by combining Figure 4.5 with Figure 4.4, it can be observed that the deepest in-diffusion corresponds to the highest passivation level in PECVD cases, that is at 25 W. The difference between it and others results from the enhanced field-effect passivation, which is contributed by the excess of dopants diffusion into the bulk c-Si [96].

However, the benefits of the enhanced field-effect passivation have not been well represented as post-annealed. The samples from 25 W to 55 W only experience a slight variation of iV_{OC} and J_0 before FGA, that are 16 mV and 1.3 fA/cm^2, respectively, even though with the large pinhole density difference. Taking 25 W and 35 W as examples, the 25 W sample has the largest pinhole density and the deepest dopant in-diffusion, but its passivation level is close to or even lower than that of 35 W. With the hydrogenation of SiN_x:H and FGA processes, the passivation quality at 25 W is improved and exceeds that at 35 W. This can be explained similarly as the previous results: as pinhole formed by ion bombardments, more excess dopants get access to the bulk c-Si, improving the field-effect passivation. On the other hand, severe surface defects accompanying pinhole region cannot be ignored. It would enhance the surface recombination, degrade the chemical passivation performance [92], and offset the improvement of field-effect passivation. Nevertheless, such local defect-enriched region will be significantly passivated during the subsequent hydrogenation, thereby mitigating the degradation of surface passivation. Thus, hydrogenated 25 W has better passivation behaviour than hydrogenated 35 W. This also answers the remaining question in section 4.2, why the hump occurs only after hydrogenation from 15 W to 55 W.

Finally, comparing the champion sample to the LPCVD case, although the in-diffusion of the latter is shallower, it shows an outstanding passivation behaviour over all the cases. In this case, there are three factors needs to be considered. Firstly, the shallower in-diffusion brings less Auger recombination into in-diffusion region [92], which contributes to the performance. Secondly, observed from Figure 3.26 LPCVD sample contains the highest Si^{4+} stoichiometry, meaning that better tunnel SiO_x would provide a better surface passivation. Thirdly, the less field-effect passivation owing to shallow in-diffusion cannot fully offset the benefits of passivation improvement brought about by the previous two factors.

4.4. Specific contact resistivity

Apart from the passivation quality, contact resistivity is also an essential property of the passivating contact. In this project, contact resistivity measurements were performed with Cox-Strack method. In this method, two opposite sides of the sample are measured between two probes. The obtained total resistance R_T consists of three parts, described as Equation 4.1:

$$R_T = R_c + R_s + R_0 \tag{4.1}$$

Where R_c is the contact resistance of the top contact on the semiconductor, R_s is the spreading resistance in the semiconducting substrate, and R_0 is the residual resistance of backside contact [93].

In our case, the contact samples are symmetrical structure. On each side, a SiO_x/poly-Si stack contact is firstly fabricated on the c-Si substrate. To prepare the electrode, 500 nm metal Ag is evaporated on the top. Therefore, the R_c contains two parts, the contact resistance between the doped poly-Si and the metal Ag as well as the contact resistance between the SiO_x/poly-Si stack and the bulk c-Si. Since the contact resistance between metal and the doped poly-Si is quite small compared to the latter resistance, it can be ignored in this measurement. Further, R_0 is equal to R_c due to the symmetrical structure. The Equation 4.1 is rewritten as Equation 4.2:

$$R_T = 2 \times R_c + R_s \tag{4.2}$$

Assuming the current flow is uniform and the contact is isotropic, R_c is further expressed in terms of contact resistivity ρ_c, as:

$$R_c = \frac{\rho_c}{A_c} \tag{4.3}$$

where A_c is the total area of the top contact.

As calculated, the specific contact resistivity ρc of the SiO_x/poly-Si passivating contact in each case is plotted in Figure 4.6. As expected, the contact resistivity experiences a decline from 5 W to 25 W, then rises back to 136 mΩ·cm^2 from 25 W to 55 W. The reduction of contact resistivity corresponds to a higher pinhole density. And the lowest ρc is found at 25 W, which is 34 mΩ·cm^2. This trend is attributed to the carrier transportation in the sample. Generally,

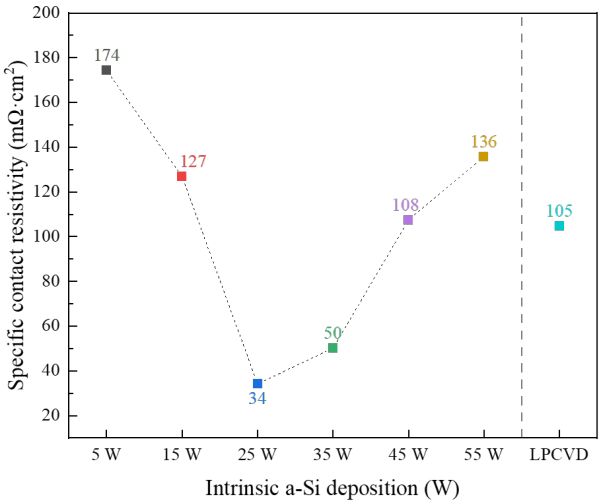

Figure 4.6: Specific contact resistivity of contact samples as a function of RF power, involving LPCVD samples as reference group.

there are two transport mechanisms in SiO_x, including direct transport through pinholes and tunnelling through the SiO_x layer. The dominated mechanisms strongly depend on the SiO_x thickness. In our case, the thickness of t-SiO_x is around 1.41 nm, and the classical tunnelling effect contributes the most to the carrier transport. However, due to lots of pinholes formed in each case, the pinhole transportation should be considered as well. Wei et al. proposed a model of ρ_c as a function of pinhole density D_{pin}, shown as Figure 3.24 [97]. From the simulated figure, $\rho_{c,tun}$ is constant regardless of how the pinhole changes, while $\rho_{c,pin}$ is negatively proportional to the pinhole density. When the pinhole density is less than 10^5 cm^{-2}, the overall contact resistivity ρ_c is consistent with $\rho_{c,tun}$. When pinhole density is higher than 10^7 cm^{-2}, it obeys the variation of the $\rho_{c,pin}$. If in between, ρ_c is a function of both $\rho_{c,tun}$ and $\rho_{c,pin}$.

All the samples in this project contain a huge amount of pinholes (> 10^7 cm^{-2}). Thereby, the contact resistivity is proportional to the pinhole density. This explains why the lower contact resistivity is along with the higher pinhole density.

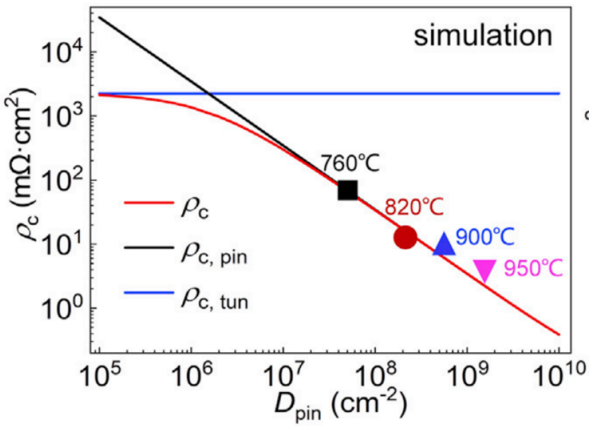

Figure 4.7: Different type of contact resistivity changes with increasing pinhole density D_{pin}. ρ_c is the overall contact resistivity of the SiO_x/poly-Si passivating contact, $\rho_{c,pin}$ is the contact resistivity via pinholes, and $\rho_{c,tun}$ represents that via tunnelling. [97]

4.5. Carrier selectivity

High performance passivating contact is supposed to have a higher carrier selectivity, that is to allow one type of the electric carrier to transport while repelling another kind. The one that allows electrons to migrate more efficiently is so-called "electron-selective contact". Attributing to the chemical passivation achieved by tunnel oxide and field-effect passivation provided by phosphorous-doped poly-Si, the SiO_x/n-type poly-Si passivating contact shows its outstanding performance in many reports.

Figure 4.8 is a typical band diagram of an electron-selective contact with a SiO_x/n^+ poly-Si structure. The carrier selectivity in this structure depends on three mechanisms. (i) Due to the work function difference between the n-type c-Si and heavily doped n^+ poly-Si, the n^+ poly-Si layer causes a band bending at their interface. The created band bending is an ideal barrier for holes to get access to the SiO_x, in the meantime, electrons would pass easily from bulk c-Si to the n^+ poly-Si. (ii) SiO_x plays an important role and acts as a second barrier. It is reported that tunnel oxide presents a barrier of 4.5 eV for holes, while for electrons it is reduced to only 3.1 eV [41]. It indicates that electrons would require less energy to tunnel through. (iii) Owing to the band gap, there are a few or no states in the n^+ region where holes can tunnel.

In other words, carrier selectivity is related to the resistivity of the contact to the majority and minority carriers, respectively [73]. Schmidt et al. and Brendel et al. reported a simplified method for selectivity calculation [6][73]. Determining resistivity for the majority carrier and minority carrier are ρ_M and ρ_m, respectively. ρ_M is equal to the contact resistivity ρ_c at the point of operation.

$$\rho_m = \frac{V}{qR(V)} \tag{4.4}$$

$$\rho_M = \rho_c \tag{4.5}$$

where V is the internal quasi-Fermi level splitting and q is the elementary charge. Then the ratio between them is

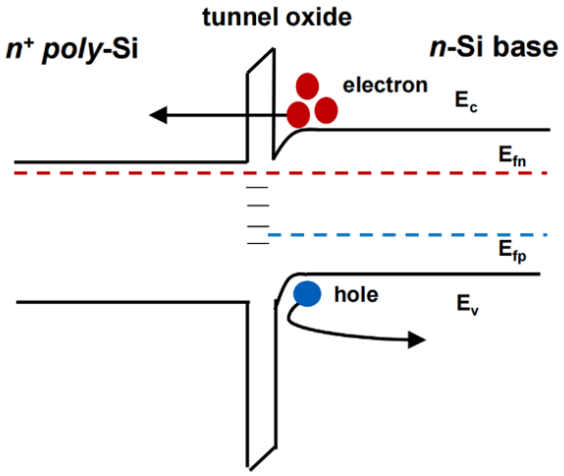

Figure 4.8: Band diagram of the tunnel oxide passivated contact structure [97]

$$\frac{\rho_m}{\rho_M} = S(V)g(V) \tag{4.6}$$

where $g(V)$ is a voltage-dependent factor, and carrier selectivity can be written as

$$S(V) = \frac{V_{th}}{\rho_c(\frac{q(R(V)}{e^{(\frac{V}{V_{th}})}-1})} \tag{4.7}$$

where V_{th} is the thermal voltage, which is produced within the P-N junction due to the action of temperature. It's value is a constant of about 26 mV at room temperature [4]. To simplify the Equation 4.7 and only focus on the ultimate device performance, the maximum power point is chosen. The selectivity is therefore expressed as

$$S = \frac{V_{th}}{\rho_c J_0} \tag{4.8}$$

where J_0 is the recombination current density. And the logarithmically scaled selectivity is commonly used:

$$S_{10} = log_{10}(S) \tag{4.9}$$

S and S_{10} are voltage-independent now. The calculated carrier selectivity as intrinsic a-Si:H deposition conditions changes is compared in Figure 4.9. Combining the champion passivation level with the lowest contact resistivity, the sample with RF power of 25 W gains a high carrier selectivity of 14.37. It is worth noting that although LPCVD sample enjoys a much higher passivation performance, the relatively high contact resistivity limits its selectivity to 14.25, with 0.12 lower than the champion case.

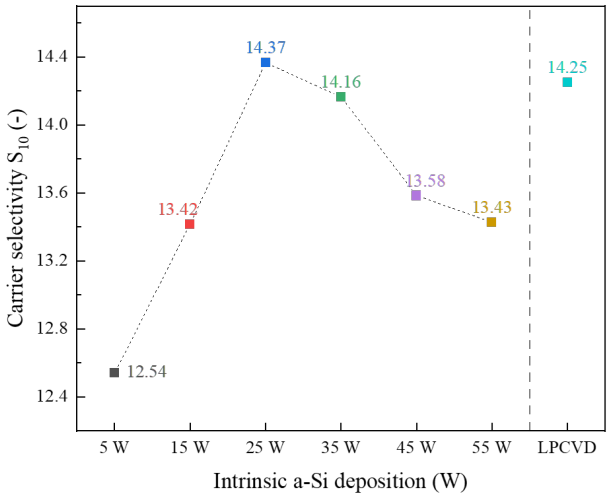

Figure 4.9: Carrier selectivity of contact samples with intrinsic a-Si:H fabricated in different RF conditions or by LPCVD method

Moreover, carrier selectivity S_{10} as an intuitive indicator of passivating contact performance directly shows the efficiency potential of an ideal crystalline silicon solar cell with a single-selective contact of S_{10}. Assuming the c-Si substrate is 110 µm thick, Lambertian light trapping and with a resistivity of 2 Ω·cm, a positive correlation between maximum efficiency η_{max} and selectivity S_{10} is described as Equation 4.10 and plotted in Figure 4.10. As can be seen from the figure, the champion passivating contact with a selectivity of 14.37 in this project is expected to yield a maximum efficiency of 28.9% in c-Si solar cell.

$$\eta_{max} = ((2.452S_{10} - 4.240)^{-19.52} + (29.21)^{-19.52})^{-\frac{1}{19.52}}\% \tag{4.10}$$

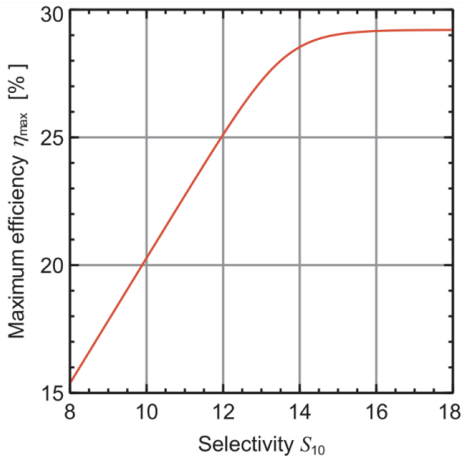

Figure 4.10: Maximum efficiency $\eta_{max}(S_{10})$ assuming a 2 Ω·cm n-type c-Si wafer of thickness W = 110 µm with Lambertian light trapping (J_{sc} = 43.6 mA/cm^2) and intrinsic bulk recombination with a single contact of selectivity S_{10}. The second contact is assumed to be ideal. [73]

5

Conclusions and outlook

The main goal of this thesis project was to investigate the impact of PECVD a-Si:H contacting layer deposition in the poly-Si-based carrier selective passivating contacts. The approach was based on studying the changed properties of each contained thin film layer when increasing the RF power. To better analyse the intrinsic principles, pinhole density in tunnel oxide were measured and as a bridge between RF power and passivating contact performance. Additionally, a pinhole formation mechanism were proposed based on several possible influence factors.

5.1. Conclusions

Preliminarily, one of the most intuitive effects of increased RF power is the higher growth rate brought to amorphous silicon. With increasing RF power, the largely improved a-Si:H deposition rate dominates the thin film formation process, even though always accompanied by a negative impact from hydrogen etching which is negligible. The second impact on a-Si:H growth is the thin film density. The absence of peak between 840-890 cm^{-1} in the case of 5 W is attributed to the RF power density (< 0.25 nm/s) , while the obvious Si-H_2 dominated peak at 2090 cm^{-1} and its enhanced intensity absorption in the case from 15 W to 55 W suggest that a-Si:H grown at higher RF power is likely to contain a large amount of voids. It is then confirmed by the calculation of microstructure factor R^*. The increment of R^* from 0.176 to 0.804 indicates the porous Si thin film is formed by increasing RF power.

Secondly, The influence of PECVD RF power is not only on the deposited a-Si:H film, but also on the underlying tunnel SiO_x due its ultra-thin thickness. The changes in two properties of SiO_x are studied. The first is regarding the pinhole density inspection and calculation. To visualize the pinhole under optical microscope, the concepts of "selective etching" and "pinhole magnification" are applied. After verifying the sufficient Si/SiO_x selectivity in TMAH solution, 180 seconds etch time is determined to be the optimal duration for "pinhole magnification". Then, with two-step five-point sampling method, the pinhole density was calculated ranging from 1.48×10^7 cm^{-2} to 4.75×10^7 cm^{-2}. An increasing number of pinholes were formed when RF power improved from 5 W to 25 W resulted from severe ion bombardment, while reduced pinhole density was found when further increasing it. To explain the latter trend,

a concept of "protective layer" was proposed in this thesis, which is defined as a buffer layer formed at the very beginning during a-Si:H deposition. It only appears when extremely high RF power applied (> 35 W). Another influence on tunnel oxide property is discussed according to the result from XPS measurement. The percentage of Si^{4+} species is found to be highest in the case of 25 W, corresponding the highest pinhole density calculated earlier. This proves to some extent that the severe particle bombardment brought by strong power would weaken or directly break the Si-O bonds in the PECVD substrate, that is the t-SiO_x in our case.

As a result, the possible reason of pinhole formation is analysed in three processes during sample fabrication: the process of thermal oxidation, the process of PECVD a-Si:H deposition and the process of annealing. Finally, five factors contribute to the pinhole formation: (i) Defects in tunnel oxide thin film from imperfect oxidation leave potential to pinhole formation. (ii) Huge ion bombardments in PECVD deposition is allowed to weaken or break Si-O in tunnel oxide. (iii) Island growth of a-Si:H makes the exposed region in tunnel oxide continue to be bombarded. (iv) Quick "protective layer" formation protects the substrate from ion bombardments. (v) The tensile stress applied by a-Si:H films during annealing intensifies the formation of pinholes.

In addition, the unexpected result from the passivation quality assessment is that a higher passivation level is presented with higher pinhole density. The best passivation quality is found in the case of 25 W, with J_0 of 3.3 fA/cm^2 and iV_{oc} of 714 mV. Combining distribution of the active dopant from ECV measurements, deeper in-diffusion occurs at 25 W indicates that a large amount of pinholes have the potential to provide a great passage for dopants to diffuse into bulk silicon. The heavily doped area in the c-Si close to the interface enhanced the field-effect passivation. Although a severe Auger recombination is expected, it does not seem to be able to offset the improvement from field-effect passivation. On the other hand, the passivation of the champion PECVD sample is lower than LPCVD sample, but it is still comparable since the difference can be attributed to the degraded chemical passivation from lower Si^{4+} stoichiometry. Additionally, it is good to notice that when performing the intrinsic a-Si:H deposition at 25 W and 35 W, a wide range of RF power leads to an iV_{oc} higher that 710 mV, with single side J_0 not over 3.5 fA/cm^2. As a result, a large optimal process window for RF power adjustment is left for n-type passivating contact optimization. As summary, a good passivation performance is achieved by a combination of the following factors: (i) less Auger recombination which is brought by a shallower in-diffusion, (ii) sufficient field-effect passivation which results from appropriate in-diffusion, and (iii) excellent surface passivation which is provided by more intact tunnel oxide.

Then, the specific contact resistivity is obtained via Cox-Strack method. It is suggested that the contact resistivity is positively correlated to the pinhole density, which is due to the improved pinhole transport in tunnel oxide. Therefore, the lowest value of 34 mΩ·cm^2 is found at 25 W.

Eventually, the carrier selectivity of each case is calculated and compared. It is worth noting that although LPCVD sample enjoys a much higher passivation performance, the relatively high contact resistivity limits its selectivity to 14.25, with 0.12 lower than the champion case. And the champion passivating contact with a selectivity of 14.37 in this project is expected to yield a maximum efficiency of 28.9% in c-Si solar cells. It proves that an outstanding carrier selectivity relies not only the passivation quality but also the contact conductance in between.

5.2. Outlook

This project has proposed few new insights into pinhole formation and illustrated some unexpected influences of PECVD method on passivating contacts and. However, there are still much room for improvement, which could be realized by further research into different tunnel oxide formation method, p-type poly-Si-based passivating contact and optimization with RF power. The method of tunnel oxide fabrication can be replaced by wet-chemical (NAOS) or PANO-SiO_x. NAOS tunnel oxide is less dense and might be less resistant to ion bombardments. PANO-SiO_x is achieved by PECVD method, which can be combined with PECVD a-Si:H deposition, thus greatly reducing the risk of the intermediate transfer process. It is thereby well worth studying the impact on the NAOS-SiO_x and PANO-SiO_x.

Additionally, since boron has higher diffusion rate, reducing boron in-diffusion in c-Si is an issue that needs to be fixed. When ion bombardment from PECVD is induced, this matter will become more severe. Therefore, it is more challenging to investigate the impact of p-type poly-Si passivating contact.

For future research into pinhole formation, the analysis in this thesis is limited. The role of some factors, such as interfacial stress and “protective layer” is still waiting to be verified.

Based on passivating contact behaviour, a wide optimal working window was given. It is beneficial to further investigate and optimize the RF power for higher performance. Finally, since the study in this project only stays at the impact on passivating contact, further research into the application of solar cells is needed to be performed and evaluated.

References

[1] A.G Aberle, S. W. Glunz, and A.W. Stephens. “Higheficiency silicon solar cells: Si/SiO_2, interface parameters and their impact on device performance”. In: *Progress in Photovoltaics: Research and Applications* 2.4 (1994), pp. 265–273.

[2] A.G. Aberle, S. Glunz, and W. Warta. “Field effect passivation of high efficiency silicon solar cells”. In: *Solar Energy Materials and Solar Cells* 29.2 (1993), pp. 175–182.

[3] A.G. Aberle, S. Glunz, and W. Warta. “Impact of illumination level and oxide parameters on Shockley–Read–Hall recombination at the $Si - SiO_2$ interface”. In: *Journal of Applied Physics* 71.9 (1992), pp. 4422–4431.

[4] All about Circuits. *Introduction to Diodes And Rectifiers*. URL: `https://www.allaboutcircuits.com/textbook/semiconductors/chpt-3/introduction-to-diodes-and-rectifiers/` (visited on 08/24/2023).

[5] J. Brcka and R.J. Sundar Gandhi. “Exploration COMSOL in Modeling RLSATM CVD Processes in Ar^+ $H_2{}^+$ $SiH_4{}^+$ C_2H_6 and Dopant Gas”. In: (2013).

[6] R. Brendel and R. Peibst. “Contact selectivity and efficiency in crystalline silicon photovoltaics”. In: *IEEE Journal of photovoltaics* 6.6 (2016), pp. 1413–1420.

[7] M.H. Brodsky and M. Cardona. “Infrared and Raman spectra of the silicon-hydrogen bonds in amorphous silicon prepared by glow discharge and sputtering”. In: *Physical Review B* 8.16 (1977), p. 3556.

[8] A. Canillas, E. Bertran, and J.L. Andújar. “In situ spectroellipsometric study of the nucleation and growth of amorphous silicon”. In: *Journal of applied physics* 6.68 (1990), pp. 2752–2759.

[9] M. Cardona. “Vibrational spectra of hydrogen in silicon and germanium”. In: *Physica Status Solidi. B, Basic Research* 2.118 (1983), pp. 463–481.

[10] W. E. Carlos and P.C. Taylor. “1 H NMR in a-Si”. In: *Physical Review B* 7.26 (1982), pp. 3605–3616.

[11] S. Chandra and V. Bhatt. “RF sputtering: A viable tool for MEMS fabrication”. In: 34 (2009), pp. 543–556.

[12] R.W. Collins, I. An I, and H.V. Nguyen. “Real time spectroscopic ellipsometry for characterization of nucleation, growth, and optical functions of thin films”. In: *Thin Solid Films* 1-2.233 (1993), pp. 244–252.

[13] A. Cuevas et al. “Skin care for healthy silicon solar cells”. In: *IEEE 42nd Photovoltaic Specialist Conference (PVSC)* (2015), pp. 1–6.

[14] S. Dam. *What is the Role of the Depletion Region in a Semiconductor PN Junction?* 2023. URL: `https://www.azom.com/article.aspx?ArticleID=22739` (visited on 08/22/2023).

[15] W.D. Eades and R.M. Swanson. “Determination of the capture cross section and degeneracy factor of $Si-SiO_2$ interface states”. In: *Applied physics letters* 44.10 (1984), pp. 988–990.

[16] Enerdata. *World Energy & Climate Statistics – Yearbook 2023*. 2023. URL: `https://yearbook.enerdata.net/total-energy/world-consumption-statistics.html`.

[17] FEI. *NOVA SEM User Operation Manual*. 4th ed. U.S., 2013.

[18] F. Feldmann. “Carrier-selective contacts for high-efficiency Si solar cells”. In: *The Title of the Journal* (2015).

[19] F. Feldmann, G. Nogay, and J.I. Polzin. “A study on the charge carrier transport of passivating contacts”. In: *IEEE Journal of Photovoltaics* 6.8 (2018), pp. 1503–1509.

[20] L. Filipovic. “Topography simulation of novel processing techniques”. In: (2012).

[21] H. Fujiwara and M. Kondo. “Interface structure in a-Si: H/c-Si heterojunction solar cells characterized by optical diagnosis technique”. In: *IEEE 4th World Conference on Photovoltaic Energy Conference* 2 (2006), pp. 1443–1448.

[22] H. Fujiwara, M. Kondo, and A. Matsuda. “Nucleation mechanism of microcrystalline silicon from the amorphous phase”. In: *Journal of non-crystalline solids* 338 (2004), pp. 97–101.

[23] G.Lavareda and C.N. de Carvalho. “Properties of high growth rate amorphous silicon deposited by MC-RF-PECVD”. In: *Vacuum* 3-4.64 (2002), pp. 245–248.

[24] S. Glunz, D. Biro, and S. Rein. “Field-effect passivation of the $SiO_2 - Si$ interface”. In: *Journal of Applied Physics* 86.1 (1999), pp. 683–691.

[25] S.W. Glunz and F. Feldmann. “SiO_2 surface passivation layers–a key technology for silicon solar cells”. In: *Solar Energy Materials and Solar Cells* 185 (2018), pp. 260–269.

[26] G. Gram. “Passivation characterisation of poly-Si based passivating contacts”. In: (2021).

[27] J.L. Guizot, K. Nomoto, and A. Matsuda. “Surface reactions during the a-Si: H growth in the diode and triode glow-discharge reactors”. In: *Surface science* 1-2.244 (1991), pp. 22–38.

[28] X. Guo, M. Liao, and Z. Rui. “Comparison of different types of interfacial oxides on hole-selective p+-poly-Si passivated contacts for high-efficiency c-Si solar cells”. In: *Solar Energy Materials and Solar Cells* 210 (2020), p. 110487.

[29] S.M. Hu. “Formation of stacking faults and enhanced diffusion in the oxidation of silicon”. In: *Journal of Applied Physics* 4.45 (1974), pp. 1567–1573.

[30] IEA. “World total final consumption by source, 1971-2019”. In: (2022).

[31] N. Ikarashi and K. Watanabe. “High-resolution transmission electron microscopy of an atomic structure at a Si (001) oxidation front”. In: *Physical Review B* 23.62 (2000), p. 15989.

[32] S. Kageyama and Akagawa. “Dielectric function of a-Si: H based on local network structures”. In: *Physical Review B* 19.83 (2011), p. 195205.

[33] B. El-Kareh and L.N. Hutter. “Fundamentals of semiconductor processing technology”. In: *Springer Science Business Media* (2012).

[34] W.M.M. Kessels, A.H.M. Smets, and D.C. Marra. “On the growth mechanism of a-Si: H”. In: *Thin Solid Films* 1-2.383 (2001), pp. 154–160.

[35] T.C. Kho, S.C. Baker-Finch, and K.R. McIntosh. “The study of thermal silicon dioxide electrets formed by corona discharge and rapid-thermal annealing”. In: *Journal of Applied Physics* 5.109 (2011).

[36] H. Kim, S. Bae, and K. Ji. “Passivation properties of tunnel oxide layer in passivated contact silicon solar cells”. In: *Applied Surface Science* 409 (2017), pp. 140–148.

[37] T. Kobayashi and T.O.T. Ogawa. “Hotta S H S. Plasma-enhanced chemical vapor deposition of silicon nitride”. In: *Japanese journal of applied physics* 31.2R (1992), p. 336.

[38] J. Koh, Y. Lee Y, and H. Fujiwara. “Optimization of hydrogenated amorphous silicon p–i–n solar cells with two-step i layers guided by real-time spectroscopic ellipsometry”. In: *Applied Physics Letters* 11.73 (1998), pp. 1526–1528.

[39] M.J. Kushner. “A model for the discharge kinetics and plasma chemistry during plasma enhanced chemical vapor deposition of amorphous silicon”. In: *63* 8 (1988), pp. 2532–2551.

[40] A.A. Langford and M.L. Fleet. “Infrared absorption strength and hydrogen content of hydrogenated amorphous silicon”. In: *Physical Review B* 23.45 (1992), p. 13367.

[41] W.C. Lee and C. Hu. “Modeling CMOS tunneling currents through ultrathin gate oxide due to conduction-and valence-band electron and hole tunneling”. In: *IEEE Transactions on Electron Devices* 7.48 (2001), pp. 1366–1373.

[42] H. Lin et al. “Silicon heterojunction solar cells with up to 26.81% efficiency achieved by electrically optimized nanocrystalline-silicon hole contact layers”. In: *nature energy* 1.11 (2023).

[43] W. Liu. “Correlation between microstructure and electrical properties of amorphous silicon in crystalline silicon/amorphous silicon heterojunction solar cells”. In: (2017).

[44] W. Liu, X. Yang, and J. Kang. “Polysilicon passivating contacts for silicon solar cells: interface passivation and carrier transport mechanism”. In: *ACS Applied Energy Materials* 2.7 (2019), pp. 4609–4617.

[45] G. Lucovsky. “Structural interpretation of the vibrational spectra of a-Si: H alloys”. In: *Physical Review B* 4.19 (1979), p. 2064.

[46] G. Lucovsky. “Vibrational spectroscopy of hydrogenated amorphous silicon alloys”. In: *Solar Cells* 4.2 (1980), pp. 431–442.

[47] lxcat. URL: `www.lxcat.net` (visited on 08/24/2023).

[48] A. Matsuda and T. Goto. “Role of surface and growth-zone reactions in the formation process of μc-Si: H”. In: *MRS Online Proceedings Library* 3.164 (1989).

[49] A. Matsuda, M. Takai, and T. Nishimoto. “Control of plasma chemistry for preparing highly stabilized amorphous silicon at high growth rate”. In: *Solar Energy Materials and Solar Cells* 1-4.78 (2003), pp. 3–26.

[50] J. Melskens. “Optimisation of a protocrystalline hydrogenated amorphous silicon top solar cell for highest stabilised efficiency”. In: (2007).

[51] MicroChemicals. *WET-CHEMICAL ETCHING OF SILICON AND SIO_2*. 2000. URL: `https://www.microchemicals.com/technical_information/silicon_etching.pdf` (visited on 08/25/2023).

[52] A. Moldovan, F. Feldmann, and K. Kaufmann. “Tunnel oxide passivated carrier-selective contacts based on ultra-thin SiO_2 layers grown by photo-oxidation or wet-chemical oxidation in ozonized water”. In: *IEEE 42nd Photovoltaic Specialist Conference (PVSC)* (2015), pp. 1–6.

[53] j. Müllerová and P. Šutta. “Microstructure of hydrogenated silicon thin films prepared from silane diluted with hydrogen”. In: *Applied Surface Science* 12.254 (2008), pp. 3690–3695.

[54] Nagwa. *Lesson Explainer: Doped Semiconductors*. 2023. URL: `https://www.nagwa.com/en/explainers/732145693936/` (visited on 08/22/2023).

[55] K.O. Ng and D. Vanderbilt. “Structure and oxidation kinetics of the Si (100)-SiO_2 interface”. In: *Physical Review B* 15.59 (1999), p. 10132.

[56] R. E. Norberg and D.J. Leopold. “Non-bonded hydrogen in a-Si: H”. In: *Journal of non-crystalline solids* 227 (1998), pp. 124–127.

[57] Olympus. *A Guide to LED Light Sources for Microscope Devices*. 2022. URL: `https://www.olympus-lifescience.com/en/discovery/a-guide-to-led-light-sources-for-microscope-devices/` (visited on 08/24/2023).

[58] Y.Y. Ong, B.T. Chen, and F.E.H. Tay. “Process analysis and optimization on PECVD amorphous silicon on glass substrate”. In: *Journal of Physics: Conference Series. IOP Publishing* 1.34 (2006), p. 812.

[59] R. Osibanjo. *Infrared Spectroscopy*. URL: `https://https://chem.libretexts.org/Bookshelves/Physical_and_Theoretical_Chemistry_Textbook_Maps/Supplemental_Modules_%28Physical_and_Theoretical_Chemistry%29/Spectroscopy/Vibrational_Spectroscopy/Infrared_Spectroscopy/Infrared_Spectroscopy` (visited on 08/24/2023).

[60] D.K. Pandey, H.L. Kagdada, and P. Sanchora. “Overview of raman spectroscopy: Fundamental to applications”. In: *Modern Techniques of Spectroscopy: Basics, Instrumentation, and Applications* (2021), pp. 145–184.

[61] S.I. Park, Y.J. Quan, and S.H. Kim. “A review on fabrication processes for electrochromic devices”. In: *International Journal of Precision Engineering and Manufacturing-Green Technology* 3 (2016), pp. 397–421.

[62] Y. Peng. *Title of the Website*. 2005. URL: `https://ir.nctu.edu.tw/bitstream/11536/64501/2/952802.pdf` (visited on 08/24/2023).

[63] J. Perrin, M. Shiratani, and P. Kae-Nune. “Surface reaction probabilities and kinetics of H, SiH_3, Si_2H_5, CH_3, and C_2H_5 during deposition of a-Si: H and a-C: H from H_2, SiH_4, and CH_4 discharges”. In: *Journal of Vacuum Science Technology A: Vacuum, Surfaces, and Films* 1.16 (1998), pp. 278–289.

[64] S. Philipps. “Photovoltaics Report”. In: (2023).

[65] W.B. Pollard and G Lucovsky. “Phonons in polysilane alloys”. In: *Physical Review B* 6.26 (1982), p. 3172.

[66] H. Proksche, G. Nagorsen, and D. Ross. “The Influence of NH 4 F on the Etch Rates of Undoped SiO2 in Buffered Oxide Etch”. In: *Journal of the Electrochemical Society* 2.139 (1992), p. 521.

[67] PVEducation. *Series Resistance*. 2023. URL: `https://www.pveducation.org/pvcdrom/design-of-silicon-cells/series-resistance` (visited on 08/22/2023).

[68] F.M. Ross and J.M. Gibson. “Dynamic observations of interface motion during the oxidation of silicon”. In: *Surface Science* 1-3.310 (1994), pp. 243–266.

[69] H. Sai and P.W. Chen. “Impact of intrinsic amorphous silicon bilayers in silicon heterojunction solar cells”. In: *Journal of Applied Physics* 10.124 (2018).

[70] A. Sakai, T. Tatsumi, and K. Ishida. “Growth kinetics of Si hemispherical grains on clean amorphous□Si surfaces”. In: *Journal of Vacuum Science Technology A: Vacuum, Surfaces, and Films* 6.11 (1993), pp. 2950–2953.

[71] A. Saraei, M.J. Eshraghi, and F. Tajabadi. “ECV Doping Profile Measurements in Silicon Using Conventional Potentiostat”. In: *Journal of Electronic Materials* 47 (2018), pp. 7309–7315.

[72] P.M. Sarro and S. Brida. “Anisotropic etching of silicon in saturated TMAHW solutions for IC-compatible micromachining”. In: *Sensors and materials* 10 (1998), pp. 201–212.

[73] J. Schmidt, R. Peibst, and R. Brendel. “Surface passivation of crystalline silicon solar cells: Present and future”. In: *Solar Energy Materials and Solar Cells* 187 (2018), pp. 39–54.

[74] M. Schofthaler, R. Brendel, and G. Langguth. “High-quality surface passivation by corona-charged oxides for semiconductor surface characterization”. In: *Proceedings of 1994 IEEE 1st World Conference on Photovoltaic Energy Conversion-WCPEC (A Joint Conference of PVSC, PVSEC and PSEC). IEEE* 2 (1994), pp. 1509–1512.

[75] N. Sharma, M. Hooda, and S.K. Sharma. “Synthesis and characterization of LPCVD polysilicon and silicon nitride thin films for MEMS applications”. In: *Journal of Materials,* (2014), pp. 1–8.

[76] P.G. Sheasby, S. Wernick, and R. Pinner. “Surface treatment and finishing of aluminum and its alloys”. In: 1 (1987).

[77] T. Shimura and E. Mishima. “Ordered structure in the thermal oxide layer on silicon substrates”. In: *5th International Symposium on the Physics and Chemistry of SiO_2 and the Si-SiO_2 Interface-2005 Fall Meeting of the Electrochemical Society* (2006), pp. 39–48.

[78] G. Shivkumar, S.S. Tholeti, and M.A. Alrefae. “Analysis of hydrogen plasma in a microwave plasma chemical vapor deposition reactor”. In: *Journal of Applied Physics* 11.119 (2016).

[79] V. Šimonka. “Thermal oxidation and dopant activation of silicon carbide”. In: (2018).

[80] A. Smets et al. *Solar energy: The physics and engineering of photovoltaic conversion, technologies and systems*. Delft, the Netherlands: UIT Cambridge Ltd, 2016.

[81] A.H.M. Smets, W.M.M. Kessels, and M.C.M. (Van de Sanden). “Temperature dependence of the surface roughness evolution during hydrogenated amorphous silicon film growth”. In: *Applied physics letters* 6.82 (2003), pp. 865–867.

[82] M. Sowinska. “In-operando hard X-ray photoelectron spectroscopy study on the resistive switching physics of HfO2-based RRAM”. In: *BTU Cottbus-Senftenberg* (2014).

[83] H. Steinkemper, F. Feldmann, and M. Bivour. “Numerical simulation of carrier-selective electron contacts featuring tunnel oxides”. In: *IEEE Journal of Photovoltaics* 5.5 (2015), pp. 1348–1356.

[84] P. Stradins, S. Essig, and Nemeth. “Passivated tunneling contacts to n-type wafer silicon and their implementation into high performance solar cells”. In: *National Renewable Energy Lab.(NREL)* (2014).

[85] K. Tatsumura and T. Watanabe. “Residual order within thermally grown amorphous SiO_2 on crystalline silicon”. In: *Physical Review B* 8.69 (2004), p. 085212.

[86] D. Tetzlaff et al. “A simple method for pinhole detection in carrier selective POLO-junctions for high efficiency silicon solar cells”. In: *Solar Energy Materials and Solar Cells* 173 (2017), pp. 106–110.

[87] *The physics and chemistry of SiO_2 and the Si-SiO_2 interface*. Springer Science Business Media, 2013.

[88] J. Tsaur and C.H. Du. “Investigation of TMAH for front-side bulk micromachining process from manufacturing aspect”. In: *Sensors and Actuators A: Physical* 1-3.92 (2001), pp. 375–383.

[89] Molecula Vista. *Nano-FTIR vs. PiF-IR: Comparing Nano-IR Techniques Get the pdf*. URL: `https://molecularvista.com/technology/comparisons/nano-ftir-vs-pif-ir/` (visited on 08/24/2023).

[90] M. Walock. “Nanocomposite coatings based on quaternary metalnitrogen”. In: *ENSAM* (2012).

[91] H. Watanabe and K. Kato. “Kinetics of initial layer-by-layer oxidation of Si (001) surfaces”. In: *Physical Review Letters* 2.80 (1998), p. 345.

[92] H. Wei, Y. Zeng, and J. Zheng. “Unraveling the passivation mechanisms of c-Si/SiO_x/poly-Si contacts”. In: *Solar Energy Materials and Solar Cells* 250.112047 (2023).

[93] B. van Wijngaarden and J. Yang. “Inaccuracies in contact resistivity from the Cox–Strack method: A review”. In: *Solar Energy Materials and Solar Cells* 246 (2022), p. 111909.

[94] J.A. Woolam. *Title of the Website*. URL: `https://www.jawoollam.com/resources/ellipsometry-faq#toggle-id-2` (visited on 08/24/2023).

[95] E. Yablonovitch, R.M. Swanson, and W.D. Eades. “Electron□hole recombination at the $Si - SiO_2$ interface”. In: *Applied Physics Letters* 48.3 (1986), pp. 245–247.

[96] G. Yang, R. Gram, and P. Procel. “Will SiO_x-pinholes for SiO_x/poly-Si passivating contact enhance the passivation quality?” In: *Solar Energy Materials and Solar Cells* 252.112200 (2023).

[97] Z. Yang, Z. Liu, and W. Cui. “Charge-carrier dynamics for silicon oxide tunneling junctions mediated by local pinholes”. In: *Cell Reports Physical Science* 12.2 (2021).

[98] ysu. *Principle of FTIR*. URL: `https://clsfzx.ysu.edu.cn/__local/3/5F/E9/D185512F536F3C5240CF3E2BCB0_EB876EB6_769CA.pdfy` (visited on 08/24/2023).

[99] ysu. *Principle of Raman*. URL: `https://http://rportal.lib.ntnu.edu.tw:8080/server/api/core/bitstreams/f21b2a4e-2f0d-45c9-ab03-8ad0dd49e02c/content` (visited on 08/24/2023).

[100] C. Yu. “Recent advances in and new perspectives on crystalline silicon solar cells with carrier-selective passivation contacts”. In: *Crystals* 8.11 (2018), p. 430.